Modelling and analysis of particle aggregation and breakage for marine water treatment

Bilde, Kasper Gram

DOI (link to publication from Publisher):
10.54337/aau539407477

Publication date:
2023

Document Version
Publisher's PDF, also known as Version of record

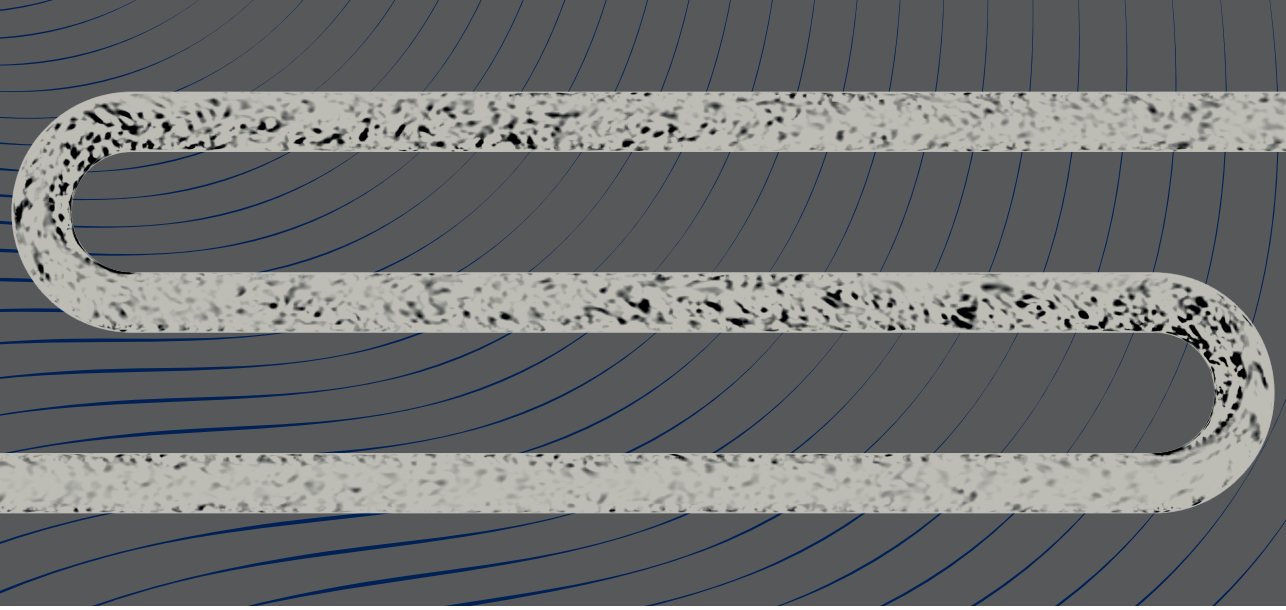

MODELLING AND ANALYSIS OF PARTICLE AGGREGATION AND BREAKAGE FOR MARINE WATER TREATMENT

BY
KASPER GRAM BILDE

DISSERTATION SUBMITTED 2023

AALBORG UNIVERSITY
DENMARK

Modelling and analysis of particle aggregation and breakage for marine water treatment

Ph.D. Dissertation

Kasper Gram Bilde

Dissertation submitted February 2023

Dissertation submitted:	February 23, 2023
PhD supervisors:	Associate Professor Kim Sørensen Aalborg University
	Søren Mølgaard Alfa Laval Aalborg A/S
Assistant PhD Supervisor:	Associate Professor Jakob Hærvig Aalborg University
	Anders Schou Simonsen Alfa Laval Aalborg A/S
PhD committee:	Associate Professor Vincenzo Liso (Chairman) Aalborg University, Denmark
	Associate Professor Antonio Buffo Politecnico di Torino, Italy
	Dr. Dirk Lucas Helmholtz-Zentrum Dresden – Rossendorf, Germany
PhD Series:	Faculty of Engineering and Science, Aalborg University
Department:	AAU Energy

ISSN (online): 2446-1636
ISBN (online): 978-87-7573-741-3

Published by:
Aalborg University Press
Kroghstræde 3
DK – 9220 Aalborg Ø
Phone: +45 99407140
aauf@forlag.aau.dk
forlag.aau.dk

Printed in Denmark by Stibo Complete, 2023

Abstract

To comply with the sulphur regulations introduced by the International Maritime Organisation in January 2020, ship owners can install exhaust gas cleaning equipment onboard vessels such as a wet scrubber. The wet scrubber removes sulphur from the exhaust gas by washing it with seawater or fresh water. Several countries and regions worldwide have prohibited the use of scrubbers operating in open-loop mode, which limits the use of scrubbers to closed-loop operations. During closed-loop operation the freshwater is recirculated over the scrubber and the concentration of pollutants continuously increases. To comply with the discharge legislation, a high-speed centrifugal separator is used to sediment the pollutants in an efficient way. To increase the efficiency of the high-speed separator, a pre-treatment system, consisting of a pipe flocculator is installed to aggregate the micron-sized particles.

The aggregation and breakage of micron-sized particles are studied using a multiphase computational fluid dynamics (CFD) model where the continuous and dispersed phases are described using the two-fluid Eulerian approach. The number density function of the dispersed phase is tracked using the population balance equation (PBE) which is solved using the class method. Interfacial momentum transfer between the two phases is included in the study to achieve a two-way coupled model. High-fidelity, large-eddy simulations are carried out to analyse the decay of secondary motion and the downstream turbulence characteristics of the flow through a 180° bend. The particle strength parameter is validated against an experimentally measured particle size distribution measured in the Alfa Laval Test and Training Centre.

Results show that the most critical geometrical parameter that influences the particle size distribution is the pipe bend radius. Furthermore, it is shown that when the Reynolds number is significantly large ($\mathrm{Re_d} > 30,000$), the influence of the bend radius becomes negligible as the naturally occurring turbulence breaks the largest aggregates.

This PhD project has contributed to achieving a better understanding of inline flocculation systems with a dilute disperse phase. The proposed modelling approach allows an in-depth study of the aggregation and breakage of micron-sized particles.

Resumé

Skibsredere kan installere udstyr til at rense udstødningsgassen fra motorer for dermed at overholde lovningen vedr. udledning af svovl som den Internationale Maritime Organisation indførte per januar, 2020. Et sådanne udstyr kan være en scrubber som fjerner svovl i udstødningsgassen ved at vaske udstødningsgassen med enten havvand eller ferskvand. Flere lande og område har forbudt brugen af scrubbere der fungerer i open-loop tilstand, hvilket begrænser brugen af scrubbere i disse områder til closed-loop tilstand. Derfor skal scrubberen fungere i closed-loop tilstand hvor ferskvand recirkuleres over scrubberen, hvilket betyder at der sker en kontinuerlig stigning af forurenende stoffer i vandet. For at overholde lovgivning af udledningsvandets vandkvalitet bruges en centrifugal højhastighedsseparator. Et forbehandlingssystem, bestående af en rør-flokkulator, er installeret opstrøms med det formål at aggregere partikler af mikronstørrelse for at opnå en højere effektivitet.

Opbrydning og aggregering af partikler af mikronstørrelse er studeret ved brug af computational fluid dynamics (CFD) hvor fluid- og partikel faserne er beskrevet af en two-fluid Eulerian metode. Taltæthedsfunktionen af partiklerne er sporet af population balance equation som løses ved brug af class method. Momentumtransport mellem fluid- og partikelfaserne er betragtet og derved opnås en tovejskoblet model. Turbulens karakteristika for et 180° rørbuk i en rørflokkulator er simuleret med høj troværdighed ved brug af en large-eddy simuleringer. Parameteren for partikelstyrke er valideret mod tests udført i Alfa Lavals Test og Trænings Center i Aalborg hvor partikelstørrelsen blev målt.

Den geometriske parameter der påvirker størrelsesfordelingen mest i en rørflokkulator er bukkeradius. Endvidere, er det vist at når Reynolds tallet blive tilstrækkeligt højt ($\mathrm{Re_d} > 30,000$) er effekten af at have et rørbuk i systemet negligerbar, da den naturligt forekomne turbulens opbryder de største aggregater.

Denne Ph.D. afhandling bidrager med en dybere forståelse af fluid-partikel systemer og hvordan partikler af mikronstørrelse aggregerer og opbryder i et rørsystem. Ved brug af to-vejs CFD modellen kan systemet analyseres lokalt for at undersøge hvor aggregering og opbrydning forekommer.

Preface

This thesis is submitted to the Faculty of Engineering and Science at Aalborg University, Denmark, for the degree of Doctor of Philosophy, PhD. The industrial PhD dissertation covers research work taken place at Aalborg University and Alfa Laval Aalborg A/S and the project was carried out from January 2020 to January 2023. The PhD project was supervised by Associate Professor Kim Sørensen and Associate Professor Jakob Hærvig from Aalborg University as well as Søren Mølgaard and Anders Schou Simonsen from Alfa Laval Aalborg A/S. The project was funded by Innovation Fund Denmark under grant no. 9065-00188B and Alfa Laval Aalborg A/S.

I would like to express my sincere gratitude to my supervisors for their discussions, scientific input and general support throughout my studies. Furthermore, I would like to thank my colleagues from Aalborg University, where Nick Høy Hansen, Ali Yahyaee Nujukambari, Tianbao Gu and Tom Condra have listened to my concerns and ideas and have provided valuable feedback. Also, I would like to thank the members of the multiphase flows and heat transfer research group for providing valuable knowledge throughout this project. From Alfa Laval, I would like to express my sincere gratitude to my supervisors as well as Olle Törnblom and Staffan Königsson for their assistance during this PhD project.

Also, I would like to thank Dr Ronald Lehnigk and Dr Fabian Schlegel at Helmholtz-Zentrum Dresden-Rossendorf for their assistance and guidance throughout the development and implementation of mathematical models in the OpenFOAM framework.

Finally, I would like to thank my family, and especially my girlfriend, Ida, for their loving support and motivation allowing me to pursue what I find most interesting.

"Hur ska jag kunna veta det, när jag aldrig har försökt?" - Pippi Långstrump
when asked if she plays the trumpet.

Kasper Gram Bilde
Aalborg University, February 23, 2023

Thesis Details

Thesis Title:	Modelling and analysis of solid particle aggregation and breakage for marine water treatment
PhD Student:	Kasper Gram Bilde
Supervisors:	Assoc. Prof. Kim Sørensen, Aalborg University
	Assoc. Prof. Jakob Hærvig, Aalborg University
	Søren Mølgaard, Alfa Laval Aalborg A/S
	Anders Schou Simonsen, Alfa Laval Aalborg A/S

The contents of this thesis are based on the journal and conference papers that have been published during this PhD project. The papers in their full length can be found in Part II.

Journal Papers

[A] Kasper Gram Bilde, Ronald Lehnigk, Jakob Hærvig, Fabian Schlegel and Kim Sørensen, "On the agglomeration and breakage of particles in turbulent flows through pipe bends using CFD-PBE", *Chemical Engineering Science*, Vol. 260, 117915, 2022, `https://doi.org/10.1016/j.ces.2022.117915`.

[B] Kasper Gram Bilde, Kim Sørensen and Jakob Hærvig, "Decay of secondary motion downstream bends in turbulent pipe flows", *Physics of Fluids*, Vol. 35, 2023

[C] Kasper Gram Bilde, Kim Sørensen and Jakob Hærvig, "On the design of compact hydraulic pipe flocculators using CFD-PBM", *Chemical Engineering Research and Design*. **Under review**

Conference Papers

[D] Kasper Gram Bilde, Jakob Hærvig and Kim Sørensen, "Aggregation and breakage of solid particles in a turbulent flow through a 90° pipe bend using CFD-PBE", *The 17th OpenFOAM Workshop*, Cambridge, United Kingdom, July 11-14, 2022, `https://vbn.aau.dk/files/479455489/OpenFOAM_Conference_2022.pdf`.

In addition to the included papers, the following software publications were also completed during the PhD period.

Software

[1] Fabian Schlegel, Kasper Gram Bilde Mazen Draw Ilya Evdokimov Susann Hänsch, Vikrant Vinayak Kamble Haris Khan Benjamin Krull, Ronald Lehnigk Jiadong Li, Hongmei Lyu, Richard Meller, Gašper Petelin, Sesi Preetam Kota and Matej Tekavčič, "HZDR Multiphase Addon for OpenFOAM", 2022, `https://doi.org/10.14278/rodare.1877`.

Thesis Structure

The topic of this dissertation is the numerical analysis of aggregation and breakage of micron-sized soot particles in a pre-treatment flocculation system using CFD to achieve accelerated sedimentation onboard marine vessels. This is motivated by a number of vessels having difficulties cleaning the washwater from a wet scrubber using a high-speed separator. To achieve a better separation efficiency in a high-speed separator, micron-sized particles are aggregated to achieve a larger effective particle diameter which results in a faster sedimentation velocity. The numerical analysis is carried out using Computational Fluid Dynamics (CFD) to model the fluid phase and this method is coupled with the Population Balance Equation (PBE) to model the dispersed particle phase. Several simulations are carried out to determine a suitable modelling framework that describes the fluid-particle flow, which in the end leads to an optimised design of the aggregation application. The numerical model is validated against data from literature and experimental measurements performed in the Alfa Laval Test and Training Centre.

The thesis is organised in a paper-based structure where Part I includes a summary report that provides an overview of the work. The published papers are presented in their full length in Part II.

Nomenclature

Symbols

	Representation	Unit		Representation	Unit
a	Aggregation frequency	$1/s$	b	Breakage frequency	$1/s$
B	Particle strength parameter	m^3/s^3	C	Coefficient	-
d	Diameter	m	D_f	Fractal dimension	-
F	Force	N	g	Gravitational acceleration	m/s^2
G	Velocity gradient	$1/s$	H	Total contact number	-
K	Internal coordinate rate of change	-	k_c	Constant relative to packing	-
L	Length	m	m	Moment	Mixed
M	Interfacial momentum transfer	N/m^3	n	Number	-
N	Number	-	P	Power	W
p	Pressure	Pa	R	Effective radius	m
r	Radius	m	S	Source term	Mixed
t	Time	s	u	Velocity	m/s
V	Volume	m^3	W	Dissipated power per volume per unit time	$W/(m^3\ s)$
x, y, z	Spatial coordinates	m	x_i	Pivotal volume	m^3
y	Molar fraction	-			

Subscripts

	Representation		Representation
32	Sauter mean	b	Bend
c	Collision radius	cr	Critical
D	Drag	d	Diameter
disp	Dispersion	f	Fluid
h	Hydraulic diameter	L	Lift
p	Particle	r	Relative
s	Sedimentation	t	Turbulent
T	Total	v	Volume
VM	Virtual mass	φ	Phase
d′	Daughter particle		

Greek symbols

	Representation	Unit		Representation	Unit
α	Volume fraction	-	β	Daughter size distribution	-
γ	Number of daughters	-	ε	Turbulent dissipation rate	m^2/s^3
ζ	Zeta potential	V	μ	Dynamic viscosity	kg/(m s)
ν	Kinematic viscosity	m^2/s	ξ	Internal coordinate	Mixed
ρ	Density	kg/m^3	τ	Shear stress	Pa
φ	Pitch of inclination	m	ω	Specific turbulent dissipation rate	1/s
ω	Vorticity	1/s			

Abbreviations

	Representation		Representation
CFD	Computational fluid dynamics	CL	Closed loop
CM	Class method	DNS	Direct numerical simulation
DO	Diesel oil	DPF	Diesel particle filter
DQMOM	Direct quadrature method of moments	ECA	Emission control area
EQMOM	Extended quadrature method of moments	FNU	Formazin Nephelometric Units
HFO	Heavy fuel oil	HSS	High-speed separator
IMO	International Maritime Organization	LES	Large eddy simulation
MEPC	Marine Environment Protection Committee	MGO	Marine gas oil
MOM	Method of moments	NG	Natural gas
OL	Open loop	PAH	Polycyclic aromatic hydrocarbon
PBE	Population balance equation	PM	Particulate matter
QBMM	Quadrature-based method of moments	RANS	Reynolds-averaged Navier Stokes
RH	Relative humidity	RNG	Re-normalisation group
RSM	Reynolds stress model	SCR	Selective catalytic reduction
SGS	Subgrid-scale	TEM	Transmission electron microscopy
WALE	Wall adaptive local eddy	ZD	Zero discharge
VLSFO	Very low sulfur fuel oil	WESP	Wet electrostatic precipitator

Contents

Part I

Summary

1 | Introduction

The *International Maritime Organization* (IMO) adopted the *International Convention for Prevention of Pollution from Ships*, MARPOL, in 1973 to reduce harmful emissions from marine vessels. MARPOL consists of six annexes, where the latest *Annex VI*, was adopted in 2005 (IMO, 2020). Annex VI concerns harmful gas emissions from ships such as sulfuric oxides (SO_x), nitrogen oxides (NO_x), and particulate matter (PM). Emission Control Areas (ECA), seen in Fig. 1.1, were introduced by the IMO in the European Union and along the American coastline to have zones where stricter legislation can be invoked to reduce emissions even further. Since the

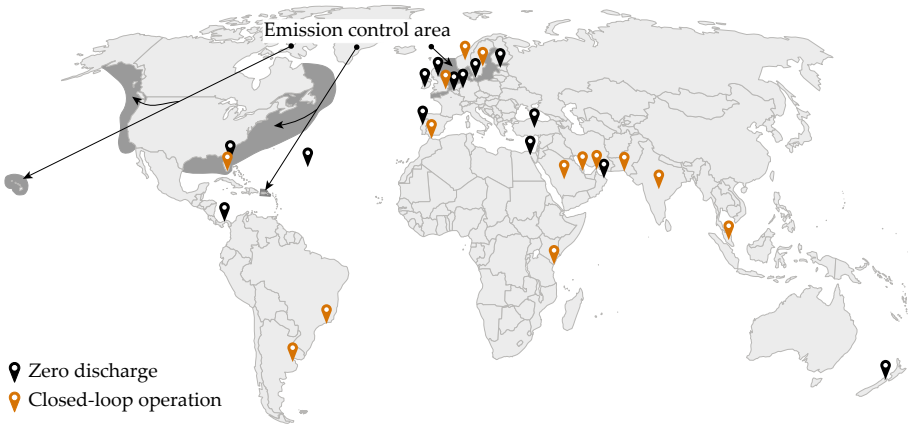

Fig. 1.1: Map of the world with ECA zones (International Maritime Organisation, 2019) and markers indicating local/national regulation on scrubber discharge effective as of the time of writing (EGCSA, 2022).

adoption of Marpol annex VI in 2005, the sulfur emissions inside ECAs have been reduced from $S_{eq} < 1.5\,\%$ to $S_{eq} < 0.1\,\%$ and

outside the ECAs, the sulfur emissions have been reduced from $S_{eq} < 4.5\,\%$ to $S_{eq} < 0.5\,\%$ as seen in Fig. 1.2. The sulfur equivalent is defined by measuring the molar fractions of SO_2 and CO_2 at the outlet of the funnel and calculated as $S_{eq} = 100\, y_{SO_2}/(43.3\, y_{CO_2})$, where y denotes the molar concentration of the species. To comply with these new regulations, ship owners must switch to a compliant fuel with a sulfur content of $< 0.005\ \mathrm{kg/kg_{fuel}}$ or install exhaust gas cleaning equipment such as a wet scrubber.

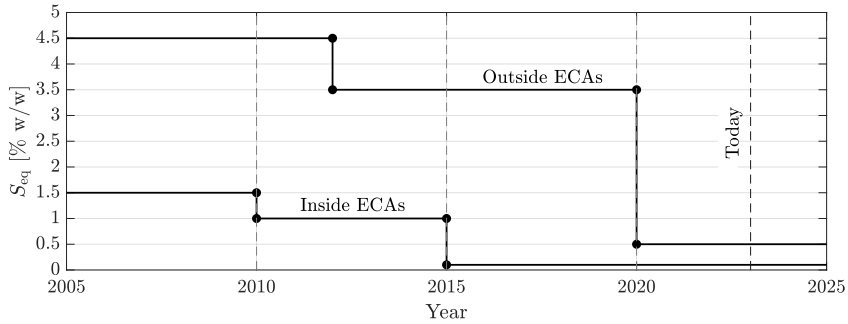

Fig. 1.2: Sulfur emission regulation limits within and outside ECAs over recent years.

1.1 Motivation

Since the IMO announced the adoption of MARPOL Annex VI, the ships with scrubbers installed have gone from just a few to over 5000, as seen in Fig. 1.3 (Clarkson, 2022). The majority of the scrubbers were ordered in 2019 and 2020, which was due to the implementation of new worldwide regulations and since then a smaller number of scrubbers have been ordered. Alfa Laval develops, sells and commissions wet scrubbers and has different types in their portfolio for various types of ships, see Fig. 1.4. A wet scrubber is used to transfer SO_x from the exhaust gas to the water which is used for scrubbing the exhaust gas. During the operation of a scrubber, the exhaust gas is first quenched in the jet section of the scrubber, seen in Fig. 1.4, with the objective of cooling the exhaust gas to achieve a lower velocity. The chemical adsorption takes place inside the packed bed absorption column

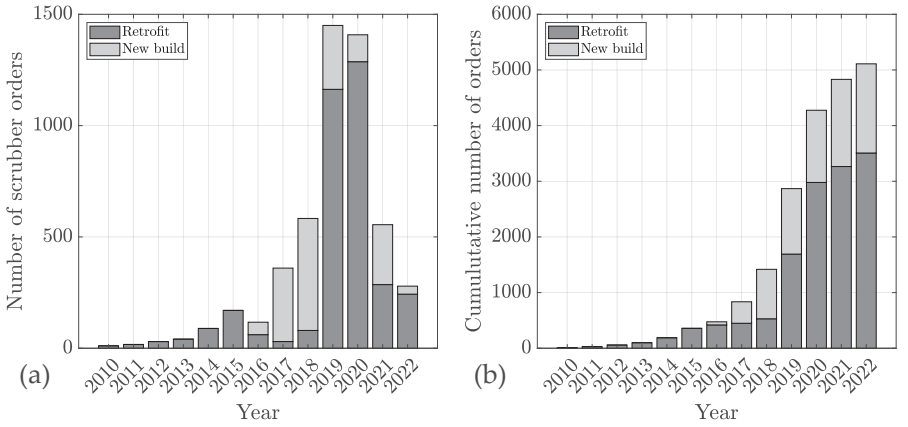

Fig. 1.3: Scrubbers contracted since 2010. Fig. 1.3a shows the number of scrubber contracts per year divided into retrofits and new build ships. Fig. 1.3b shows the cumulative sum of the number of contracted ships with scrubbers. Data from Clarkson (2022).

where water is sprayed on top of the packed bed. The majority of the SO_x is transferred from the gas phase to the water phase during this stage. To remove droplets in the gas, a demister is placed before the gas exists the scrubber. The objective of operating the scrubber is to remove the SO_x, but as a bi-product, the scrubber also captures particulate matter, oily residue and inorganic salts. Winnes et al. (2020) report that the scrubber removes 32 % to 43 % of the insoluble particulate mass in the exhaust gas and that the scrubber decreases the emissions of polycyclic aromatic hydrocarbons (PAH), black carbon, organic carbon and elemental carbon in the majority of the tests performed. This is in good agreement with the observations of Hansen (2012), who report PM removal efficiencies in the range of 45 % to 55 % for scrubbers equipped with sprayers. An increased PM removal efficiency of 79 % was observed when a so-called venturi pre-unit was installed, however, this is something that is rarely installed on marine vessels.

The scrubber can be operated in either open-loop (OL) or closed-loop (CL) mode as seen in the process diagram in Fig. 1.5. During open-loop operation, the sea chest pump pumps water to the scrubber for the scrubbing process and the effluent scrubber water is discharged back into the ocean. This is allowed by the IMO as long as the quality regulations for the discharged wa-

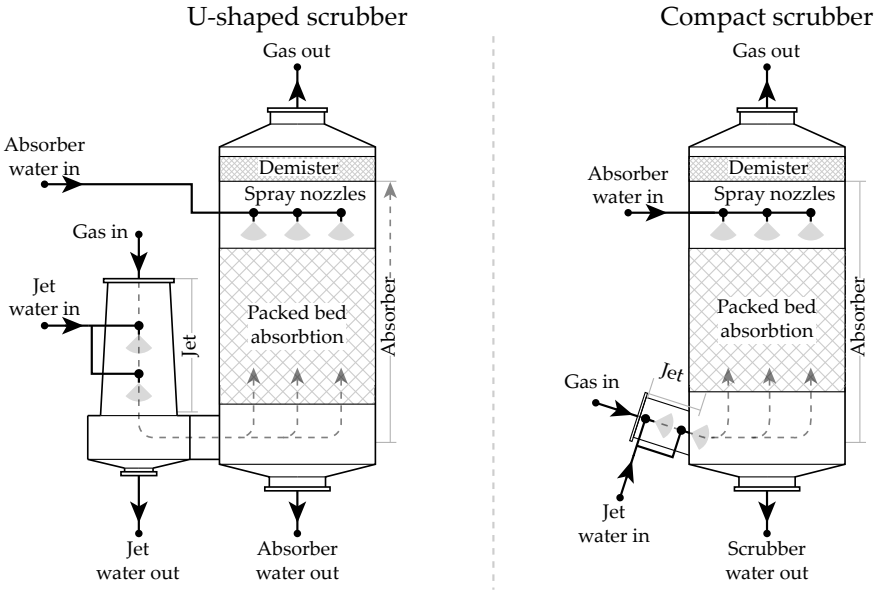

Fig. 1.4: Two configurations of the scrubber in Alfa Laval's portfolio. The U-shaped scrubber is the most widely installed, whereas the compact scrubber has a shorter and more efficient jet section for cooling the exhaust gas. Illustration reprinted and inspired from Simonsen (2018).

ter are met. The current quality requirements for the discharge water are defined in MEPC 340(77) and specify a minimum pH of 6.5 measured at a distance of 4 m from the overboard discharge point, a maximum continuous PAH concentration of 50 μg/L and a maximum turbidity of 25 Formazin Nephelometric Units (FNU) (MEPC, 2021). Several researchers have focused on the marine environmental impact of open-loop scrubbers, as the water is discharged back into the ocean without any cleaning. Kjølholt et al. (2012) were some of the early researchers to study the impact of discharging scrubber water in the North Sea and Baltic Sea. It was reported that the acidic water would have a negligible impact on the ocean, as the acidic buffer capacity exceeds the emissions. Furthermore, they concluded that the concentrations of PAH, hydrocarbons, heavy metals and metalloids would have a magnitude below the levels of concern. Lange et al. (2015) analysed the impact of discharging scrubber water in ports and coastal waters, with a focus on the German coastal line. It was con-

cluded that the discharge of water from open-loop operation adds additional stress factors for marine organisms and recommends that the discharge of water from open-loop scrubbers should be prohibited in these areas. Magnusson et al. (2018) analysed the scrubber effluent water of both closed-loop and open-loop scrubbers and their impact on marine organisms. They concluded that toxic components in the water impacted the marine organisms, however, it was difficult to accurately determine which components disrupted the organism. When the scrubber is operating in

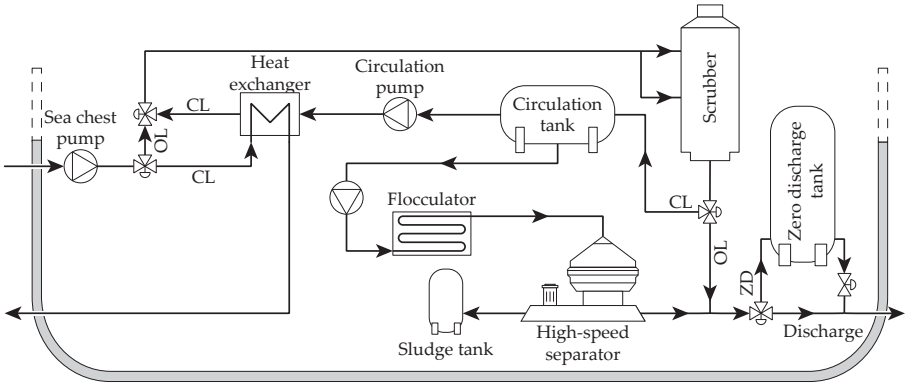

Fig. 1.5: Process diagram for the water flow of a hybrid wet scrubber with a water cleaning system. The wet scrubber can operate in open-loop (OL) where the water is pumped through the scrubber and back to the ocean or it can operate in closed-loop where the water is recirculated over the circulation tank. Before discharge, the water is cleaned using the high-speed separator where the sludge is stored in a sludge tank. A zero-discharge (ZD) tank is also shown, to visualise scenarios where the vessels cannot discharge scrubber water.

a closed-loop mode, the water is recirculated over a circulation tank, as seen in Fig. 1.5. The circulated water is cooled using seawater before being pumped into the scrubber for cleaning of the exhaust gas. The scrubber effluent water is then recirculated back to the circulation tank. As the water in the exhaust gas condenses inside the scrubber, some volume of water needs to be discharged from the system and as PM is continuously captured inside the scrubber, a cleaning system is therefore needed. The cleaning system, developed by Alfa Laval, consists of a pre-treatment system called a flocculator and a high-speed separator (HSS) which separates the PM from the water using highly accelerated sedi-

mentation. The separated particulate matter is stored as sludge in a dedicated tank and whenever the ship is in port, the sludge is pumped onshore and the port disposes of the sludge according to regulations.

Due to the large focus on the use of open-loop scrubbers, several countries and ports have adopted local legislation regarding the discharge of scrubber water. In Fig. 1.1 markers are placed in locations where local regulations have been adopted and the general tendency is that the scrubber must either be operated in closed-loop or a zero-discharge zone has been introduced. If a zero-discharge regulation is adopted, this means that the ship must either switch to compliant fuel or install a zero-discharge tank as shown in Fig. 1.5. The cleaned water stored in the zero-discharge tank can be discharged whenever the ship is outside the zero-discharge zone.

It is expected that a number of ports, countries and areas will have stricter legislation regarding the discharge of scrubber water to reduce the pollution of the oceans. Therefore, the continued use of scrubbers relies on having an efficient water cleaning system that effectively removes pollutants from the scrubber effluent water. This can, theoretically, be installed for open-loop scrubbers, but the concentrations of PM, PAH, heavy metal and other pollutants are very low, making it difficult to separate the pollutants from the water. During closed-loop operation, the concentration of pollutants continuously increases as the water is recirculated making this solution more favourable to clean.

The problem with designing an effective water cleaning system for marine applications is that space is sparse onboard a ship. The water cleaning system has to be designed in a compact way where it does not take up unnecessary space, which could otherwise be used for cargo. One of the core products of Alfa Laval's portfolio is the high-speed separator, which can be used for various jobs of separation, purification or both.

1.2 Working Principle of the High-Speed Separator

During operation the HSS rotates around its centre of mass with a fixed rotational speed, depending on its size and design, typically exerting the fluid and particles to a centrifugal force of 7,000-10,000g. Different types of separators are in Alfa Laval's portfolio including separators for liquid-liquid separation, e.g. separating oil from water, liquid-liquid-solid separation, e.g. separating oil and particles from water and liquid-solid separation which is the separator type used to clean the scrubber effluent water. An example of the bowl in a liquid-solid separator is seen in Fig. 1.6. In this separator, the scrubber effluent water enters from the top and goes into a distribution chamber where the water is led underneath a sealing ring as illustrated in Fig. 1.6. From here the solids, which are denser compared to water, move towards the circumference of the bowl and the water stays around the centreline of the separator. To achieve better separation, a set of conical disks are placed inside the HSS, to hinder particles from leaving the HSS with the water. The disk stack acts as a large surface wall, where the no-slip condition forces the denser particles to move downwards until they can reach the circumference of the bowl. At a given frequency the bowl opens and the solid phase is discharged as sludge. To understand the important parameters when separating solids using an accelerated sedimentation process, such as a centrifuge, consider first a sedimentation process working under regular gravitational acceleration. The simplest expression for the sedimentation velocity of solid particles under the influence of gravity is given by Stokes' law (Stokes, 1850) for spherical particles as

$$u_{\mathrm{s}} = \frac{d_{\mathrm{p}}^2 \left| \rho_{\mathrm{f}} - \rho_{\mathrm{p}} \right|}{18\mu} g \,, \tag{1.1}$$

where d_{p} is the diameter of the solid particle, ρ is the density, μ is the dynamic viscosity of the fluid, g is the gravitational acceleration and subscripts f and p denote the fluid and particle phase, respectively.

A faster sedimentation velocity results in a shorter retention

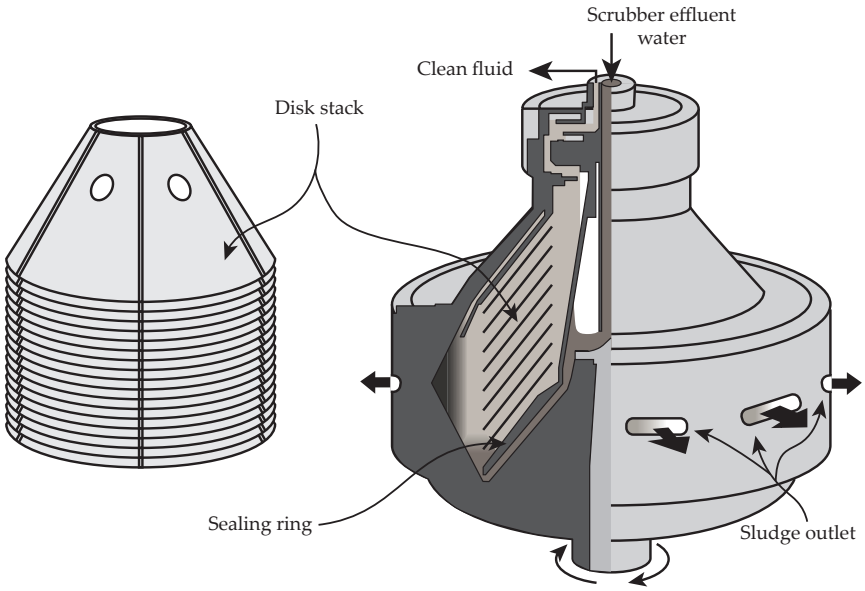

Fig. 1.6: Cross-sectional view of a liquid-solid high-speed separator, where the scrubber effluent water enters from the top, the clean fluid leaves at the top and the sludge is discharged to the side of the bowl. An example of the conical disk stack is also shown in the figure.

time inside the separation device, which means a faster and more efficient separation. Decreasing the viscosity is one option for achieving a faster sedimentation velocity, which can be achieved by increasing the temperature of the fluid. This is feasible until a certain temperature where either phase change or cavitation inside the high-speed separator might start to occur. The density difference between the phases is also fixed as the temperature does not affect the density of water significantly. This leaves two important factors, namely the gravitational acceleration, which can be increased when increasing the rotational speed and the effective diameter of the particle. The sedimentation velocity of a particle scales with the square of the diameter and the diameter of the particles is thereby the single most important parameter when increasing the efficiency of a high-speed separator.

1.3 Coagulation and Flocculation

To increase the effective diameter of the particles, it is required that the suspended particles are cohesive and can adhere to the surface of each other. This way, the effective diameter of a particle increases as more particles collide and aggregate. Depending on the chemical and mechanical properties of the particles in the process, they can either be naturally adhesive or additives can be added to change the adhesive properties of the solid particles. Soot particles suspended in water, which are the particles captured by the scrubber, become negatively charged with a zeta potential in the range of $30\,\text{mV} < \zeta < 50$ mV (Liu et al., 2003; Growney et al., 2015; Chen and Huang, 2017), which, according to Kumar and Dixit (2017), result in particles that have a moderate to good stability. Particles with a zeta potential in this range, will thereby naturally repel each other due to the electrical charge surrounding the given particles. The electrical charge is generally described by the electrical double layer (Gouy, 1910; Chapman, 1913; Stern, 1924) surrounding the particle and a conceptual visualisation of a particle with an electrical double layer is seen in Fig. 1.7. The electrical potential at the surface of the particle is known as the Nernst potential and the electrical potential from the slipping plane is known as the zeta potential.

The electrical potential of a particle can be changed by adding reversely charged ions to the solution and in Fig. 1.7 it is illustrated how the electrical double layer decreases as more reversely charged ions adhere to the surface. If too many reversely charged ions adhere to the surface of the particle, the electrical potential is reversed and the particles start to repel each other again. Changing the electrical potential of the particles is the first step in coagulation and often metal-based coagulants with positive ions are used in wastewater processes, e.g. aluminium chloride ($AlCl_3$), ferric sulphate ($Fe(SO_4)_3$) or sodium aluminate ($Na_2Al_2O_4$) among others.

When the electrical potential of the particles has been neutralised, the particles can adhere to the surface of each other. Coagulation can be an effective method to make fine particles ag-

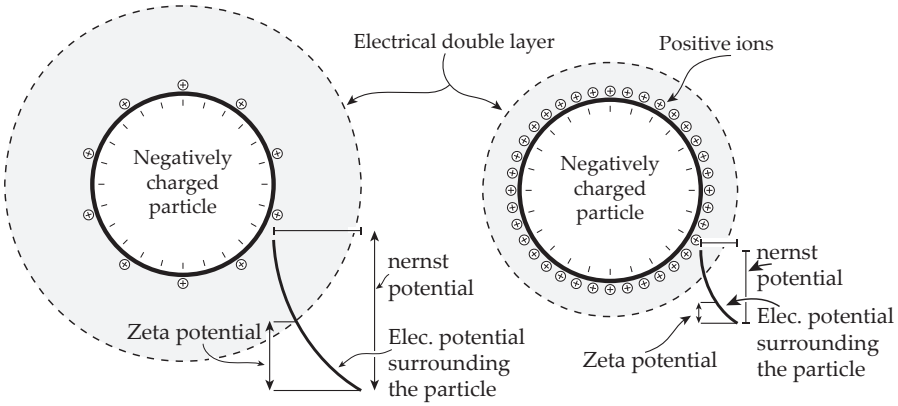

Fig. 1.7: Conceptual visualisation of the electrical double layer, where the figure on the left shows a negatively charged particle with a larger electrical double layer. On the right the same particle is treated with positively charged ions, e.g. Al^{2+}, resulting in a reduction in the electrical potential surrounding the particle. The visualisation is inspired by Priesing (1962).

gregate, but for many applications, the final aggregate size due to coagulation is too small to have a large impact. Therefore, polymer flocculants are often added to the process as well. Polymer flocculants hold a cationic or anionic charge and the magnitude of the charge depends on the particle charge of the application. These polymers also have different molecular architectures as they can be linearly bound or of a high interconnecting structure which again depends on the particle that needs to be aggregated. The overall working principle of the polymer flocculants is seen in Fig. 1.8, where the destabilised particles are subject to a fluid flow and then polymer flocculants are added to the solution. These long-chained polymers then capture and forms an enclosure around the particles, which effectively increases the effective diameter of the aggregate as seen by the fluid. The molecular architecture of the polymer often depends on the sedimentation application. For the present work, where a high-speed separator is utilised, the architecture of the polymers has to be of a high interconnecting structure, as the polymers will add strength to the aggregates when they enter the inlet of the high-speed separator.

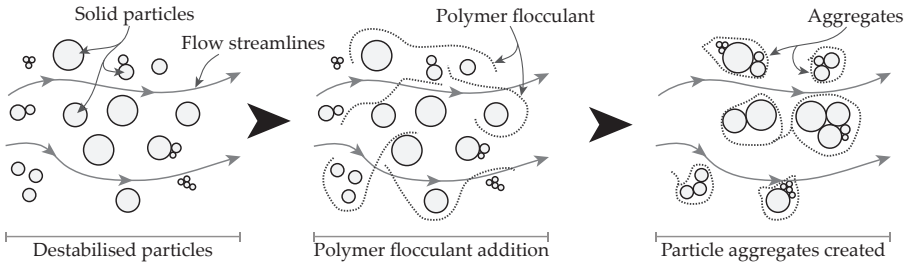

Fig. 1.8: Conceptual illustration of the flocculation process in a fluid flow. The polymer flocculant is added to the destabilised particles and due to the velocity fluctuations in the fluid, aggregates are created due to orthokinetic flocculation.

1.4 Orthokinetic Aggregation

The research into adhesive particles and how these aggregate in a fluid has been a relevant topic for more than a century. In general, the aggregation of particles is governed by the velocity gradients of the flow. As the velocity gradients of the flow increase in magnitude, particles will collide and aggregate at an increased frequency, however, due to the larger velocity gradients aggregates will form an ultimate smaller size due to the continuous breakdown of the largest aggregates (Bratby, 2016). A lower velocity gradient leads to larger aggregates but this takes more time as particle collisions occur at a lower frequency. A conceptual illustration of particle contact is seen in Fig. 1.9 where particles i and j come into contact due to a velocity gradient in a fluid flow.

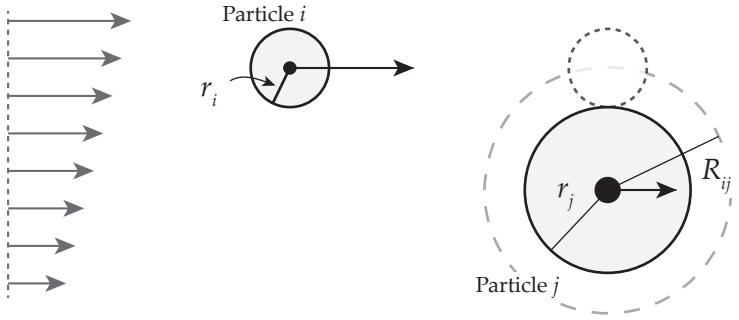

Fig. 1.9: Particle contact between particle i and j under the influence of a velocity gradient.

Particles must be close enough for the London-van der Walls

force to pull and hold the particles together. This is illustrated as the contact radius $R_{ij} = r_i + r_j$ in Fig. 1.9.

Historically, Smoluchowski (1917) proposed a mathematical model describing the theoretical orthokinetic aggregation of colloidal particles under laminar conditions. The total number of contacts between particles i and j per unit time under laminar flow conditions is given as

$$H_{ij} = \frac{4}{3} n_i n_j R_{ij}^3 \frac{dv}{dz}, \tag{1.2}$$

where dv/dz is the velocity gradient. The model of Smoluchowski (1917) is limited in value as it is mostly theoretical and the majority of industrial applications have flows in the turbulent regime. As the velocity gradient is unknown in turbulent flows, Camp and Stein (1943) replaced the velocity gradient in the existing model with a measurable root mean square (RMS) velocity gradient of the fluid as

$$G = \sqrt{\frac{W}{\mu}}, \tag{1.3}$$

where W is the mean value of dissipated power per unit volume per unit time. This definition can be a measurable value if dealing with mechanically stirred flocculation devices, where the power dissipated to the fluid is a measured value. This approach is, however, difficult when dealing with flows where turbulence is not induced by an electric motor. Saffman and Turner (1956) further correlated the velocity gradient in a turbulent flow with the turbulent energy dissipation rate, ε, as

$$G = \sqrt{\frac{P/V}{\mu}} = \sqrt{\frac{\varepsilon}{\nu}}, \tag{1.4}$$

where P is the power dissipated, V is the volume of a tank and ν is the kinematic viscosity of the fluid. This approach yields the average absolute velocity gradient per unit volume per unit time. The concept proposed by Camp and Stein (1943) for determining the averaged velocity gradient within a system has been

a cornerstone in the design process for many years and the concept has been taught in several textbooks (e.g. Crittenden et al. (2012); Bratby (2016)). Many researcher, including Luo (1997); Bridgeman (2006); Oliveira and Donadel (2019) to name a few, have argued that the approach is flawed as the velocity gradient for a system experiences local zones with a velocity gradient that is much greater compared to the averaged. This is for example the case when studying an impeller stirring in a solution, where the velocity gradient is larger in the vicinity of the impeller (Bridgeman et al., 2010). For this reason, numerous researchers have successfully used CFD to study the velocity gradients and particle aggregation, as the energy dissipation rate is either modelled or resolved locally. Turbulence induced by an impeller or by a hydraulic flocculator is captured locally when using CFD as a tool, which is why it provides a better insight into the design process. In modern times, multiphase simulations, including particle-laden flows, have been developed and researched to a point where they can also be applied to industrial applications. The modelling approach will be further discussed in section 1.6.

1.5 Commonly Used Flocculation Applications

During the destabilisation- and flocculation process, it is necessary to make the adhesive particles collide to form an aggregate. There are several ways to do this depending on the application at hand. If the concentration of particles is sufficiently large and the particles are much smaller than $d_\mathrm{p} \ll 1$ μm, perikinetic aggregation occurs which is due to Brownian motion as the mean-free path is small. This is, however, not the case for most wastewater and water purification plants, where the concentration of particles is too small and the particles are also too large to rely on collision due to Brownian motion. As previously mentioned, particle collisions are mainly driven by orthokinetic aggregation where velocity gradients are induced in the flow due to turbulence.

Shear velocities within the fluid can be introduced in a number of ways, e.g. introducing a mechanical stirrer in a tank, which is illustrated in Fig. 1.10a, where an electric motor is operated to ro-

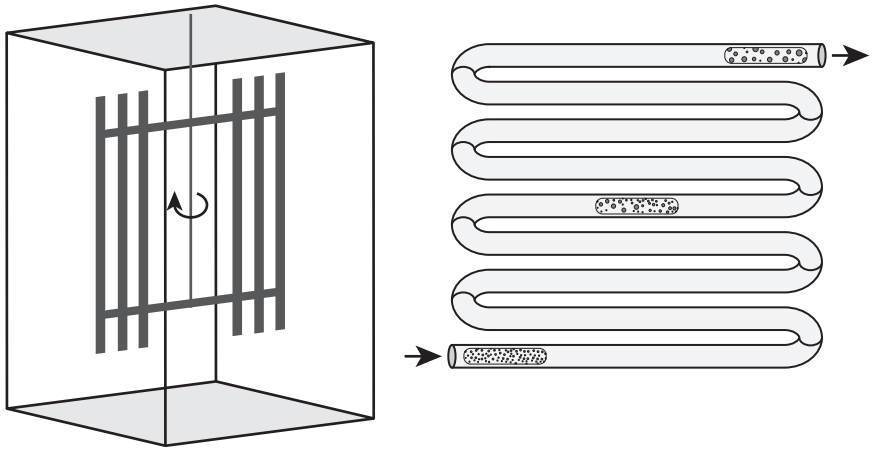

(a) Flocculation tank (b) Pipe flocculator

Fig. 1.10: Two examples of flocculators relying on orthokinetic aggregation. Fig. 1.10a illustrates a flocculation tank where a stirrer induces a shear velocity in the fluid as the motor rotates the stirrer inside the tank. Fig. 1.10b shows a pipe flocculator where the shear velocity is induced by the pipe bends as the fluid moves through the pipe.

tate a stirrer inside a tank. The stirrer then induces a shear velocity inside the application causing the particles to collide and adhere to each other. Another example is a pipe flocculator, illustrated in Fig. 1.10b, where the shear velocity is induced in the fluid by the piping layout. As the fluid moves through the piping, the flow is forced to change direction and this induces turbulence inside the pipe domain, which results in particles colliding. Also, pipe flocculators are often operated in the turbulent regime, $\mathrm{Re_d} > 10,000$, where velocity fluctuations occur naturally.

A flocculation tank is a highly efficient application to make particles aggregate and form large aggregates as the mechanical stirrer is controlled using an electrical motor, but the downside of this application is that it often occupies a large volume and is difficult to operate on a ship due to the movement of the ship, e.g. rolling due to waves. Onboard a ship it is, therefore, more beneficial to use a pipe flocculator, as this has a compact form factor and as the particles are suspended within a turbulent fluid flow, the motion of the ship does not affect the performance of the pipe flocculator.

1.6 Numerical Approach

Simulating the turbulent particle-laden flow using a numerical model allows analysis of different geometrical configurations, different particle properties and more. In-depth data can be produced to study local phenomena which drive and improves the development of the application eventually resulting in a more efficient application. To achieve such a reliable numerical model, an additional focus must be on describing the fluid-particle interaction and particle-particle interaction.

In general, two different approaches can be applied to simulate the fluid-particle flow and a conceptual illustration between the two approaches is shown in Fig. 1.11. The first method is categorised as the Eulerian-Lagrangian approach where the fluid phase is modelled using an Eulerian approach and the discrete particle phase is modelled using a Lagrangian approach tracking each particle. There exists a variety of Lagrangian methods to describe particle-particle interaction which is then coupled to the Eulerian CFD method. A widely used approach is to model the particle phase using a macroscale perspective where several individual particles are lumped together into a parcel. This method is often referred to as the discrete parcel method (DPM) and is commonly used when simulating droplets. When simulating the particle-particle interaction using a mesoscale perspective the length- and time scale must be considered. Molecular dynamics (MD) is commonly used to simulate the particle-particle interaction of nanoparticles. This method is used to accurately capture the collision due to Brownian motion. Molecular dynamics is rarely coupled to CFD as the time scale for nanoparticles is in the order of picoseconds to nanoseconds whereas fluid motion is in the order of microseconds. One method that has gained popularity in recent years is the discrete element method (DEM) originally proposed by Cundall and Strackt (1979), which resolves particle-particle collisions using the analytical expressions for contact stresses by Hertz (1882). The DEM approach considers particles in the order of micrometres to centimetres and is often coupled to CFD as the time scales for fluid motion and particles

are in the same range. Common for the Lagrangian methods is that a large number of Lagrangian particles need to be tracked and handled. When particles become sufficiently small, $d_p < 10$ μm, and when dealing with industrial applications, the number of Lagrangian particles becomes extremely large, e.g. $n_p > 10^9$. To counter the issues with an extreme number of discrete particles, researchers often choose to coarse-grain the micron-sized particles into parcels or simulate a small section of the application. A coarse-grained parcel is then a number of particles lumped together to reduce the number of computational points. Several methods have been developed to maintain the mechanical properties of the solid particles when coarse-graining (Hærvig, 2017), but the author has not found any suitable method to both conserve the mechanical- and adhesive properties of a particle when performing coarse-graining. Due to the problem of not find-

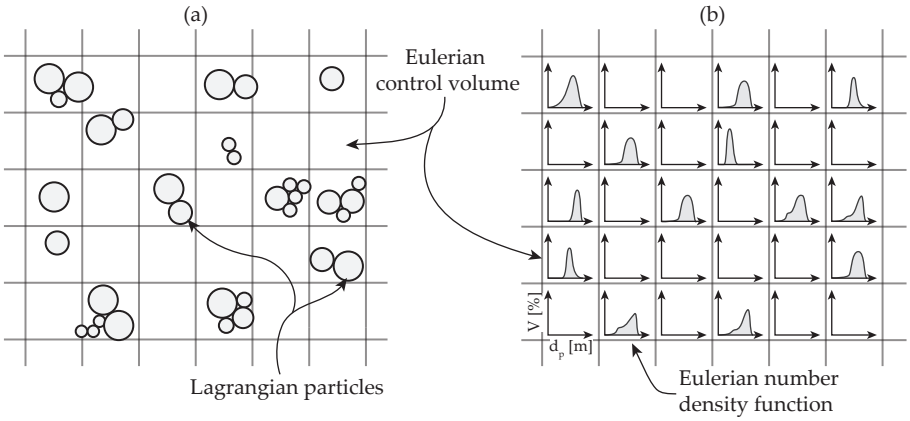

Fig. 1.11: Conceptual illustration of the Eulerian-Lagrangian approach in Fig. 1.11a and the Eulerian-Eulerian approach in Fig. 1.11b.

ing a suitable method to conserve the adhesiveness of particles while coarse-graining, brings up the second category of numerical methods, namely the Eulerian-Eulerian approach. Using this approach both the fluid- and the particle phases are modelled using an Eulerian approach. The size distribution of the particle phase can then be accounted for using the statistical Population Balance Equation (PBE), where the number density function is tracked. The number of equations applied to the computational

domain is thereby bound by the control volumes within the domain. This means that when simulating micron-sized particles in turbulent flows for industrial-scale applications, the particles can be modelled using their actual size and no coarse-graining is necessary.

To summarise the two different approaches; the Eulerian-Lagrangian models provide a more accurate prediction of the particle-particle interaction, but at the cost of computational expenses. This limits the use when dealing with micron-sized particles in industrial applications. Adopting the Eulerian-Eulerian approach fulfils the computational resources available today while maintaining sufficient accuracy to describe dilute particle aggregation in turbulent flows. The present study will employ the Eulerian-Eulerian method where the PBE is used to track the number density function of the particle phase.

1.6.1 Population Balance Equation

The use of the population balance equation has gained popularity over the recent years, as shown in Fig. 1.12. This is due to the fact that the population balance equation can be applied to describe a larger variety of processes and fields e.g. crystallisation, droplet formation, bubbly flows or particulate processes to name a few. Coupling the population balance equation with the multi-fluid Eulerian CFD framework allows particles to change size during the simulation, as the number density function is continuously tracked. The number density function defines the distribution of the dispersed phase for the properties of interest at any given time and space, which, in a general form for a dispersed phase, is given by

$$\frac{\partial}{\partial t} n(\xi, \boldsymbol{x}, t) + \nabla \cdot [\boldsymbol{u}_{\mathrm{d}} n(\xi, \boldsymbol{x}, t)] + \frac{\partial}{\partial \xi} \cdot [\boldsymbol{K}(\xi, \boldsymbol{x}, t)\, n(\xi, \boldsymbol{x}, t)] = S(\xi, \boldsymbol{x}, t)\,. \tag{1.5}$$

Herein ξ denotes the internal coordinate of interest, n is the number density, $\boldsymbol{u}_{\mathrm{d}}$ is the velocity of the dispersed phase and K is the rate of change of the internal coordinate due to a continuous change such as mass and heat transfer, growth, dissolution

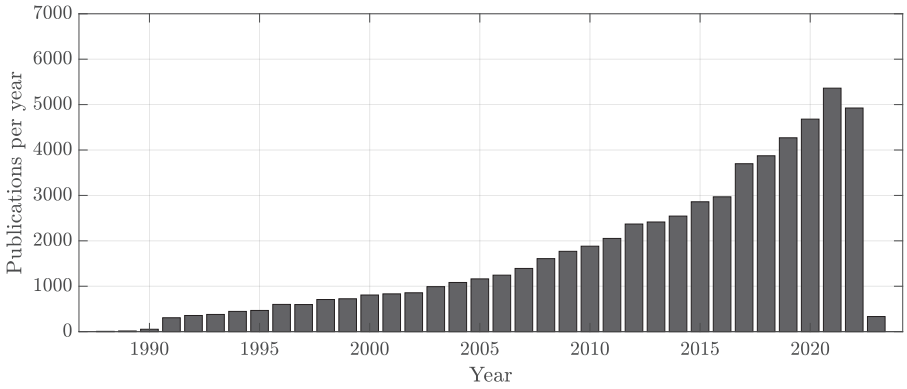

Fig. 1.12: The number of papers published on population balance. Keyword: "population balance" from Web of Science at the time of writing.

and/or chemical reactions. The discontinuous changes due to discrete events, e.g. aggregation and breakage, are handled by the source term, S. As all terms depend on the internal coordinate, spatial coordinate and time, these will be denoted by only the internal coordinate from here on, e.g. $n(\boldsymbol{\xi}, \boldsymbol{x}, t) = n_{\xi}$, for the ease of notation.

The properties of interest, $\boldsymbol{\xi}$, can include e.g. temperature, size, velocity, and composition and if the number density function is a function of only one internal coordinate, $\xi = \xi_1$, the distribution is known as *univariate*. Likewise, if the distribution is a function of two or more internal coordinates, $\boldsymbol{\xi} = (\xi_1, \xi_2, \xi_{...}, \xi_m)$, it is known as *bivariate* and *multivariate*, respectively.

1.6.2 Solution of the Population Balance Equation

Several solution methods have been proposed to solve the population balance equation within the Eulerian-Eulerian CFD framework for polydisperse flows. Three main solution approaches have gained the most attention and are the most widely used: The method of moments (MOM), the quadrature-based moment methods (QBMM) and the class method (CM). Further subcategories of solution methods are found when dealing with the QBMM approaches. To give an overview of the various solution methods, a brief discussion is provided in this section. The choice

of solution method for the population balance equation also depends on the complexity of the shape of the number density function, e.g. whether it is monodisperse, low- or high polydisperse, as shown in Fig. 1.13.

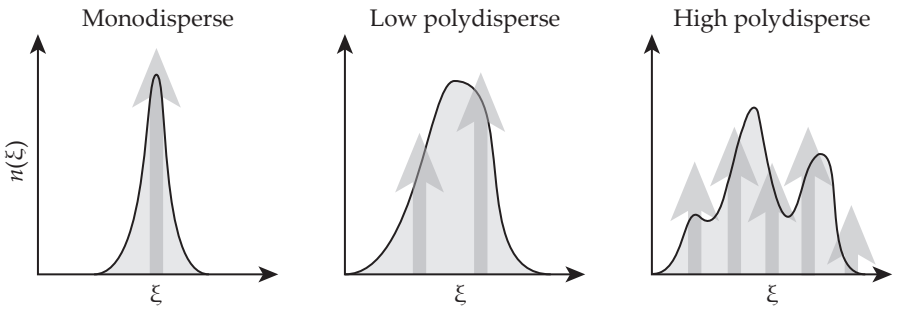

Fig. 1.13: Polydispersity of the dispersed phase number density function as a function of the internal coordinate. Illustration inspired by Shiea et al. (2020).

Method of Moments

A direct solution of the number density function for many engineering solutions often requires solution procedures as the number density function contains much information. This is why Hulburt and Katz (1964) proposed an approximation of the number density function that tracks the evolution of the statistical moments of the number density function instead of the function itself. These moments are defined in their general form as

$$m_{k_1,k_2,\ldots,k_m,k_{m+1},k_{m+2},k_{m+3}} = \int_{\Omega_u}\int_{\Omega_\xi} \xi_1^{k_1}\xi_2^{k_2}\ldots\xi_m^{k_m} u_x^{k_{m+1}} u_y^{k_{m+2}} u_z^{k_{m+3}} f(t,\boldsymbol{x},\boldsymbol{\xi},\boldsymbol{u}) d\boldsymbol{\xi} d\boldsymbol{u} \,. \tag{1.6}$$

The exponent vector, $\boldsymbol{k} = (k_1, k_2, \ldots, k_m, k_{m+1}, k_{m+2}, k_{m+3})$ defines the order of the moment with respect to the internal coordinate of velocity component. The low-order moments have a physical meaning and are generally measurable. As an example, the zeroth order moment defines the number concentration within the system, $m_0 = \xi^0 u_x^0 u_y^0 u_z^0$. The higher-order moments often

cannot be directly measured and therefore might be difficult to interpret. After this transformation of the number density function, the left-hand side is given in terms of moments, however, the right-hand side integral source terms remain unclosed, commonly referred to as the closure problem. As the number density function is transformed into a set of moments, information about the number density function is only available when transforming the moments.

Quadrature-Based Moment Methods

There exists a variety of QBMM approaches to solving the population balance equation, and an overview of some of the more popular ones will be described in this section. The general idea of QBMMs is that the number density function is approximated using an N-node quadrature formula which can be a summation of N weighted kernel functions. These kernels are centred on a node, which is often referred to as an abscissa, of a Gaussian quadrature approximation. One of the most common kernel density functions is the Dirac delta function. This approach was first adopted by McGraw (1997) who used the N-node Gaussian quadrature approximation to solve the univariate population balance equation and then named the approach the quadrature method of moments (QMOM). A similar approach was presented by Marchisio and Fox (2005) who named it the direct quadrature method of moments (DQMOM). Using the DQMOM, the quadrature approximation is transported in time and space to evolve the moments according to their transport equation. One of the main benefits of using the DQMOM is that there is no need for an inversion algorithm. The disadvantage of using both the QMOM and DQMOM is that the distribution function and its shape is not directly available and must be reconstructed from the moments during post-processing.

When working with applications that require continuous reconstruction of the number density function, Yuan et al. (2012) proposed the extended quadrature method of moments (EQMOM), which employs a parametric continuous kernel density

function instead of Dirac delta functions. The kernel density function needs to be chosen for the application at hand. As the kernel density function is not a Dirac delta function, the continuous reconstruction of the number density function contains information about the shape of the number density function. However, it is not always possible to reconstruct the actual shape of the number density function (Yuan et al., 2012, 2014; Madadi-Kandjani and Passalacqua, 2015).

Common to the QBMM approaches is that the integral values and the moments are often presented by the authors and the distribution function is rarely reconstructed. It is thereby difficult to analyse whether the distribution function is polydisperse and if the polydispersity is modelled accordingly.

Class Method

The class method is based on the concept of discretising the internal coordinate into a number of discrete intervals, hence the alternative name *sectional* method. This method provides a direct solution of the number density function in which a set of macroscopic transport equations are solved for the physical domain. As opposed to the MOM and QBMM, the class method is quite intuitive as the number density function is solved in the physical space and also since discretisation is regularly used when solving other non-linear systems. One of the main advantages of using the class method is that the shape of the number density function is readily available at any given time and space. This also means that no pre-defined shape has to be specified, but the interval of internal coordinates needs to be specified by the user.

The direct solution of the discretised number density function comes at the expense of additional computational power compared to the MOM and QBMM, as additional scalar transport equations need to be solved depending on the discretisation. If multiple Eulerian fields, e.g. multiple velocity fields, are introduced, further complexity and transport equations need to be solved which increases the computational demand further. Compared to the QMOM and DQMOM methods, the class method

is more computationally demanding, but when compared to the EQMOM which is also able to predict the continuous shape of the distribution, the class method is comparable in terms of computational time required (Li et al., 2017).

Besides the intuitiveness of the class method, the main advantage of this approach is that the size distribution is directly available at all spatial and temporal coordinates. There is no need for reconstructing the distribution function, as the number density function is solved directly. When compared to experimental results, this makes the validation more convenient, as the distribution function can be compared anywhere within the system. Furthermore, the polydispersity is directly observed when the distribution function is reported and hence it is easy for others to rely on the data. Shiea et al. (2020) report that the QMOM and class method are regarded as the first candidates when dealing with a univariate problem, where the class method is preferred if the number density function can be measured directly within the system. As the particle size is the parameter of interest in this study, the class method is chosen as the solution to the population balance equation. The population balance equation then becomes a univariate problem, where the internal coordinate is the volume of the particles.

1.7 Outline of the Summary Report

The dissertation consists of a summary report based on Papers A-D which describes the methodology and findings more in detail. A graphical overview of the dissertation and papers is shown in Fig. 1.14.

Chapter 1: Presents the background and motivation of the dissertation and introduces the objectives and limitations and discusses possible solution approaches.

Chapter 2: Describes the numerical approach including governing equations, interfacial momentum transfer modelling, particle aggregation and breakage kernels used in the present study.

Chapter 3: Describes the experimental work carried out during the present work. The particle size distribution of the micron-sized particles in the process feed stream is analysed.

Chapter 4: Covers an overview of the main contributions and findings from Papers A-C based on the modelling approach presented in Chapter 2 and fitted to the experimental measurements presented in Chapter 3.

Chapter 5: Provides an overall closure of the summary report and perspectives for future work.

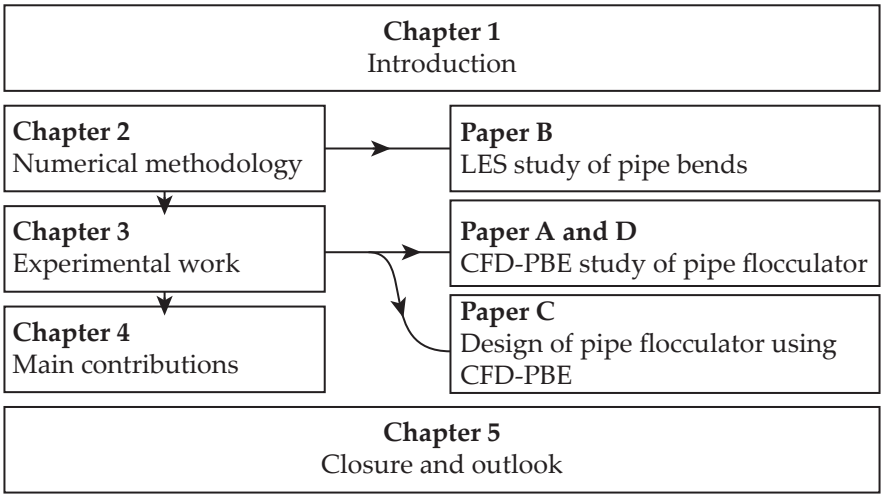

Fig. 1.14: Graphical overview of the structure of the dissertation.

1.8 Outline of Publications

The list provided gives a brief overview of the papers published in relation to this dissertation. The papers, in their full length, are found in Part II.

Paper A: On the agglomeration and breakage of particles in turbulent flows through pipe bends using CFD-PBE

Chemical Engineering Science, Vol. 260, 117915

Aggregation and breakage of solid particles subject to a turbulent flow in the range of $15,000 \leq \mathrm{Re_d} \leq 35,000$ are investigated for different bend radii of a hydraulic pipe flocculator using CFD-PBE. A methodology for describing aggregation and breakage of solid particles while including interfacial momentum transfer between the two phases is presented using the class method implemented in the open-source CFD library OpenFOAM. A parametric study is performed to tune the parameters to reproduce a particle size distribution obtained from experimental measurements performed in the Alfa Laval Test and Training centre. The results showed that as the Reynolds number increases, the particle size distribution decreases. When more turbulence is induced in the flow, particles are more prone to breakage. As a result, when the Reynolds number exceeded $\mathrm{Re_d} > 30,000$, the impact of the bend radius became negligible, as a naturally high magnitude of turbulence is already present inside the pipe flow.

Paper B: On the downstream effects of fully developed turbulent flows through 180° pipe bends

Physics of Fluids, Vol. 35

Several large eddy simulations were carried out for a pipe flow with a 180° pipe bend with bend radii of $1 \leq r_\mathrm{b}/d_\mathrm{h} \leq 3.375$ at a Reynolds number of $\mathrm{Re_d} = 10,000$. A fully developed turbulent profile is applied at the inlet boundary condition to study the downstream turbulence characteristics for the different bend radii. The LES model is validated against experimental- and DNS data from the literature for a straight pipe and an infinitely long curved pipe, respectively. Secondary flows are induced by the pipe bend and these increase in magnitude as the bend radius decreases. It is shown how the secondary motions decay when the flow moves downstream from the bend and negligible differences in secondary motions for the different bend radii are observed at a downstream location of $x/d_\mathrm{h} = 4$. Furthermore, it is shown how the recovery length of the velocity profile de-

creases as more turbulence is induced by decreasing the bend radii, meaning that the recovery of the velocity profile is driven by turbulence transport.

Paper C: On the design of compact hydraulic pipe flocculators using CFD-PBM

Chemical Engineering Research and Design (**Under review**)

In the paper, various geometrical parameters of a hydraulic pipe flocculator are investigated by applying the presented CFD-PBE approach presented in Paper A. A total of 123 configurations are simulated at a Reynolds number of $\mathrm{Re_d} = 20,000$ and the volume-averaged Sauter mean diameter is presented for all simulations. The results showed that the bend radius has the single-largest impact on the final particle size. Furthermore, it was shown how the particles increase linearly in the straight sections of the configurations, which is why it is favourable to have a long straight pipe within the configuration. Helically coiled designs showed promising results due to the fixed curvature, however, it was indicated that the bend radius needed to be larger than the applied range of bend radii.

Paper D: Aggregation and breakage of solid particles in a turbulent flow through a 90° pipe bend using CFD-PBE

17th OpenFOAM Workshop, Cambridge University, 2022

The CFD-PBE model presented in Paper A was applied to study the aggregation and breakage of particles through a 90° bend. As the modelling framework is carried out using OpenFOAM, this paper was presented at the OpenFOAM Workshop and a tutorial for showcasing the modelling framework was supplied. The tutorial was later accepted by the OpenFOAM Foundation to become a standard tutorial within the multifluid Eulerian framework. In the paper, it is shown how the aggregates break over the 90° bend but that they will rebuild and aggregate further as they move downstream from the bend.

2 | Modelling Approach

To model the aggregation and breakage of solid particles suspended in a fluid flow, both the fluid- and the particle phase must be resolved and coupled. Within the Eulerian framework force models have to be applied to the fluid-solid interface in order to account for the momentum of the fluid forces acting on the particles. Therefore a two-way coupling is required where momentum is exchanged between the two phases. In order to reproduce the particle size distribution, the aggregation- and breakage models are fitted to experimental data obtained from the Alfa Laval Test and Training Centre and the procedure for this is explained further in Chapter 3.

2.1 Particle Properties

During the combustion of fuel oil in the engine, soot is formed which is then transferred from the dry exhaust gas to the water inside the scrubber. During this process, the morphology and size of the particles change and this section clarifies the properties and assumptions related to the particle phase.

After soot has been formed inside the combustion cylinder in the engine, it appears as a fractal of low order. Trivanovic et al. (2019) performed measurements on diesel soot aggregates from the combustion of natural gas (NG) and diesel using a dual-fuelled marine engine with a nominal load of 4320 kW. Transmission Electron Microscopy (TEM) images of the soot aggregates from various loads are shown in Fig. 2.1 and it is shown that the soot aggregates are loosely coupled in the gas phase. The aggre-

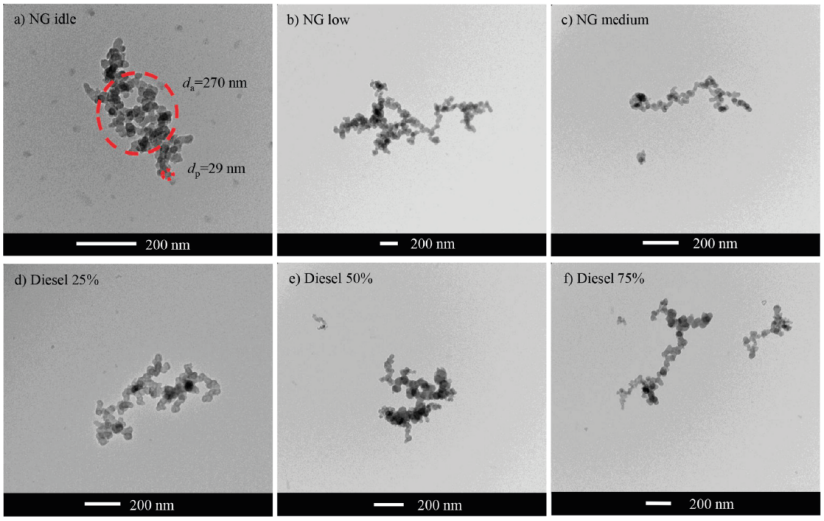

Fig. 2.1: TEM images of soot aggregates from a duel-fuelled marine engine with a nominal load of 4320 KW. Images are taken when the engine was operated using natural gas (NG) in idle mode (2.1a), at low load (2.1b), at medium load (2.1a) and when the engine was operated using diesel at 25 % (2.1d), at 50 % (2.1e) and 75 % (2.1f). Reprinted from Trivanovic et al. (2019).

gates are therefore described as having a low fractal dimension. A conceptual illustration of the fractal dimension, D_f, is seen in Fig. 2.2. Tightly coupled aggregates with a fractal dimension of $D_f = 3$ are stronger compared to aggregates with a fractal dimension of $D_f = 1$ as the number of interconnections is larger. This also means that aggregates with the same number of primary particles have a smaller effective diameter as the aggregates have a more compact form.

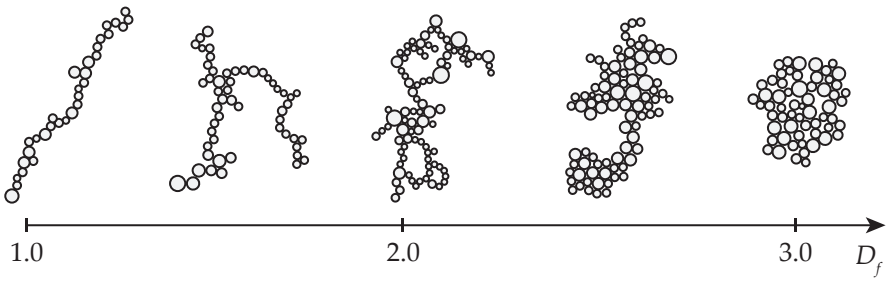

Fig. 2.2: Conceptual illustration of fractal dimensions. Loosely coupled aggregates on a single line are of a low fractal dimension ($D_f = 1$) and compact coupled aggregates that resemble spheres are of a high fractal dimension ($D_f = 3$).

When soot particles are exposed to a wet environment, Mikhailov et al. (2006) and Ma et al. (2013) show how the soot aggregates change morphology and become more tightly coupled and become a higher-order fractal. Fig. 2.3 shows the TEM images of Mikhailov et al. (2006) where soot particles are exposed to an environment with relative humidity (RH) of 10 % and 100 %. The soot particles collapse and form compact aggregates that are quite spherical. Fig. 2.4 show similar TEM images from Ma et al. (2013) of soot particles that have been exposed to water and then the water is evaporated from the soot particle before TEM images are taken. Again, it is shown that the soot particle collapses and forms a compact spherical-like aggregate with high fractal order. As it is shown that soot particles in wet environments change morphology to compact spherical-like aggregates, it is assumed that soot particles are spherical in this study.

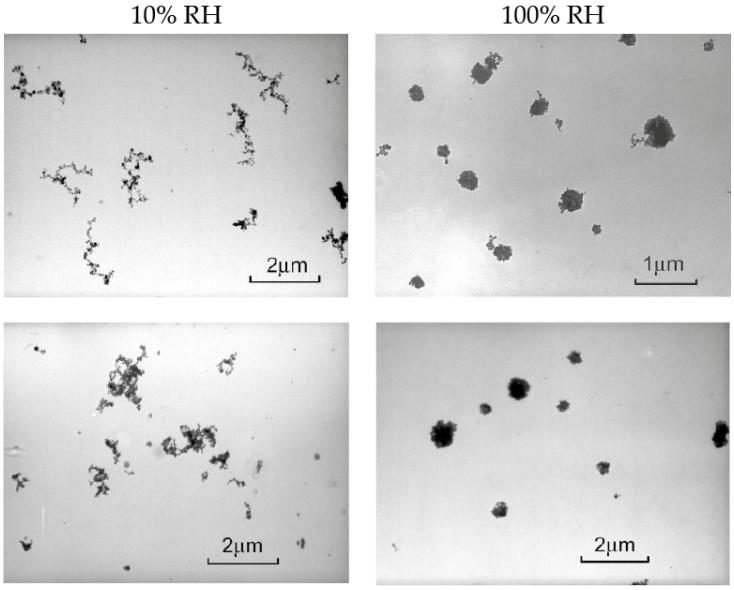

Fig. 2.3: TEM images of soot aggregates from a diffusion acetylene burner in an environment with RH = 10 % (left) and RH = 100 % (right). Reprinted from Mikhailov et al. (2006).

Zoltan Jenei et al. (2018) report that diesel soot primarily consists of graphite and determines a true density of 2100 kg/m^3. As soot aggregates are porous structures, the individual particle will

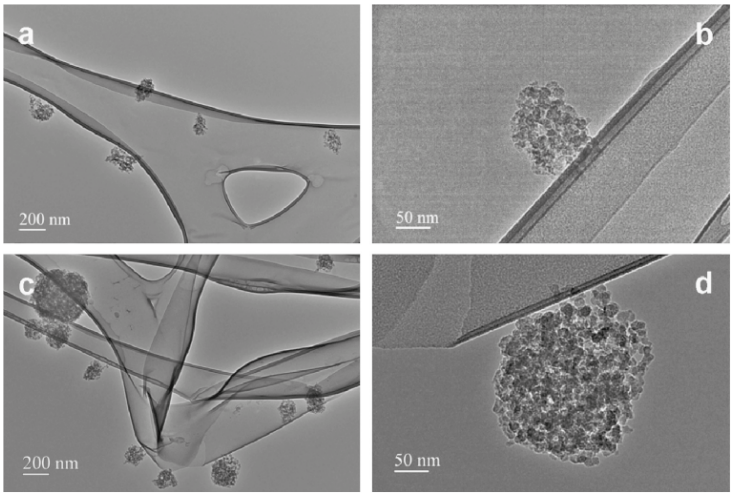

Fig. 2.4: TEM images of collapsed soot from a burner using ethylene as a fuel after being exposed to water and then dried during a rapid evaporation process. Reprinted from Ma et al. (2013).

not be solid and the density is therefore adjusted to account for the fluid occupying some of the volumes. Density measurements performed on diesel soot show good agreement using a bulk density of $\rho_\mathrm{p} = 1400\ \mathrm{kg/m^3}$ giving the density ratio between the particle and fluid phase of $\rho_\mathrm{p}/\rho_\mathrm{f} = 1.4$, as the process fluid is water.

2.2 Population Balance Equation

The population balance equation is used to track the spatial and temporal evolution of the number density function, as mentioned in Sec. 1.6. In the present work, the continuous change of the internal coordinate due to growth, nucleation or other phenomena will be neglected and only the discrete events due to aggregation and breakage will be included. Furthermore, particle size is the parameter of interest resulting in the internal coordinate becoming the volume of the particles, $\xi = v$, giving the number density function

$$\frac{\partial n_v}{\partial t} + \nabla \cdot (\boldsymbol{u}_\mathrm{p} n_v) = S_v \,. \tag{2.1}$$

These simplifications lead to a univariate system where it is assumed that all particles share the same velocity field, $\boldsymbol{u}_\mathrm{p}$. This assumption is acceptable if the inertia of the particles is small if the size distribution is sufficiently narrow and if collisions are not important. The discontinuous changes are handled by the source term which is defined as

$$S_v = \underbrace{\frac{1}{2}\int_0^v n_{v'} n_{v-v'} a_{v',v-v'} \mathrm{d}v'}_{\text{Aggregation, birth}} - \underbrace{n_v \int_0^\infty n_{v'} a_{v,v'} \mathrm{d}v'}_{\text{Aggregation, death}} \tag{2.2}$$

$$+ \underbrace{\int_v^\infty n_{v'} b_{v'} \beta_{v,v'} \mathrm{d}v'}_{\text{Breakage, birth}} - \underbrace{n_v b_v}_{\text{Breakage, death}} . \tag{2.3}$$

Herein, $a_{v',v-v'}$ denotes the corresponding aggregation frequency and $b_{v'}$ denotes the total breakage frequency. The information about the fragments created during breakage is handled by the daughter size distribution function $\beta_{v,v'}$, which is further described in Sec. 2.2. A conceptual illustration of the birth and death of particles due to aggregation and breakage is shown in Fig. 2.5. As reported in Sec. 1.4 on page 13, both aggregation and breakage of particles are driven by velocity gradients in the continuous phase. Velocity gradients are an expression of the turbulence induced in the fluid. Turbulence modelling when using CFD is described in Sec. 2.4 on page 39.

As the number density function in Eq. (2.1) is solved using the class method, as described in Sec. 1.6.2 on page 20, it is discretised into a number of discrete size classes and solved directly. The number density function is integrated over the volumes yielding the number concentration

$$N_i = \int_{v_i}^{v_{i+1}} n_v \mathrm{d}v \tag{2.4}$$

for each discretised size class. The number density function is

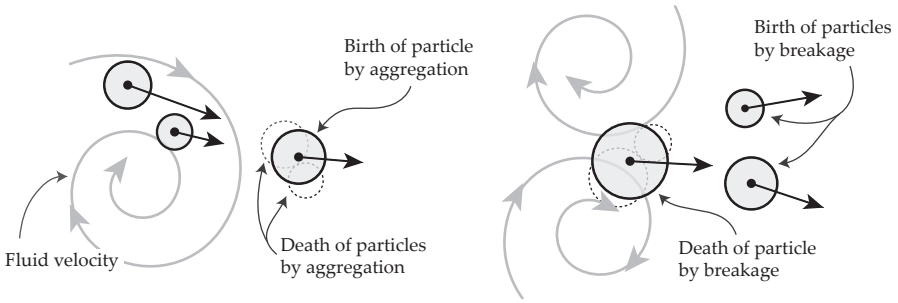

Fig. 2.5: Conceptual illustration of birth and death of particles due to aggregation and breakage caused by fluid velocity gradients.

then solved for each discrete size class as

$$\frac{\partial N_i}{\partial t} + \nabla \cdot \left(\boldsymbol{u}_\mathrm{p} N_i \right) = S_i \,. \tag{2.5}$$

Kumar and Ramkrishna (1996) proposed to solve the population balance equation by assuming the population is concentrated at pivotal volumes, x_i. Lehnigk et al. (2021) implemented this solution into the open-source CFD library OpenFOAM and discretised the pivotal volumes as $v_i = (x_i + x_{i-1})/2$, also shown in Fig. 2.6.

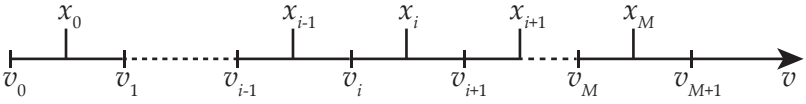

Fig. 2.6: Discretisation of the volumes using pivotal volumes, x_i, into a total of M size classes. Illustration by Lehnigk (2020).

Aggregation kernel

Birth and death of new particles due to aggregation from Eq. (2.2) is handled using an aggregation frequency by a kernel. The kernel proposed by Adachi et al. (1994) has been successfully used by Marchisio et al. (2003) to describe the aggregation of particles in turbulent flows. This kernel is adopted in the present study and implemented in the multi-fluid Eulerian framework of OpenFOAM. The aggregation frequency for solid particles is

given by

$$a_{d,d'} = \frac{4}{3}\sqrt{\frac{3\pi}{10}}\sqrt{\frac{\varepsilon}{\nu}}\,(d+d')^3 \ , \tag{2.6}$$

where d and d' are the diameters of the colliding particles. The aggregation frequency for different energy dissipation rates is shown in Fig. 2.7 for a particle of $d_\mathrm{p} = 10$ μm colliding with particles in the range of 1 μm to 1000 μm.

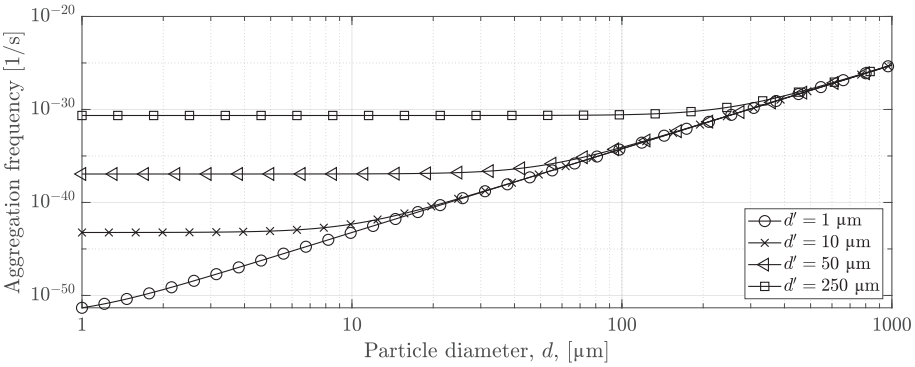

Fig. 2.7: Aggregation frequency for a constant turbulent dissipation rate of $\varepsilon = 0.1$ m^2/s^3 for particles with different diameters colliding with particles between 1 μm and 1000 μm.

Breakage kernel

Birth and death of particles due to breakage in Eq. (2.2) is handled by calculating a breakage frequency. Kusters (1991) proposed an exponential relationship of the breakage frequency based on a maximum particle strength. As previously described, flocculation and aggregation of particles have a historical usage of energy dissipation rate, ε, which is also why the exponential kernels is based on the turbulent energy dissipation rate. The breakage kernels are given as

$$b_{v'} = \sqrt{\frac{4}{15\pi}}\sqrt{\frac{\varepsilon}{\nu}}\exp\left(-\frac{\varepsilon_\mathrm{cr}}{\varepsilon}\right) \ , \tag{2.7}$$

where ε_cr is the critical energy dissipation rate required for an aggregate to break. This critical energy dissipation rate is defined

as

$$\varepsilon_{\mathrm{cr}} = \frac{B}{r_{\mathrm{c}}}\,, \tag{2.8}$$

where B is a strength coefficient determined by experimental measurements and r_{c} is the collision radius. Mandelbrot (1985) proposed the relation for the collision radius as a function of the fractal dimension, D_{f} of the aggregate, as

$$r_{\mathrm{c}} = r_0 \left(\frac{n_i}{k_{\mathrm{c}}}\right)^{1/D_{\mathrm{f}}}\,. \tag{2.9}$$

Herein r_0 is the radius of the primary particles of the aggregate and n_i is the number of primary particles within the aggregate and k_c is a constant relative to packing, which is often assumed unity (Jeldres et al., 2017). Even though the particles are assumed spherical when modelling the interfacial momentum exchange, it is assumed advantageous to consider the fractal dimension of the particles in terms of inter-particle strength. The number of primary particles within an aggregate is defined using the radius of the aggregate, r_i, as

$$n_i = \left(\frac{r_i}{r_0}\right)^{D_{\mathrm{f}}}\,. \tag{2.10}$$

Plotting the aggregation and breakage frequencies in Fig. 2.8 for particles within the range of $1\,\mu\mathrm{m} \leq d_{\mathrm{p}} \leq 1000\,\mu\mathrm{m}$, a primary particle size of $d_0 = 250$ nm, a fractal dimension of $D_{\mathrm{f}} = 2.4$, a particle strength coefficient of $B = 50 \cdot 10^{-7}\ \mathrm{m}^3/\mathrm{s}^3$ for energy dissipation rates of $0.01 < \varepsilon < 0.3$ shows how the exponential breakage kernel activates for the different size groups. Using this breakage kernel shows that larger aggregates are more prone to breakage compared to smaller aggregates.

As new particles are formed due to breakage, the newly formed particles have to be specified by a daughter size distribution function.

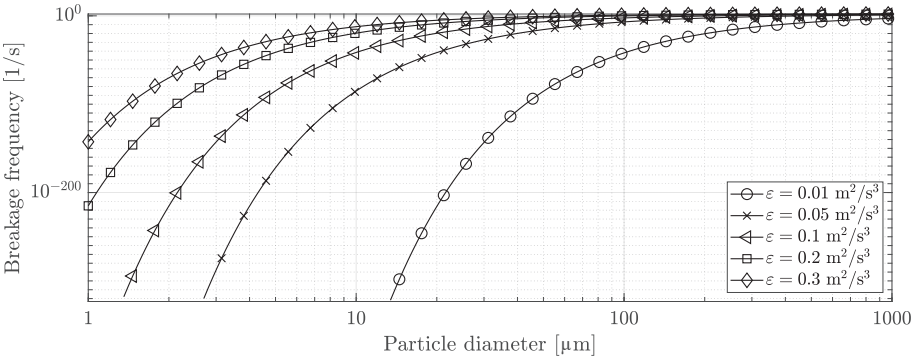

Fig. 2.8: Breakage frequency for particles between 1 μm and 1000 μm for different energy dissipation rates. The breakage frequency is calculated based on a primary particle size of d_0 = 250 nm, a strength parameter of $B = 50 \cdot 10^{-}7$ m^3/s^3 and a fractal dimension of D_f = 2.4.

Daughter size distribution

The daughter size distribution must satisfy the following volumetric constraints

$$\int_0^{v'} v\beta_{v,v'}\mathrm{d}v = v' \,, \tag{2.11}$$

$$\int_0^{v'} v\beta_{v,v'}\mathrm{d}v = \gamma \,, \tag{2.12}$$

where γ is the number of daughter particles born during breakage. These constraints are made to conserve the volumetric continuity of the particle phase during breakage. In this study, the discretised beta distribution function by Laakkonen et al. (2007) is applied. The discretised beta distribution function is given by

$$\beta_{v,v'} = (1 + C_4)(2 + C_4)(3 + C_4)(4 + C_4)\left(\frac{1}{3}\right)\left(\frac{1}{v'}\right)\left(\frac{v}{v'}\right)^2\left(1 - \frac{v}{v'}\right)^{C_4} , \tag{2.13}$$

where the coefficient C_4 is a function of the number of daughter particles produced during a breakage event, defined as

$$C_4 = 3n_i - 4 \tag{2.14}$$

where n_i is the number of daughter particles born at a breakage. Bilde et al. (2022) perform a sweep of multiple parameters and show that a binary breakage coefficient $C_4 = 2$ produces a particle

size distribution that is in good agreement with the experimentally measured particle size distribution described in Chapter 3. The normalised daughter size distribution function by Laakkonen et al. (2007) is shown in Fig. 2.9.

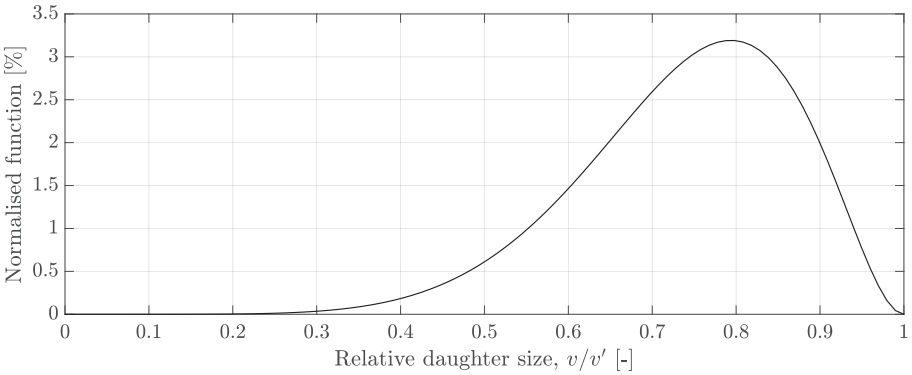

Fig. 2.9: Daughter size distribution function of Laakkonen et al. (2007) with a binary coefficient of $C_4 = 2$.

2.3 Governing equations for Continuity and Momentum

The continuity equation for each phase using the two-fluid Eulerian method is given by

$$\frac{\partial \left(\alpha_\varphi \rho_\varphi\right)}{\partial t} + \nabla \cdot \left(\alpha_\varphi \rho_\varphi \boldsymbol{u}_\varphi\right) = S_\varphi \tag{2.15}$$

where S_φ is the source term representing all mass sources and mass transfer terms, including those due to breakage and aggregation.

The momentum equation for each phase is given by

$$\frac{\partial \alpha_\varphi \rho_\varphi \boldsymbol{u}_\varphi}{\partial t} + \nabla \cdot \left(\alpha_\varphi \rho_\varphi \boldsymbol{u}_\varphi \boldsymbol{u}_\varphi\right) - \nabla \cdot \boldsymbol{\tau}_\varphi = -\alpha_\varphi \nabla p + \alpha_\varphi \rho_\varphi \boldsymbol{g} + \boldsymbol{M}_\varphi + \mathbf{S}_\varphi \tag{2.16}$$

where α is the mass fraction of the species, $\boldsymbol{g}$ is the gravitational acceleration, $\boldsymbol{\tau}$ is the shear stress tensor of the phase and $\boldsymbol{M}$ is the interfacial momentum transfer further described in Sec. 2.5.

It is assumed that the phases share the same pressure, which is why there is no difference in pressure for the continuous and dispersed phases. When modelling the continuous phase using the RANS approach, the stress tensor of the phase includes the Reynolds stresses and these needs to be modelled by choosing an appropriate model for the given system further described in Sec. 2.4.

2.4 Turbulence Modelling

As previously mentioned, turbulence can be categorised into three overall categories: RANS, LES and DNS. Besides these overall categories, hybrid turbulence models exist where RANS and LES are combined, e.g. the Detached Eddy Simulation (DES) of Strelets (2001). These turbulence models provide closure for the Navier-Stokes equation as expressions for the velocity fluctuations of the fluid are described. When using DNS, all of the eddies in the energy cascade in Fig. 2.11 are resolved, whereas the LES model resolves the largest eddies and models the smallest eddies in the Kolmogorov subrange. The smallest eddies are modelled using a subgrid-scale (SGS) model, where numerous models are presented in the literature. When using the RANS approach, only the mean velocity is considered, as the instantaneous velocity, u, is divided into a mean velocity, $\overline{u}$ and a fluctuating velocity, u', as $u = \overline{u} + u'$. The velocity fluctuations are then modelled as the so-called Reynolds stress (Reynolds, 1895) which is a tensor defined as

$$\boldsymbol{\tau}_{\mathrm{R}} = -\rho\overline{\boldsymbol{u}'\boldsymbol{u}'}\,. \tag{2.17}$$

A comparison of the velocity field when using RANS and LES turbulence models is shown in Fig. 2.10. The mean velocity is shown in Fig. 2.10a whereas the velocity fluctuations and thereby the largest eddies are visualised in the velocity field when using the LES turbulence approach in Fig. 2.10b.

Particle aggregation and breakage are driven by the turbulent eddies in the fluid, as illustrated in Fig. 2.5 on page 34. The energy spectrum in Fig. 2.11 shows that the eddies carrying the most ki-

Fig. 2.10: Velocity field for a simulation of a jet using a RANS turbulence model in Fig. 2.10a and a LES turbulence model in Fig. 2.10b. The RANS model considers only the mean velocity whereas the largest velocity fluctuations are resolved in the LES model.

netic energy are eddies with a low wavenumber. It is therefore the large eddies that cause particle aggregation and breakage, which is why RANS and LES models are favourable in this study. The smallest scale of turbulence is resolved when using DNS, but these small eddies do not have a significant impact on the particle phase in terms of aggregation and breakage. Furthermore, DNS requires a dense computational mesh with a cell size of $y^+ < 1$ in the entire computational domain. For highly turbulent flows, multiphase flows and industrial applications, DNS is not yet feasible, even with modern high-performance computers. Therefore, RANS and LES are considered for the present study and a description of the turbulence models is presented in the following sections.

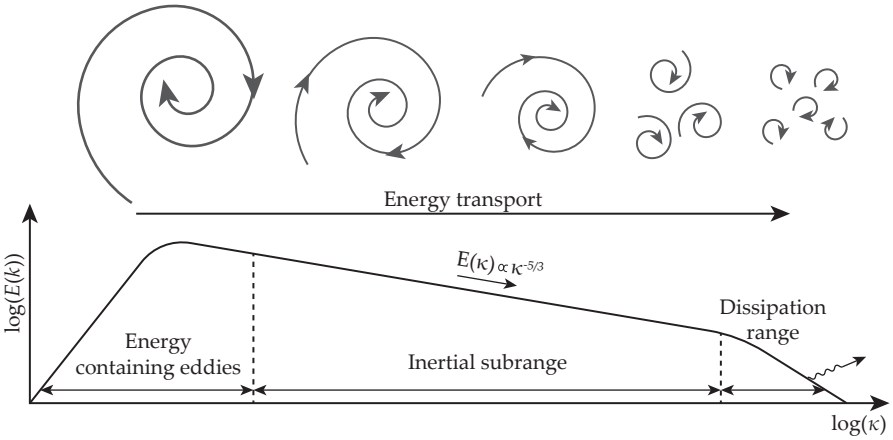

Fig. 2.11: Energy spectrum as a function of the wavenumber, κ for turbulent eddies. Conceptual understanding of how the kinetic energy of eddies dissipates into smaller eddies and eventually into heat. According to Kolmogorov's law, the energy spectrum experience a $-5/3$ decay in the inertial subrange (Kolmogorov, 1941a,b).

2.4.1 Reynolds Averaged Navier-Stokes

As the RANS approach solves the mean velocity in the fluid flow, the velocity fluctuations are modelled, as previously mentioned. The governing momentum equation for the multi-fluid Eulerian approach in Eq. 2.16 includes a stress tensor which includes the Reynolds stress in Eq. 2.17. The Reynolds stress tensor is symmetric and represents the correlation between the fluctuating velocity and is hence unknown. The RANS equations have a closure problem and additional modelling is needed to solve the Reynolds stress. Numerous models are presented in the literature for solving the Reynolds stress, where some of the most widely used is the group of k-ε models, the group of k-ω and the SST models which are all linear eddy viscosity models. These are widely used, as most of these models are presented as a 2-equation turbulence model and the computational demand is thereby relatively low while maintaining sufficient prediction capabilities. Another widely used group of turbulence models is the Reynolds Stress Model (RSM), which is a 6-equation closure model. Various methods for modelling the Reynolds stress transport have been presented throughout the literature, where two

commonly used RSM models are presented by Launder et al. (1975) and Speziale et al. (1991).

The choice of turbulence model often depends on the application at hand. In the present study, the flow inside a pipe and the swirling motion induced by the pipe bend are of interest. Kim et al. (2014) performed CFD analysis of the flow within a 90° pipe bend and compared different RANS turbulence models to the experimental data of Sudo et al. (1998). Some of the most widely used linear eddy viscosity RANS models were applied, including the standard k-ε model, the extended k-ε model, the RNG k-ε model and the k-ω SST model. Furthermore, non-linear eddy viscosity models were also applied and analysed, including the Lien cubic k-ε model and the Launder-Sharma low Reynolds number k-ε model among others. In general, Kim et al. (2014) concluded that the RNG k-ε model gives good agreement for the streamwise velocity and secondary swirl velocity profiles. Similarly, Hilgenstock and Ernst (1996) compared the standard k-ε turbulence model and the RNG k-ε to experimental data and concluded that the RNG k-ε produces better results for the swirling flow motion. Escue and Cui (2010) also performed CFD analysis of the flow in a swirling pipe flow and compared the RNG k-ε turbulence model to the RSM model. The downstream velocity and turbulence profiles were compared to experimental data of Rocklage-Marliani et al. (2003). For lower swirl numbers it was reported that the RNG k-ε was superior in terms of predicting the velocity profile and as the swirl number increases a similar performance was observed from the two turbulence models. The authors also report that both the RNG k-ε model and the RSM seemed to have unrealistic decay of turbulence downstream. As secondary swirls are present in the pipe flow with bends, the RNG k-ε is reported to be the best-suited turbulence model when predicting the velocity field for these applications and is, hence, used in the present study.

2.4.2 Large Eddy Simulation

When observing Fig. 2.10 the difference between RANS and LES is immediately visible as the largest eddies are directly observable within the velocity field. A cut-off value is introduced in the energy spectrum in Fig. 2.11 where eddies become too small to resolve and are instead modelled using the SGS model. The earliest SGS model was proposed by Smagorinsky (1963) for LES simulations and has since then been applied numerous times in LES studies. Several other SGS models have been presented and used in various studies, including the one-equation SGS model of Yoshizawa (1998), the dynamic one-equation model of Kim and Menon (1995), the dynamic Smagorinsky model of Germano et al. (1998) and the wall-adapting local-eddy (WALE) viscosity SGS model of Nicoud and Ducros (1999). The WALE model automatically adjusts the sub-grid scale eddy-viscosity at the wall to zero, meaning no dynamic constant adjustments or damping functions are needed to correct for the walls. As a result, the WALE model is well-suited for wall-bounded flows and has been used in numerous studies. Several studies have compared the results from the Smagorinsky- and WALE SGS model and concluded that the WALE model describes the turbulence properties more accurately when compared to experimental data (Weickert et al., 2010; Shukla and Dewan, 2019; Salehi et al., 2020). The WALE model is further described in Paper B.

2.5 Interfacial Momentum Transfer

Various forces are important when predicting the motion of particles in a turbulent flow. As the size of the particles is modelled using the population balance equation and the governing equations for the particle phase are performed using an Eulerian approach, the important force contributions are discussed in the following section. The interfacial momentum transfer requires modelling of the individual force contributions and, in this study, it is given

as

$$\boldsymbol{M}_{\varphi} = \sum_{\varphi=0,\varphi\neq\psi}^{N} \left(\boldsymbol{F}_{\mathrm{D},\varphi\psi} + \boldsymbol{F}_{\mathrm{L},\varphi\psi} + \boldsymbol{F}_{\mathrm{VM},\varphi\psi} + \boldsymbol{F}_{\mathrm{disp},\varphi\psi} \right) , \tag{2.18}$$

where F_{D} is the drag force, F_{L} is the lift force, F_{VM} is the virtual mass force, F_{disp} is the turbulent dispersion force and subscripts φ and ψ denote the individual phases. It should be noted that the turbulent dispersion force should only be included in the interfacial momentum transfer when turbulence is modelled using the RANS approach. It is noteworthy to add that $M_{\varphi\psi} = -M_{\psi\varphi}$ for a two-fluid system, such as in this study, and that

$$\sum_{\varphi=0}^{N} \boldsymbol{M}_{\varphi} = 0 \tag{2.19}$$

is required to conserve momentum. The different fluid-particle forces included in the present study are illustrated in Fig. 2.12.

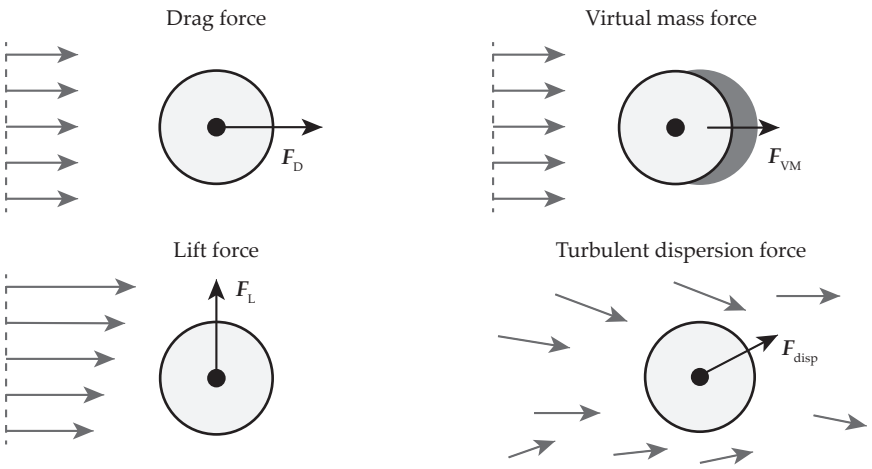

Fig. 2.12: Conceptual illustration of the fluid-particle forces included in this study. The grey arrows indicate the fluid velocity and the black arrows indicate the force acting on the particle.

Drag force

As a velocity difference occurs between the particle and fluid phase, a resistant opposing force relative to the surrounding fluid

is applied, more commonly referred to as the drag force. This force is governed by the shape of the particles and the viscous shear stresses in the fluid at the surface of the particles and the drag force is given as

$$\boldsymbol{F}_{\mathrm{D}} = -\frac{3}{4} C_{\mathrm{D}} \rho_{\mathrm{f}} \frac{\alpha_{\mathrm{f}}}{d_{\mathrm{p}}} \left| \boldsymbol{u}_{\mathrm{p}} - \boldsymbol{u}_{\mathrm{f}} \right| \left(\boldsymbol{u}_{\mathrm{p}} - \boldsymbol{u}_{\mathrm{f}} \right) , \tag{2.20}$$

where C_{D} is the drag force coefficient. Often, the drag force is related to using the particle Reynolds number, which is defined as

$$\mathrm{Re}_{\mathrm{p}} = \frac{\left| \boldsymbol{u}_{\mathrm{p}} - \boldsymbol{u}_{\mathrm{f}} \right| d_{\mathrm{p}}}{\nu_{\mathrm{f}}} . \tag{2.21}$$

In the multi-fluid model, the drag force is therefore often defined as

$$\boldsymbol{F}_{\mathrm{D}} = -\frac{3}{4} \frac{\alpha_{\mathrm{p}} \rho_{\mathrm{f}} \nu_{\mathrm{f}}}{d_{\mathrm{p}}^2} C_{\mathrm{D}} \mathrm{Re}_{\mathrm{p}} \left(\boldsymbol{u}_{\mathrm{p}} - \boldsymbol{u}_{\mathrm{f}} \right) \tag{2.22}$$

The shape of the particles is important as this influences the pressure distribution and the downstream turbulence. A suitable drag force coefficient needs to be chosen based on the assumed shape of the particles. As the particles are assumed spherical in this study, several suitable models have been proposed. Since the particle phase is dilute, the drag force coefficient model of Wen and Yu (1966) is chosen and is given by

$$C_{\mathrm{D}} = \begin{cases} \frac{24}{\mathrm{Re}_{\mathrm{p}}} \left(1 + 0.15 \mathrm{Re}_{\mathrm{p}}^{0.687} \right) \alpha_{\mathrm{f}}^{-2.65} & \text{for } 0.5 \leq \mathrm{Re}_{\mathrm{p}} < 1000 \\ 0.44 \alpha_{\mathrm{f}}^{-2.65} & \text{for } \mathrm{Re}_{\mathrm{p}} \geq 1000 \, . \end{cases} \tag{2.23}$$

Lift force

Rotations within the fluid flow are often experienced when dealing with turbulent flows and whenever such a rotational fluid velocity is experienced by the dispersed particles, a lift force perpendicular to the fluid flow is enforced on the particles. The lift force is given as

$$\boldsymbol{F}_{\mathrm{L}} = -C_{\mathrm{L}} \rho_{\mathrm{f}} \left(\boldsymbol{u}_{\mathrm{p}} - \boldsymbol{u}_{\mathrm{f}} \right) \cdot \boldsymbol{\omega} , \tag{2.24}$$

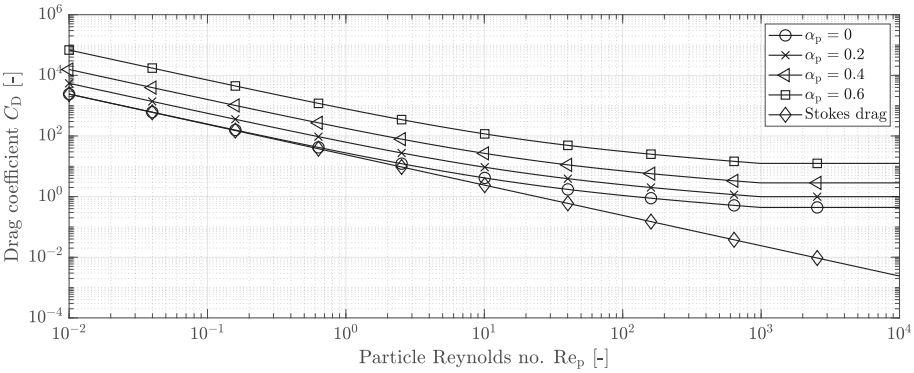

Fig. 2.13: Drag force coefficient proposed by Wen and Yu (1966) alongside the Stokes drag for spherical particles $C_D = 24/Re_p$.

where C_L is the lift force coefficient and $\boldsymbol{\omega}$ is the vorticity of the fluid velocity defined by the curl operator as $\boldsymbol{\omega} = \nabla \times \boldsymbol{u}_f$. As for the drag force coefficient, the lift force coefficient depends on the shape of the particles. As spherical particles are assumed in this study, a low pressure is experienced on the side where the highest velocity is observed, resulting in the particle moving in the direction of the low pressure. Saffman (1965) proposed the relationship for the lift force coefficient for spherical particles at low Reynolds numbers as

$$C_L = \frac{3}{2\pi\sqrt{Re_\omega}} C'_L \,, \tag{2.25}$$

where $C'_L = 6.46$ and the Reynolds vorticity number is given as $Re_\omega = |\boldsymbol{\omega}|\, d_p^2/\nu_f$. Mei (1992) extended the work of Saffman (1965) for the lift force coefficient to cover a wider range of finite Reynolds numbers. This relationship is often referred to as the Saffman-Mei lift force coefficient and is given as

$$C'_L = \begin{cases} 6.46\left[\left(1 - 0.3314\beta^{0.5}\right)\exp\left(-0.1Re_p\right) + 0.3314\beta^{0.5}\right] & Re_p \leq 40 \\ 6.46 \cdot 0.0524\sqrt{\beta Re_p} & Re_p > 40 \,, \end{cases} \tag{2.26}$$

where $\beta = 0.5\left(Re_\omega/Re_p\right)$.

Virtual mass force

Whenever particles decelerate or accelerate the virtual mass force is defined as the additional force required to accelerate a body immersed in a dense fluid compared to the same acceleration when the body is in a vacuum. This force makes the particles respond as if they had a greater mass than in actuality which also explains the naming of the force as an additional or virtual mass that has to be accelerated. The virtual mass force is given as

$$\boldsymbol{F}_{\mathrm{VM}} = -C_{\mathrm{VM}}\rho_{\mathrm{f}}\alpha_{\mathrm{p}}\left(\frac{D_{\mathrm{p}}}{Dt}\boldsymbol{u}_{\mathrm{p}} - \frac{D_{\mathrm{f}}}{Dt}\boldsymbol{u}_{\mathrm{f}}\right), \tag{2.27}$$

where C_{VM} is the virtual mass force coefficient and the terms D_{p}/Dt and D_{f}/Dt are the material derivatives for the particle and fluid phase, respectively. For a spherical particle in an incompressible and inviscid fluid, the virtual mass force coefficient is a constant of $C_{\mathrm{VM}} = 0.5$ (Drew et al., 1979).

The virtual mass force needs to be considered when simulating the behaviour of unsteady flows, as the force contribution is a function of the particle acceleration.

Turbulent dispersion force

When fluid flow within the domain is turbulent local velocity fluctuations occur, but as the turbulence is modelling using a RANS approach, these velocity fluctuations are not resolved. Therefore, the particles are only affected by the time-averaged fluid velocity and to include the force acting on the particles due to fluid velocity fluctuations, the turbulent dispersion force is included. Both Gosman et al. (1992) and Burns et al. (2004) performed Favre averaging of the drag force from the time-averaged fluid velocity and a separate diffusion turbulent drag term to achieve this. Burns et al. (2004) derived and proposed an explicit relationship for the turbulent dispersion force which is given by

$$\boldsymbol{F}_{\mathrm{disp}} = -\frac{3}{4}C_{\mathrm{D}}\frac{\alpha_{\mathrm{p}}\rho_{\mathrm{f}}}{d_{\mathrm{p}}}\boldsymbol{u}_{\mathrm{r}}\frac{\nu_{\mathrm{t}}}{\mathrm{Sc}_{\mathrm{t}}}\left(\frac{\nabla\alpha_{\mathrm{f}}}{\alpha_{\mathrm{f}}} - \frac{\nabla\alpha_{\mathrm{p}}}{\alpha_{\mathrm{p}}}\right), \tag{2.28}$$

where Sc_t is the turbulent Schmidt number for the volume fraction dispersion which is often assumed $Sc_t = 0.9$ (Frank et al., 2004; Rzehak and Krepper, 2013).

Another way to include this force directly is to choose another turbulence model. By resolving the fluid velocity fluctuations using e.g. direct numerical simulations (DNS) or large-eddy simulations (LES), the large-scale velocity fluctuations will be resolved and the drag force acting on these slip velocities would result in the turbulent dispersion force.

3 | Experimental Work

In order to validate the numerical results from the CFD-PBE model, experimental work was carried out at the Alfa Laval Test and Training Centre. The objective of the experimental work was to evaluate the separation efficiency of the high-speed separator under various conditions and to produce a particle size distribution of the particulates suspended in the water.

3.1 Alfa Laval Test and Training Centre

The Alfa Laval Test and Training Centre is a 2800 m^2 large testing area where all components onboard a ship can be tested. A 4-stroke MAN 28/32 engine with a nominal power of 2 MW is installed inside the centre. One of the main reasons the engine was installed in the centre was the ability to produce dirty exhaust gas to test exhaust gas treatment equipment. An overview of the Alfa Laval Test and Training Centre is seen in Fig. 3.1.

3.1.1 Components

The gas stream from the engine to the exhaust gas funnel is shown in Fig. 3.1 and the water recirculation loop inside the scrubber in Fig. 3.2. The gas stream consists of the following components.

Engine: MAN 28/32 engine with 9 cylinders capable of delivering 2 MW shaft power. The engine is connected to a generator delivering 1.8 MW of electrical power to the electrical grid of Aalborg at full power. The engine can operate on various fuels

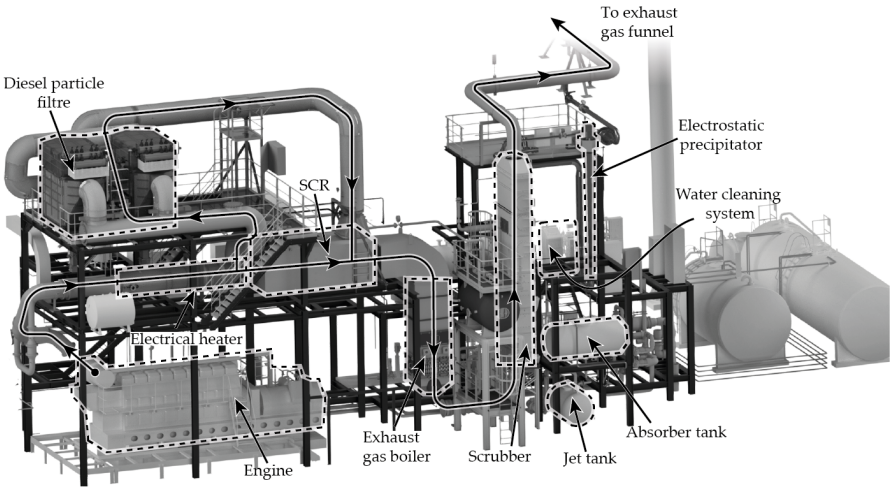

Fig. 3.1: Overview of the gas- and water streams in Alfa Laval's Test and Training Centre in Aalborg. The NO_x in the exhaust gas, produced by a 2 MW auxiliary engine, is removed in SCR, followed by a cooling sequence in the exhaust gas boiler. The exhaust gas enters the scrubber before reaching the exhaust gas funnel. The water inside the scrubber loop is recirculated over the jet- and absorber tank and cleaned using the high-speed separator with a flocculator pre-treatment.

including diesel oil (DO), marine gas oil (MGO), very low sulphur oil (VLSFO), heavy fuel oil (HFO) and even methanol, where the engine was operated on HFO during the test.

SCR: The selective catalytic reduction (SCR) unit removes NO_x in the exhaust gas. An electrical heater is placed upstream of the SCR to heat the exhaust gas if needed. The SCR unit is produced by Haldor Topsøe and works by spraying urea into the exhaust gas which reacts with the surface of the catalyst.

Diesel particle filter: Two boxes containing catalytic diesel particle filters (DPF) are installed in parallel with the SCR to remove PM and NO_x in the exhaust gas. Urea is injected into the DPF box to remove NO_x in a similar way as for the SCR. For the tests performed during the present work, the DPF was bypassed as 92-99 % of the PM would have been removed when passing through this unit (Johansen et al., 2022).

Exhaust gas boiler: An exhaust gas boiler is installed downstream

the SCR, where heat is extracted from the exhaust gas. The heat is used to produce steam operated at 7 bar and has a maximum capacity of 600 kg/h. Steam produced inside the boiler is transferred to the district heating grid of Aalborg.

Scrubber: An experimental in-line rectangular scrubber is installed after the exhaust gas boiler. Two spray systems are installed inside the scrubber, namely one sprayer system in the jet section and one above the absorber section. Above the absorber spray system, a demister is installed to capture the droplets inside the exhaust gas. The scrubber is operated in closed-loop mode where the water is recirculated over the jet- and absorber tank. The water used in the scrubber is extracted at two locations, one at the bottom of the jet section and one at the bottom of the absorber column. The water from the jet section is redirected to the jet tank and the water from the absorber section is redirected to the absorber tank.

Electrostatic precipitator: A small-scale wet electrostatic precipitator (WESP) is installed after the scrubber to remove PM. The WESP removes up to 97.2 % of the PM in the exhaust gas and can handle up to 12 % of the exhaust gas volume flow (Hansen et al., 2022). During operation, the PM is captured on the wet walls of the WESP and is flushed to the absorber tank with a fixed interval.

Absorber tank: Water from the absorber section is directed to the absorber tank, hence the naming. The absorber tank has a total volume of 3 m^3. During operation, water can be transported from the jet tank to the absorber tank due to droplet entrainment at high gas velocities, resulting in a high water level inside the tank. The water in the tank is then redirected to the jet tank. The acidity of the water increases during operation, which is why a pH meter is installed at the return pipe to the tank. The pH can be adjusted by dosing alkaline into the feed process stream leaving the absorber tank.

Jet tank: The jet tank has a total volume of 2 m^3 and receives

the dirtiest part of the water, as a large fraction of the particles is captured in the jet section of the scrubber. This is also why the water cleaning system is connected to this tank, where water is continuously cleaned using a high-speed separator. If a high water level is registered in the jet tank, water is redirected to a waste tank located outside of the centre.

Water cleaning system: The water cleaning system consists of a flocculator with chemical dosing and a high-speed separator (HSS). The flocculator is installed upstream of the high-speed separator and is designed with set a of consecutive straight pipes followed by 180° bends, as shown in Fig. 3.3. The pH can be adjusted at the inlet of the flocculator, where sodium hydroxide (NaOH) can be dosed. A coagulant is dosed when pH has been adjusted followed by a second dosing stage where a flocculant is dosed. Various chemicals can be dosed at these locations and at different rates. The HSS is an Alfa Laval NOPX-407 high-speed separator which is installed after the flocculator. The HSS can handle flow rates up to 6 m^3/h. The separated particle phase is discharged into a sludge tank which eventually is pumped to the waste tank outside the centre. The clean effluent water is returned to the jet tank.

3.1.2 Water Circulation Loop

As the present study focuses on the cleaning and pre-treatment of the scrubber washwater, a process overview of the scrubber water circulation loop is shown in Fig. 3.2. The water from the scrubber is split into two streams, namely the water coming from the jet section and the water coming from the absorber section. The water is circulated over the two tanks and the water going to the sprayers in the absorber column is cooled. Water droplets from the jet section can be entrained in the gas flow resulting in the absorber tank filling faster than the jet tank. Also, the majority of the condensation takes place in the absorber tank. To prevent high water levels, the water is bled to the jet tank where

the water cleaning system is also operated to remove PM. Before separation in the HSS, the PM is flocculated in the flocculator and the separated PM is stored as a sludge in a sludge tank.

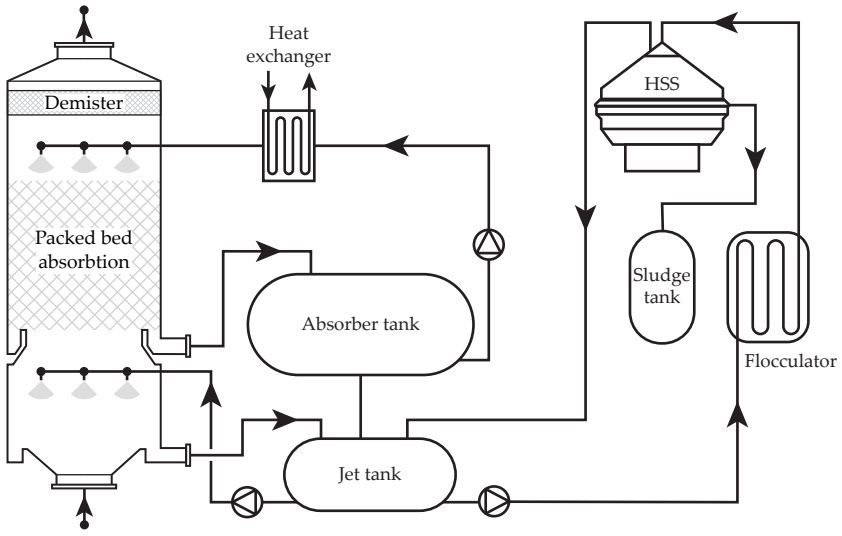

Fig. 3.2: Overview of the scrubber water recirculation loop. The washwater from the jet section of the scrubber is stored in the jet tank and the washwater from the absorber section is stored in the absorber tank. The water is cleaned from the jet tank using the flocculator and HSS and then redirected back to the jet tank.

3.2 Measurements

Particle size measurements were performed using a Malvern Mastersizer 3000 during a test in the Alfa Laval Test and Training Centre on 17/03-2021. The engine was operated on HFO and at a fixed load of 1,250 kW. As particles are transferred from the gas phase to the water phase inside the scrubber and WESP, the concentration of particles inside the jet tank increases. The water cleaning unit was operated with a volumetric flow rate in the range of 1-6 m^3/h. The objective of the test was to measure the particle size distribution of the soot, as this has not been previously performed, and to establish knowledge about the separation efficiency of the HSS. The size distribution is an important parameter for the design of the HSS. Hansen et al. (2022) performed particle size measure-

ments in the gas phase at the outlet of the scrubber on the same engine. It was determined that 97 % of the particulate mass is particles larger than d_p = 0.09 μm in the gas phase.

The Mastersizer 3000 by Malvern Panalytical capable of measuring particles between 0.01 μm and 3500 μm was used to measure the particles in the process water. The Mastersizer 3000 uses the technique of laser diffraction to measure the light scattering of suspended particles. The Mastersizer 3000 is equipped with two lasers with different wavelengths and sensors that capture the scattered light from the two different light sources and correlate the scattered light intensity to particle size.

Particles were destabilised using a chemical coagulant based on poly-aluminium chloride (Kemira PAX-HP800) followed by the addition of a polymer flocculant with a high interconnecting molecular structure and a high cationic charge (BASF Zetag 9048FS). As coagulants and flocculants have a preferred operating pH of 6-8, (Bratby, 2016) and as both the process water and the poly-aluminium chloride are acidic, sodium hydroxide is dosed to increase the pH before coagulation, which is shown in Fig. 3.3, reaching the desired pH of approximately 7.

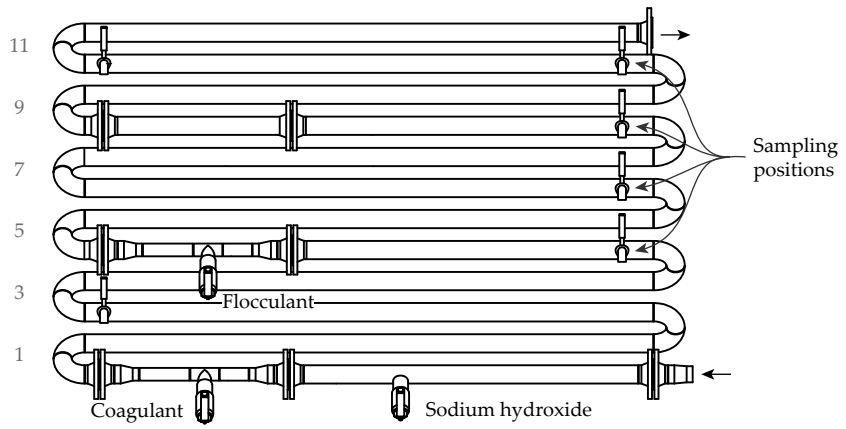

Fig. 3.3: Overview of the flocculator installed in the Alfa Laval Test and Training Centre. Sodium hydroxide (NaOH) is dosed at the inlet of the flocculator followed by a venturi-type mixer where the coagulant is dosed. After 4 consecutive bends, a flocculant is dosed in a venturi-like mixer. Sample points are located after 3, 4, 6, 8, 10 and 11 bends.

To induce turbulence while dosing both the coagulant and flocculant, a venturi-like mixer is introduced in the flocculator. Samples of the process water can be taken after a total of 3, 4, 6, 8, 10 and 11 bends to analyse the impact over the length of the flocculator. Additional flanges are installed between bends 8 and 10 as an optional dosing point for a third flocculant.

3.3 Results

As the objective of the test is to establish knowledge about the particle size distribution of soot suspended in water, the particle size distribution is measured at the inlet of the flocculator, where particles are stable and throughout the pipe flocculator after destabilisation. The stability of particles is also of interest, as it was established in the literature study, that suspended soot particles were moderately stable. Equipment to measure the zeta potential of the particles was not available at the test and the particle size distribution of a sample was instead measured to analyse whether it changes over time.

3.3.1 Feed Composition

The particle size distribution was measured at the inlet of the pipe flocculator. A set of samples were taken during the day to determine the size distribution of the untreated process water. The particle size distribution of the untreated particles is seen in Fig. 3.4. The spread of the measurements is generally small and the particle size distribution did not change significantly during testing. In general, it was found that 1 % of the volumetric density is smaller than $d_\mathrm{p} < 1$ μm and that 50 % of the particle mass is smaller than $d_\mathrm{p} < 8$ μm. Hansen et al. (2022) showed that 52 % of the particulate mass in the gas phase consists of particles smaller than $d_\mathrm{p} < 1$ μm, meaning that particles will aggregate to form slightly larger aggregates when suspended in water.

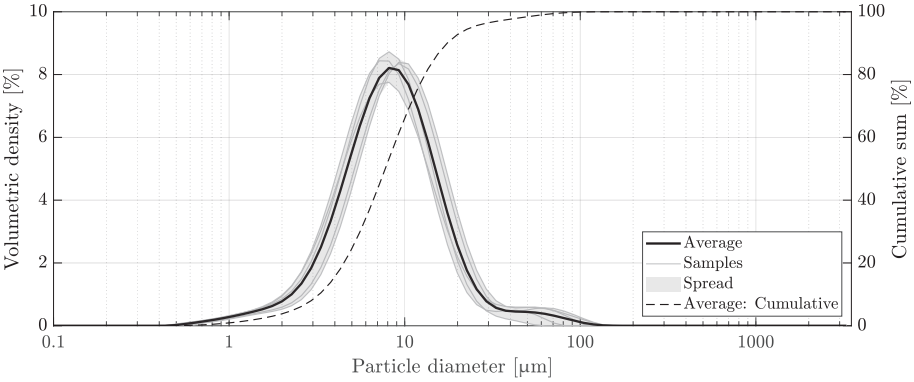

Fig. 3.4: Volumetric density function (left axis) and cumulative sum (right axis) of the untreated process water with soot particles.

3.3.2 Pipe Flocculator

The change in the particle size distribution is measured as the particles undergo flocculation in the pipe flocculator. Samples are taken at the inlet of the pipe flocculator, after 4x-, 6x-, 8x- and 10x bends which are marked in Fig. 3.3. The sample taken after 4x

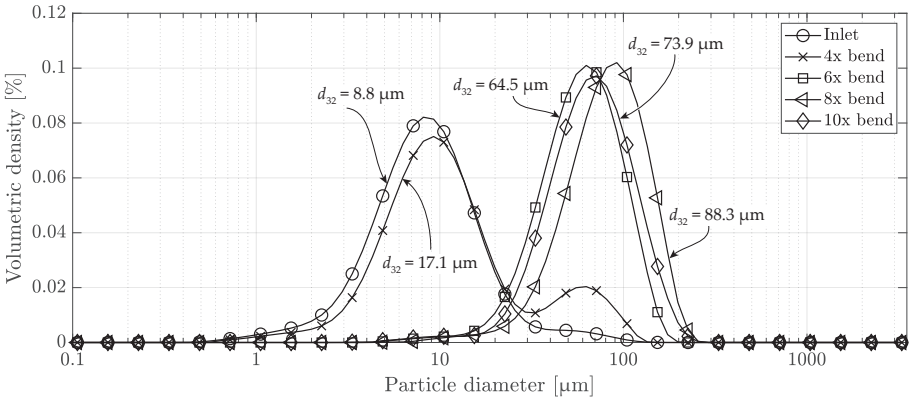

Fig. 3.5: Volumetric density function of the suspended particles in the process water throughout the pipe flocculator. See Fig. 3.3 for the position of sample locations.

bends has only been treated with the coagulant to destabilise the particles which causes some of the particles to aggregate. Polymer flocculant has been added into the process water after 6x bends, which explains the large difference between the previous sample. The averaged particle diameter increases until a total of 8 pipe

bends have been passed and then a slight decrease is observed. The decrease in size distribution is due to the breakage of the largest aggregation as additional turbulence is induced by the flanges installed between bend 8x and 10x as shown in Fig. 3.3.

3.3.3 Particle Stability

To analyse the stability of the suspended soot particles, a sample is analysed over time. The particle size distribution was measured when the sample was taken, after 23 hours and finally after 91 hours. Between the measurements, the sample was stored in a sealed laboratory glass bottle and placed in a motionless place to ensure no external movements of the sample. The measurements are shown in Fig. 3.6, where it is observed that there is a negligible difference between the initial sample and the sample measured after 91 hours. The suspended soot particles are therefore stable, meaning negligible aggregation happens over time if the sample is untreated, which is in good agreement with the zeta potential measurement by Liu et al. (2003), Growney et al. (2015) and Chen and Huang (2017).

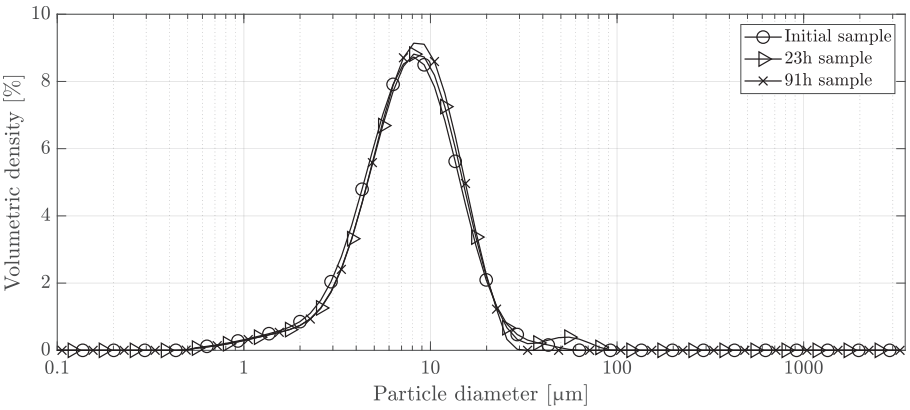

Fig. 3.6: Particle size distribution of an untreated process water sample with soot particles. The size distribution is measured when it was taken, after 23 hours of storage and again after 91 hours of storage.

4 | Contributions Related to Particle Aggregation and Breakage

The contributions and main findings related to particle aggregation and breakage are briefly outlined in this chapter. The papers in their entirety are found in Part II.

4.1 Paper A: On the agglomeration and breakage of particles in turbulent flows through pipe bends using CFD-PBE

The purpose of the study by Bilde et al. (2022), reprinted on page 97, is to develop a multiphase CFD model capable of describing the particle-laden flow using the Eulerian two-fluid model. The multiphase model includes the aggregation and breakage of solid particles in turbulent flows. The study analyses the impact of varying the Reynolds number and the bend radius of a pipe flocculator to clarify important design parameters. The geometrical configuration is two consecutive pipes, with a length of $L = 10d_\mathrm{h}$, connected by 180° pipe bends with a varying bend radius bounded by $1 \leq r_\mathrm{b} d_\mathrm{h} \leq 2.5$. A periodic boundary condition is applied to achieve an infinite long configuration. The applied Reynolds number of the fluid phase is bounded by $15,000 \leq \mathrm{Re}_\mathrm{f} \leq 35,000$ to analyse the impact of increasing turbulence on the particle size distribution.

4.1.1 Methodology

The population balance equation, described in Sec. 2.2 on page 32, is used to track the evolution of the particle number density function. The two-fluid Eulerian modelling approach, described in Sec. 2.3 on page 38 and interfacial momentum transfer includes the drag-, lift,- virtual mass- and turbulent dispersion force. Turbulence is modelled using the RNG k-ε model by Yakhot and Orszag (1986).

The particle phase is discretised with a logarithmic distribution between $d_\mathrm{p} = 1$ μm and $d_\mathrm{p} = 1000$ μm. The fluid velocity field is initialised using a single-phase steady-state solution and the dispersed particle phase is then inserted into the fully-developed fluid flow with a monodisperse size of $d_\mathrm{p} = 1$ μm.

4.1.2 Results

As the CFD-PBE model contains parameters that need fitting to the particle properties, a parameter sweep of these is performed and compared to the experimentally obtained particle size distributions reported in Sec. 3.3 on page 55. Fig. 4.1 shows the obtained particle size distribution when using a strength parameter of $B = 50 \cdot 10^{-7}$ m^3/s^3 and a binary daughter size distribution coefficient of $C_4 = 2$ for a fluid Reynolds number of $\mathrm{Re_f} = 22,500$. The coefficients used are able to reproduce the measured particle size distribution when aggregating soot particles suspended in water when adding a chemical coagulant and a polymer flocculant.

Analysing the effect of the increasing fluid Reynolds number on the particle size distribution shows that as the Reynolds number increases, the particle size distribution is skewed towards the smaller particles, as shown in Fig. 4.2. The simulations are performed for fluid Reynolds numbers in the range of $15,000 \leq \mathrm{Re_f} \leq 35,000$ for a bend radius of $r_\mathrm{b} = 1.5 d_\mathrm{h}$. As more turbulence is induced in the fluid domain, the turbulent energy dissipation rate increases, causing the largest particles to break, hence resulting in smaller particles.

At fluid Reynolds numbers of $\mathrm{Re_f} > 30,000$ there is not ob-

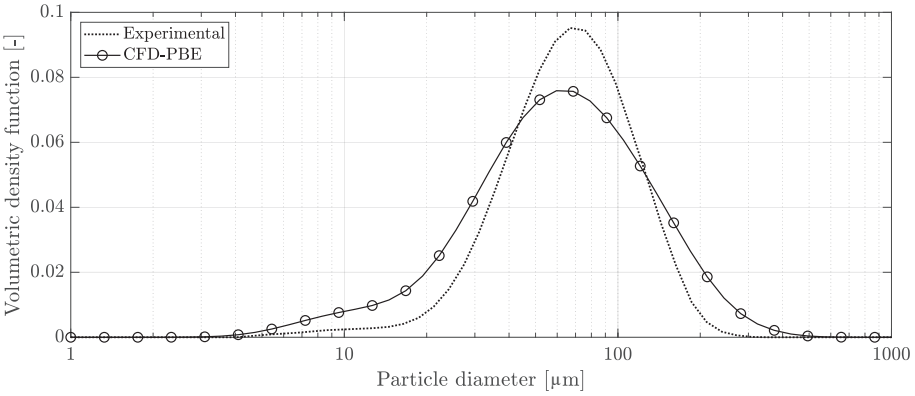

Fig. 4.1: Parametric fitting of the CFD-PBE model parameters using the experimentally obtained particle size distribution. The particle size distribution from the CFD-PBE model is obtained for a Reynolds number of $\mathrm{Re_f} = 22,500$ a particle strength coefficient of $B = 5 \cdot 10^{-7}$ $\mathrm{m^3/s^3}$ and a binary daughter size coefficient of $C_4 = 2$.

served a significant difference between the results from the different bend radii, as shown in Fig. 4.3. It is observed that the simulation with the largest bend radius produces the largest aggregates for fluid Reynolds numbers of $\mathrm{Re_f} < 30,000$. As a larger magnitude of turbulence is induced by decreasing the bend radius, the particles are more prone to breakage when choosing a small bend radius.

4.2 Paper B: Decay of secondary motion downstream bends in turbulent pipe flows

The purpose of the study of Bilde et al. (2023), reprinted on page 125, is to analyse the decay of secondary motion downstream of a pipe bend with different bend radii using LES. Understanding the induced turbulence structures and how the secondary flow decay downstream of a 180° bend is an important factor for a large range of engineering applications including those handling particle aggregation and breakage.

As the largest eddies are resolved when using LES only the smallest eddies are modelled using a sub-grid scale model and in the study, the WALE model of Nicoud and Ducros (1999) is applied. The LES model is validated using the experimental data

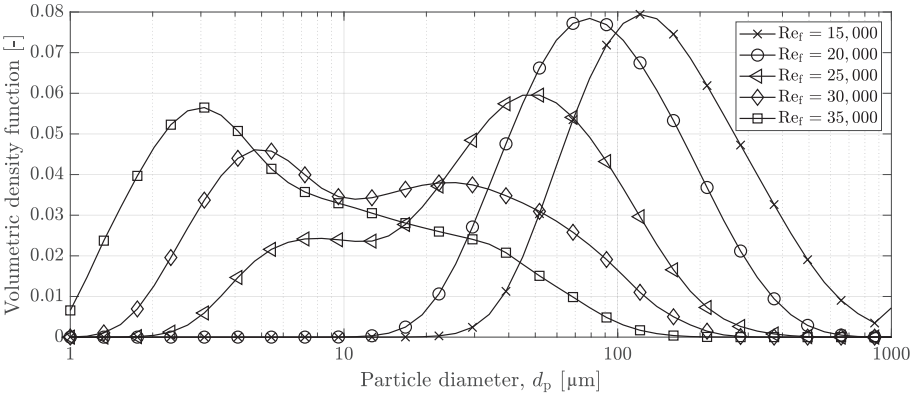

Fig. 4.2: Particle size distributions for fluid Reynolds numbers in the range of $15,000 \leq \mathrm{Re_f} \leq 35,000$ for a bend radius of $r_b = 1.5d_h$.

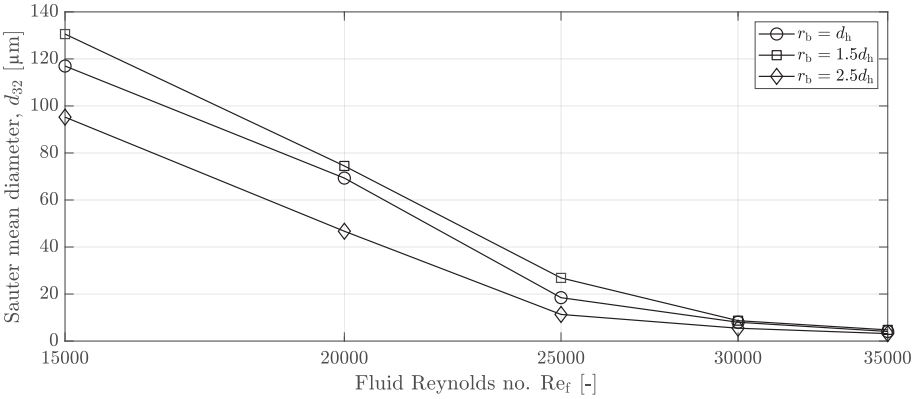

Fig. 4.3: Sauter mean diameter, d_{32}, as a function of the fluid Reynolds number for the three different bend radii.

of Toonder and Nieuwstadt (1997) for a straight pipe and the experimental data of Sattarzadeh (2011) and Kalpakli Vester et al. (2016) for a 90° pipe bend. A total of 5 simulations are carried out to simulate the decay of the secondary motion of pipe bends with a bend radius of $r_B = d_h$, $r_B = 1.5d_h$, $r_B = 2d_h$, $r_B = 2.5d_h$ and $r_B = 3.375d_h$.

4.2.1 Results

Analysing the turbulence intensity profile downstream from the pipe bend in Fig. 4.4 shows how the skewed profile is observable

immediately downstream from the bend. As the flow moves downstream the turbulence intensity profile recovers and becomes more uniform.

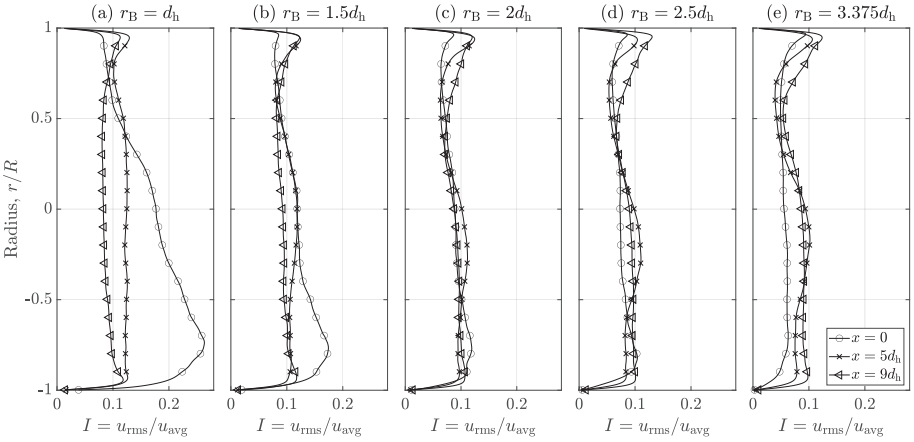

Fig. 4.4: Turbulence intensity profiles at the outlet of the bend, $x = 0$, at a downstream distance of $x = 5d_h$ and at the outlet of the computational domain, $x = 9d_h$, for the different bend radii. The inner pipe radius is defined by $r/R = -1$ and the outer is defined by $r/R = 1$.

The large magnitude of secondary motion induced by the pipe bend when the bend radius decreases decay quickly after the pipe bend, as shown in Fig. 4.5. A significant difference is observed between the secondary motion velocity profiles for the different bend radii, but after a downstream length of $x/d_h = 4$, there is an observed negligible difference between the configurations.

Analysing the area-averaged turbulence intensity downstream from the bend in Fig. 4.6, show the magnitude of turbulence induced by the pipe bend with different radii and how turbulence decay downstream from the bend. The length after the bend is limited to $x/d_h = 10$ and it is observed that an even longer straight pipe is needed downstream to obtain a turbulence intensity of the same magnitude as is observed at the inlet of the pipe.

It is concluded that the larger magnitudes of secondary motions decay with a larger gradient. Furthermore, it is shown how the secondary flow produces a skewed velocity profile and how the velocity profile recovers downstream of the bend. The recovery length of the velocity profile is shorter when more turbulence

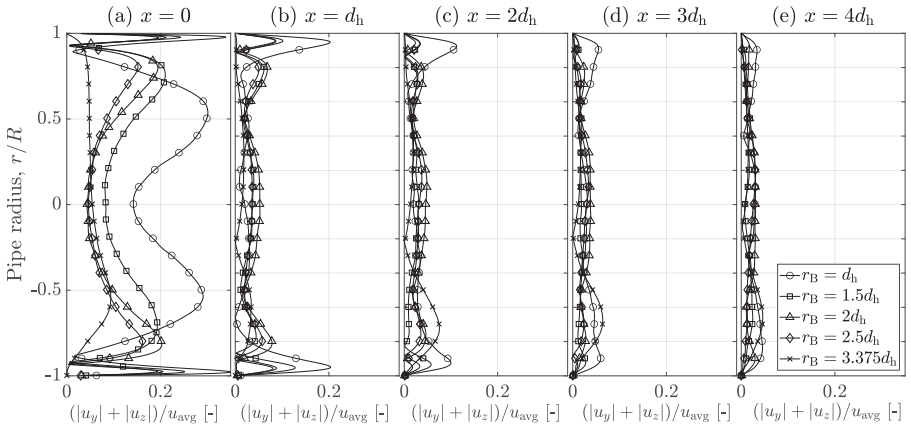

Fig. 4.5: Downstream normalised secondary velocity profile, $\left(|u_y| + |u_z|\right)/u_{\text{avg}}$, at $x/d_h = 0$, $x/d_h = 1$, $x/d_h = 2$, $x/d_h = 3$ and $x/d_h = 4$ after the pipe bend.

is induced within the pipe. This is in good agreement with the statement of Hellström et al. (2013) who states that the recovery of the velocity profile is driven by turbulence transport.

4.3 Paper C: On the design of compact hydraulic pipe flocculators using CFD-PBM

In the present study, reprinted on page 143, the important geometrical design parameters are investigated using the CFD-PBE modelling approach presented by Bilde et al. (2022). The geometrical parameters of interest are the pitch of inclination, φ, the bend radius, r_b, the primary length, L_1, and the secondary length, L_2, of the configuration, shown in Fig. 4.7. The pitch of inclination is varied between $1 \leq \varphi/d_h \leq 3$, the bend radius is varied between $1 \leq r_b/d_h \leq 2.5$, the primary length is varied between $0 \leq L_1/d_h \leq 20$ and the second length is varied between $0 \leq L_2/d_h \leq 10$. The special case where $L_1 = L_2 = 0$, thereby making a helically coiled tube flocculator, is also included in the simulations. A total of 123 simulations are carried out to evaluate the particle size distribution as a function of the geometrical configurations and clarify the most important parameters when designing a pipe flocculator. All simulations are carried out at

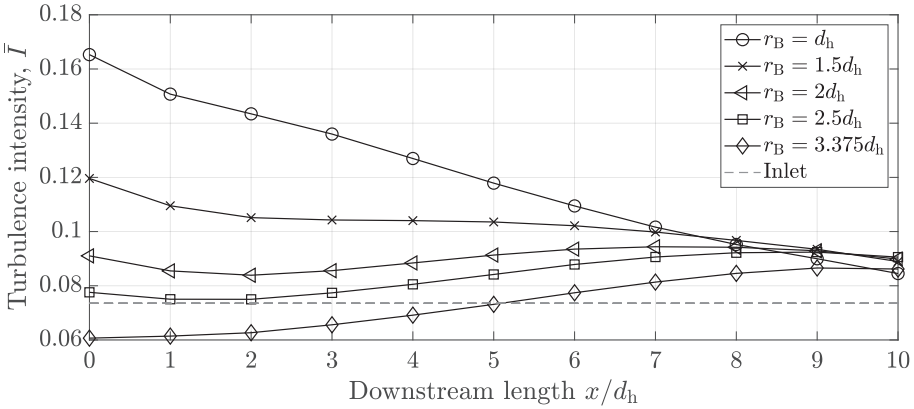

Fig. 4.6: Area-averaged turbulence intensity, $\bar{I}$, downstream from the bend.

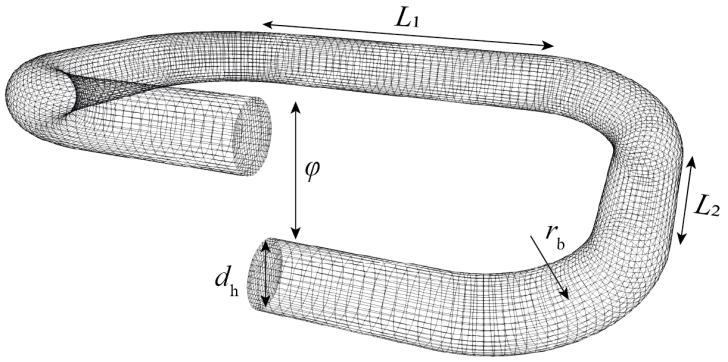

Fig. 4.7: Geometrical configuration and parameters that are analysed in the present study.

Reynolds numbers of $\mathrm{Re_f} = 20,000$.

4.3.1 Results

It was found that the pitch of inclination does not impact the particle size distribution significantly. This is also expected, as the density ratio between the fluid- and particle phases is low, $\rho_p/\rho_f = 1.4$. Analysing the cross-sectional averaged Sauter mean diameter, $\tilde{d}_{32}$, in Fig. 4.8 show how particles aggregate in the straight parts of the pipe and when a 90° bend is reached, breakage occurs resulting in a negative diameter gradient. Fig. 4.8 is shown for a single configuration to highlight the zones with a 90° bend, whereas Fig. C.4 in Paper C compares the cross-sectional

averaged Sauter mean diameter of 5 configurations.

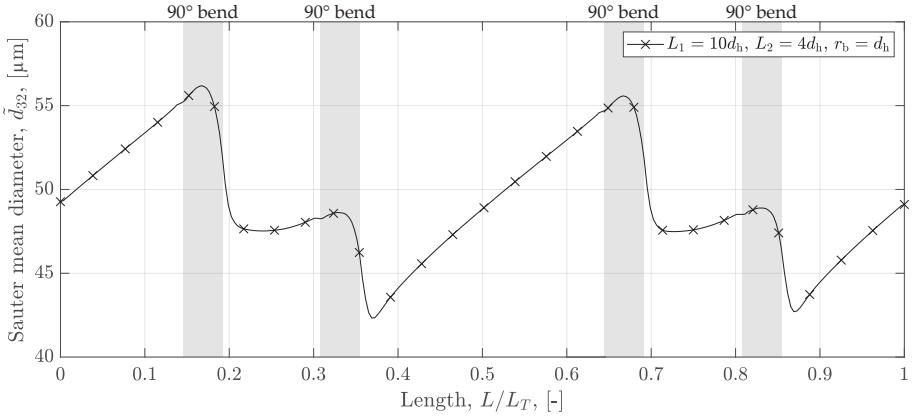

Fig. 4.8: Cross-sectional averaged Sauter mean diameter, $\tilde{d}_{32}$ for a configuration.

The volume-averaged Sauter mean diameter, seen in Fig. 4.9, show how larger aggregates are formed when the bend radius increases. It is observed that the particle diameter, $\overline{d}_{32}$, increases as the bend radius of the configuration increases. Furthermore, it is observed that the steady-state particle diameter is dependent on the primary- and secondary lengths. The particle diameter increases as the primary length of the configuration increases. An interesting observation is made for the helical pipe flocculators when the bend radius exceeds $r_b/d_h \geq 2$. In these two configurations, a significantly larger particle diameter is observed compared to the simulation with a similar configuration but $L_2/d_h = 2$. This indicates that if the bend radius is increased more, a large volume-averaged particle diameter will be observed for such a helical pipe flocculator. The largest particle diameter is observed for the configuration with $r_b/d_h = 2.5$, $L_1/d_h = 20$ and $L_2 = 0$.

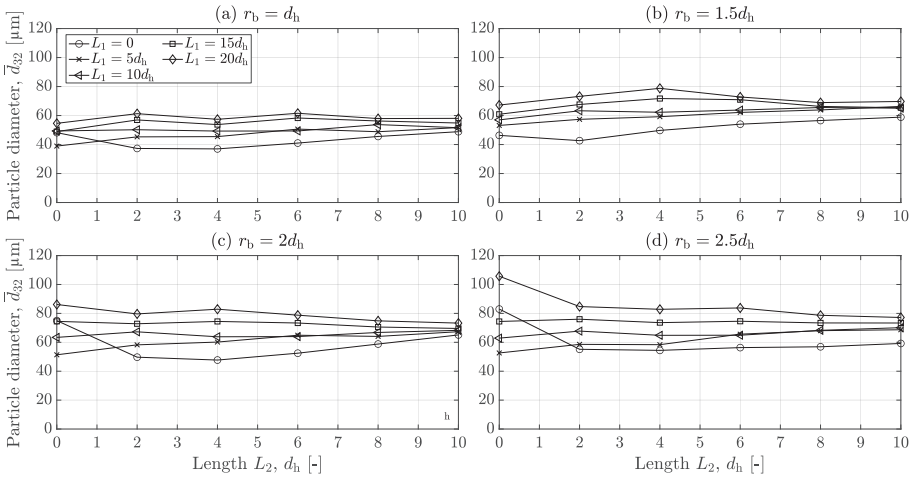

Fig. 4.9: Volume-averaged Sauter mean diameter, $\overline{d}_{32}$ for the different configurations.

5 | Closure

The main findings of this dissertation are summarised in the following section and an outlook with suggestions for future work is presented.

5.1 Conclusion

Aggregation and breakage of micron-sized particles is a commonly encountered problem in a large range of applications. Throughout the presented work, a fundamental understanding of governing particle transport when subject to a fluid flow and how particles aggregate and break when subject to turbulence is achieved. As billions of micron-sized particles at high Reynolds numbers are present in the presented industrial applications it is highlighted why the Eulerian-Eulerian approach is beneficial compared to the Eulerian-Lagrangian approach when modelling the fluid-particle flow using CFD. The number density function of the dispersed particle phase is tracked using the population balance equation which is solved using the class method. Two-way coupling of the CFD-PBE model is implemented into the open-source CFD library OpenFOAM, where appropriate interfacial force models are applied. Solid particle aggregation- and breakage kernels are developed to describe the changing particle size when subject to turbulence and these models are implemented into OpenFOAM.

To achieve a better understanding of the turbulence induced by a 180° bend and how this turbulence decay downstream of a bend, a large eddy simulation is carried out for five different

bend radii. Using the LES model, it is shown how secondary motion is induced by the curvature of the bend and that difference in secondary motion becomes negligible after a downstream length of $x/d_\mathrm{h} = 4$. The turbulence induced by the pipe bend is significantly larger when the bend radius is small, $r_\mathrm{B}/d_\mathrm{h} = 1$. It is shown how turbulence decay with a larger gradient when the initial turbulence is larger, which explains why the velocity profile recovers faster to its initial state.

Next, it is presented how to model the fluid-particle flow using the CFD-PBE framework and the modelling framework is fitted to predict the aggregation and breakage of soot particles. Simulating different bend radii of a pipe flocculator at different Reynolds numbers, show how aggregates change size depending on the geometrical setup and the turbulence induced by the pipe. Generally, it is concluded that larger bend radii produce larger aggregates but at the cost of a long distance to obtain a steady-state solution. When the Reynolds number increases sufficiently, $\mathrm{Re} > 30,000$, there is not observed any significant difference between the simulated bend radii.

Finally, guidelines on the design of pipe flocculators are presented after performing a total of 123 simulations. The geometrical parameters of a pipe flocculator are varied to conclude on the most important parameters and to find an optimum design within the bounded parameters when fixing the Reynolds number. It is, once again, concluded that the bend radius is the single most important parameter and that the primary length of a flocculator is the second-most important parameter. Furthermore, it is shown that the helically coiled pipe flocculator shows a promising result, however, the bend radius needs to be increased further than what was performed in this study.

To summarise: This dissertation has presented how multiphase CFD-PBE models can contribute to the design of applications where solid particle aggregation and breakage occur. Using the presented CFD-PBE model is possible to analyse in detail where aggregates are most prone to breakage and perform design alterations to find the most optimal configuration for the system at hand.

5.2 Outlook

Throughout this dissertation, the focus has been on fluid-particle flow and the modelling of the interfacial momentum transfer models. The momentum transfer models are based on the assumption that the particles are spherical and also that the aggregates are spherical. This is, of course, a crude assumption which can be refined using knowledge about the fractal dimension. One difficulty of applying this in the Eulerian-Eulerian framework is that the fractal dimension needs to be specified in advance and therefore requires knowledge of the morphology of the aggregates. One way of dealing with this could be to simulate smaller aggregates using an Eulerian-Lagrangian approach (e.g. CFD-DEM) and analyse the fractal dimension and morphology of the formed aggregates when the position of the fractal is considered as well.

The most important parameters in the study are related to the breakage kernel as this kernel defines the steady-state particle size distribution. The aggregate strength parameter, B, is tuned using experimental data, but in principle, this value could be coupled to existing adhesion theory, e.g. Johnson-Kendall-Roberts (JKR) or Derjaguin-Muller-Toporov (DMT). This would require more knowledge about the mechanical- and physical properties of the soot particles as well as the additives. This could prove to be a successful way of coupling the methods, expanding the breakage kernel to consider the mechanical properties of the particle phase instead of being a simple coefficient.

The turbulence properties of the fluid phase are in the multiphase model described using the RNG k-ε model and to achieve a higher prediction of the turbulence characteristics could be extended to LES. This would also enable a direct calculation of the turbulent dispersion force as the largest eddies are resolved using the method. The additional accuracy obtained when using LES comes at the expense of an even more computationally demanding model.

Another future work that is worth mentioning is the simulation of the flow through the separator and the turbulence properties

through this domain. The aggregates are created to withstand the turbulence inside the high-speed separator and therefore this device serves as the bottleneck of what the aggregates must be able to overcome. At the inlet, there is an interface between water and air which is most likely causing a lot of turbulence.

Bibliography

Y. Adachi, M. A. Cohen Stuart, and R. Fokkink. Kinetics of Turbulent Coagulation Studied by Means of End-over-End Rotation. *Journal of Colloid and Interface Science*, 165(2):310–317, 7 1994. ISSN 0021-9797. doi: 10.1006/JCIS.1994.1234.

M. Anwer, R. M.C. So, and Y. G. Lai. Perturbation by and recovery from bend curvature of a fully developed turbulent pipe flow. *Physics of Fluids A*, 1(8):1387–1397, 1989. ISSN 08998213. doi: 10.1063/1.857315.

J. Azzola, J. A.C. Humphrey, H. lacovides, and B. E. Launder. Developing turbulent flow in a u-bend of circular cross-section: Measurement and computation. *Journal of Fluids Engineering, Transactions of the ASME*, 108(2):214–221, 1986. ISSN 1528901X. doi: 10.1115/1.3242565.

Janarjan Bhandari, Swarup China, Kamal Kant Chandrakar, Greg Kinney, Will Cantrell, Raymond A. Shaw, Lynn R. Mazzoleni, Giulia Girotto, Noopur Sharma, Kyle Gorkowski, Stefania Gilardoni, Stefano Decesari, Maria Cristina Facchini, Nicola Zanca, Giulia Pavese, Francesco Esposito, Manvendra K. Dubey, Allison C. Aiken, Rajan K. Chakrabarty, Hans Moosmüller, Timothy B. Onasch, Rahul A. Zaveri, Barbara V. Scarnato, Paulo Fialho, and Claudio Mazzoleni. Extensive Soot Compaction by Cloud Processing from Laboratory and Field Observations. *Scientific Reports 2019 9:1*, 9(1):1–12, 8 2019. ISSN 2045-2322. doi: 10.1038/s41598-019-48143-y.

Kasper Gram Bilde, Jakob Hærvig, Ronald Lehnigk, Fabian

Schlegel, and Kim Sørensen. On the agglomeration and breakage of particles in turbulent flows through pipe bends using CFD-PBE. *Chemical Engineering Science*, 260:117915, 10 2022. ISSN 00092509. doi: 10.1016/J.CES.2022.117915.

Kasper Gram Bilde, Kim Sørensen, and Jakob Hærvig. Decay of secondary motion downstream bends in turbulent pipe flows. *Physics of Fluids*, 35(1):015102, 2023. doi: https://doi.org/10.1063/5.0129339.

John Bratby. *Coagulation and flocculation in water and wastewater treatment*. IWA Publishing, 2016. ISBN 9781843391067. doi: 10.2166/9781780407500.

J. Bridgeman, B. Jefferson, and S.A. A. Parsons. The development and application of CFD models for water treatment flocculators. *Advances in Engineering Software*, 41(1):99–109, 1 2010. ISSN 09659978. doi: 10.1016/J.ADVENGSOFT.2008.12.007.

John Bridgeman, Bruce Jefferson, and Simon Parsons. Assessing floc strength using CFD to improve organics removal. *Chemical Engineering Research and Design*, 86(8):941–950, 8 2008. ISSN 0263-8762. doi: 10.1016/J.CHERD.2008.02.007.

Jonathan M Bridgeman. *Investigating the relationship between shear and floc fate using CFD*. PhD thesis, Cranfield University, 2006.

A. D. Burns, Thomas Frank, Ian Hamill, and J. M. Shi. The Favre averaged drag model for turbulent dispersion in Eulerian multiphase flows. *5th International Conference on Multiphase Flow*, 4 (392):1–17, 2004.

Lingling Cai, Zhiqiang Liu, Sha Mi, Chun Luo, Kebo Ma, Aixiang Xu, and Sheng Yang. Investigation on flow characteristics of ice slurry in horizontal 90° elbow pipe by a CFD-PBM coupled model. *Advanced Powder Technology journal*, 30:2299–2310, 2019. doi: 10.1016/j.apt.2019.07.010.

Thomas R. Camp and Philip C. Stein. Velocity Gradients and Internal Work in Fluid Motion. *Journal of Boston Society of Civil Engineering*, 30:219–237, 1943.

David Leonard Chapman. A contribution to the theory of electrocapillarity. *The London, Edinburgh, and Dublin philosophical magazine and journal of science*, 25(148):475–481, 1913. ISSN 1941-5982. doi: 10.1080/14786440408634187.

Chengyu Chen and Weilin Huang. Aggregation Kinetics of Diesel Soot Nanoparticles in Wet Environments. *Environmental Science and Technology*, 51(4):2077–2086, 2 2017. ISSN 15205851. doi: 10.1021/acs.est.6b04575.

Clarkson. Clarkson World Fleet Register, 2022.

John C. Crittenden, R. Rhodes Trussell, David W. Hand, Kerry J. Howe, and George Tchobanoglous. *Water Treatment: Principles and Design*. Wiley, 3 edition, 2012.

P. A. Cundall and O. D. L. Strackt. Discrete numerical model for granular assemblies. *International Journal of Rock Mechanics and Mining Sciences & Geomechanics Abstracts*, 16(4):77, 8 1979. ISSN 01489062. doi: 10.1016/0148-9062(79)91211-7.

J David Griffith and Robert G Williams. Application of Jar-Test Analysis at Phoenix, Ariz. *Journal (American Water Works Association)*, 64(12):825–830, 1972.

W.R. Dean. The stream-line motion of fluid in a curved pipe. *The London, Edinburgh, and Dublin Philosophical Magazine and Journal of Science*, 5(30):673–695, 4 1928. ISSN 1941-5982. doi: 10.1080/14786440408564513.

Massimiliano Di Liberto, Ivan Di Piazza, and Michele Ciofalo. Turbulence structure and budgets in curved pipes. *Computers and Fluids*, 88:452–472, 12 2013. ISSN 00457930. doi: 10.1016/j.compfluid.2013.09.028.

Farzad F. Dizaji, Jeffrey S. Marshall, and John R. Grant. Collision and breakup of fractal particle agglomerates in a shear flow. *Journal of Fluid Mechanics*, 862:592–623, 3 2019. ISSN 14697645. doi: 10.1017/jfm.2018.959.

D. Drew, L. Cheng, and R. T. Lahey. The analysis of virtual mass effects in two-phase flow. *International Journal of Multiphase Flow*, 5(4):233–242, 8 1979. ISSN 0301-9322. doi: 10.1016/0301-9322(79)90023-5.

Joel J Ducoste and Mark M Clark. Turbulence in flocculators: Comparison of measurements and CFD simulations. *AIChE Journal*, 45(2):432–436, 1999. doi: 10.1002/aic.690450222.

EGCSA. SOx Regulation Map, 2022.

Andrew Escue and Jie Cui. Comparison of turbulence models in simulating swirling pipe flows. *Applied Mathematical Modelling*, 34(10):2840–2849, 10 2010. ISSN 0307-904X. doi: 10.1016/J.APM.2009.12.018.

Meng Fan, Liangfu Chen, Shenshen Li, Mingmin Zou, Lin Su, and Jinhua Tao. The Effects of Morphology and Water Coating on the Optical Properties of Soot Aggregates. *Aerosol and Air Quality Research*, 16:1315–1326, 2016. ISSN 2071-1409. doi: 10.4209/aaqr.2015.04.0250.

Thomas Frank, Junmei Shi, and A. D. Burns. Validation of eulerian multiphase flow models for nuclear safety applications. In *3rd International Symposium on Two-Phase Flow Modelling and Experimentation*, 2004. doi: 10.1364/OE.26.001825.

Sashikumaar Ganesan. An operator-splitting Galerkin/SUPG finite element method for population balance equations : stability and convergence. *ESAIM: Mathematical Modelling and Numerical Analysis*, 46(6):1447–1465, 11 2012. ISSN 0764-583X. doi: 10.1051/M2AN/2012012.

Mohamed Gar Alalm, Mahmoud Nasr, and Shinichi Ookawara. Assessment of a novel spiral hydraulic flocculation/sedimentation system by CFD simulation, fuzzy inference system, and response surface methodology. *Separation and Purification Technology*, 169:137–150, 9 2016. ISSN 1383-5866. doi: 10.1016/J.SEPPUR.2016.06.019.

Massimo Germano, Ugo Piomelli, Parviz Moin, and William H. Cabot. A dynamic subgrid-scale eddy viscosity model. *Physics of Fluids A: Fluid Dynamics*, 3(7):1760, 6 1998. ISSN 0899-8213. doi: 10.1063/1.857955.

A. D. Gosman, C. Lekakou, S. Politis, R. I. Issa, and M. K. Looney. Multidimensional modeling of turbulent two-phase flows in stirred vessels. *AIChE Journal*, 38(12):1946–1956, 12 1992. ISSN 1547-5905. doi: 10.1002/AIC.690381210.

Erik Gotfredsen, Jens Dahl Kunoy, Stefan Mayer, and Knud Erik Meyer. Experimental validation of RANS and DES modelling of pipe flow mixing. *Heat and Mass Transfer/Waerme- und Stoffuebertragung*, pages 2211–2224, 2020. ISSN 14321181. doi: 10.1007/s00231-020-02835-8.

M. Gouy. Sur la constitution de la charge électrique à la surface d'un électrolyte. *Journal de Physique Théorique et Appliquée*, 9 (1):457–468, 1910. ISSN 0368-3893. doi: 10.1051/JPHYSTAP: 019100090045700.

David J. Growney, Oleksandr O. Mykhaylyk, Laurence Middlemiss, Lee A. Fielding, Matthew J. Derry, Najib Aragrag, Gordon D. Lamb, and Steven P. Armes. Is Carbon Black a Suitable Model Colloidal Substrate for Diesel Soot? *Langmuir*, 31(38): 10358–10369, 2015. ISSN 15205827. doi: 10.1021/acs.langmuir.5b02017.

Johannes Haarhoff and Jeremia J van der Walt. Towards optimal design parameters for around-the-end hydraulic flocculators. *Journal of Water Supply: Research and Technology-Aqua*, 50(3):149–160, 5 2001. ISSN 0003-7214. doi: 10.2166/aqua.2001.0014.

J. Hærvig, K. Sørensen, and T.J. J. Condra. Early stages of agglomeration of adhesive particles in fully-developed turbulent pipe flows. *International Journal of Multiphase Flow*, 106:254–267, 9 2018. ISSN 0301-9322. doi: 10.1016/J.IJMULTIPHASEFLOW.2018.04.017.

Jakob Hærvig. *On the Adhesive Behaviour of Micron-sized Particles in Turbulent Flow: A Numerical Study Coupling the Discrete Element Method and Large Eddy Simulations*. PhD thesis, Aalborg University, 2017.

Jens Peter Hansen. Exhaust Gas Scrubber Installed Onboard MV Ficaria Seaways Title: Exhaust Gas Scrubber Installed Onboard MV Ficaria Seaways. Technical Report 1429, Miljøstyrelsen, 2012.

Nick Høy Hansen, Henrik Sørensen, and Jakob Haervig. Experimental study of a full-scale hexagonal wet electrostatic precipitator for collection of black carbon and particulate matter generated by a marine diesel engine. *https://doi.org/10.1080/10962247.2022.2121325*, 9 2022. ISSN 1096-2247. doi: 10.1080/10962247.2022.2121325.

Leo H.O. Hellström, Metodi B. Zlatinov, Guangjun Cao, and Alexander J. Smits. Turbulent pipe flow downstream of a 90° bend. *Journal of Fluid Mechanics*, 735:R7, 2013. ISSN 14697645. doi: 10.1017/jfm.2013.534.

Heinrich Hertz. Ueber die Berührung fester elastischer Körper. *Journal fur die Reine und Angewandte Mathematik*, 1882(92):156–171, 1 1882. ISSN 14355345. doi: 10.1515/CRLL.1882.92.156/MACHINEREADABLECITATION/RIS.

A. Hilgenstock and R. Ernst. Analysis of installation effects by means of computational fluid dynamics—CFD vs experiments? *Flow Measurement and Instrumentation*, 7(3-4):161–171, 9 1996. ISSN 0955-5986. doi: 10.1016/S0955-5986(97)88066-1.

Christine M. Hrenya and Jennifer L. Sinclair. Effects of particle-phase turbulence in gas-solid flows. *AIChE Journal*, 43(4):853–869, 4 1997. ISSN 1547-5905. doi: 10.1002/AIC.690430402.

H. M. Hulburt and S. Katz. Some problems in particle technology: A statistical mechanical formulation. *Chemical Engineering Science*, 19(8):555–574, 8 1964. ISSN 0009-2509. doi: 10.1016/0009-2509(64)85047-8.

IMO. Prevention of Air Pollution from Ships, 2020.

International Maritime Organisation. Emission Control Areas (ECAs) designated under regulation 13 of MARPOL Annex VI (NOx emission control), 2019.

R. I. Issa. Solution of the implicitly discretised fluid flow equations by operator-splitting. *Journal of Computational Physics*, 62(1):40–65, 1 1986. ISSN 10902716. doi: 10.1016/0021-9991(86)90099-9.

Ricardo I Jeldres, Phillip D Fawell, and Brendan J Florio. Population balance modelling to describe the particle aggregation process: A review. *Powder Technology*, 326:190–207, 2017. doi: 10.1016/j.powtec.2017.12.033.

Zhaohua Jiang, Kenta Rai, Takuya Tsuji, Kimiaki Washino, Toshitsugu Tanaka, and Jun Oshitani. Upscaled DEM-CFD model for vibrated fluidized bed based on particle-scale similarities. *Advanced Powder Technology*, 31(12):4598–4618, 12 2020. ISSN 15685527. doi: 10.1016/j.apt.2020.10.009.

Keld Johansen, Peter Bergstrøm Kristensen, Ruddi Mortensen, Anders Schou Simonsen, John Phair, Søren Mølgaaard, and Jens Peter Hansen. *Development of Catalytic Filter for marine engines*. The Danish Environmental Protection Agency, 2022. ISBN 9788770384162.

K. L. Johnson, K. Kendall, and A. D. Roberts. Surface energy and the contact of elastic solids. *Proceedings of the Royal Society of London Series A*, 324:301–313, 1971. doi: 10.1098/rspa.1971.0141.

P. C. Johnson and R. Jackson. Frictional–collisional constitutive relations for granular materials, with application to plane shearing. *Journal of Fluid Mechanics*, 176:67–93, 1987. ISSN 1469-7645. doi: 10.1017/S0022112087000570.

A. Kalpakli and R. Örlü. Turbulent pipe flow downstream a 90° pipe bend with and without superimposed swirl. *International Journal of Heat and Fluid Flow*, 41:103–111, 6 2013. ISSN 0142727X. doi: 10.1016/j.ijheatfluidflow.2013.01.003.

Athanasia Kalpakli Vester, Sohrab S. Sattarzadeh, and Ramis Örlü. Combined hot-wire and PIV measurements of a swirling turbulent flow at the exit of a 90° pipe bend. *Journal of Visualization*, 19(2):261–273, 2016. ISSN 18758975. doi: 10.1007/s12650-015-0310-1.

Jongtae Kim, Mohan Yadav, and Seungjin Kim. Characteristics of Secondary Flow Induced by 90-Degree Elbow in Turbulent Pipe Flow. *Engineering Applications of Computational Fluid Mechanics*, 8(2):229–239, 2014. ISSN 1994-2060. doi: 10.1080/19942060.2014.11015509.

Won Wook Kim and Suresh Menon. A new dynamic one-equation subgrid-scale model for large eddy simulations. *33rd Aerospace Sciences Meeting and Exhibit*, 1995. doi: 10.2514/6.1995-356.

Jesper Kjølholt, Stian Aakre, Carsten Jürgensen, and Jørn Lauridsen. *Assessment of possible impacts of scrubber water discharges on the marine environment*. Miljøstyrelsen, 2012. ISBN 978-87-92903-30-3.

Andrey Nikolaevich Kolmogorov. Dissipation of energy in the locally isotropic turbulence. *Dokl. Akad. Nauk SSSR A*, 32:16,18, 1941a.

Andrey Nikolaevich Kolmogorov. The local structure of turbulence in incompressible viscous fluid for very large Reynolds numbers. *Cr Acad. Sci. URSS*, 30:301–305, 1941b.

Ajeet Kumar and Chandra Kumar Dixit. 3 - Methods for characterization of nanoparticles. In Surendra Nimesh, Ramesh Chandra, and Nidhi B T Advances in Nanomedicine for the Delivery of Therapeutic Nucleic Acids Gupta, editors, *Advances in Nanomedicine for the Delivery of Therapeutic Nucleic Acids*, pages 43–58. Woodhead Publishing, 2017. ISBN 978-0-08-100557-6. doi: https://doi.org/10.1016/B978-0-08-100557-6.00003-1.

Sanjeev Kumar and D. Ramkrishna. On the solution of population balance equations by discretization—I. A fixed pivot technique. *Chemical Engineering Science*, 51(8):1311–1332, 4 1996. ISSN 0009-2509. doi: 10.1016/0009-2509(96)88489-2.

K. A. Kusters. *The influence of turbulence on aggregation of small particles in agitated vessels*. PhD thesis, Technische Universiteit Eindhoven, 1991.

Marko Laakkonen, Pasi Moilanen, Ville Alopaeus, and Juhani Aittamaa. Modelling local bubble size distributions in agitated vessels. *Chemical Engineering Science*, 62(3):721–740, 2 2007. ISSN 0009-2509. doi: 10.1016/J.CES.2006.10.006.

S Laine, L Phan, P Pellarin, and P Robert. Operating Diagnostics On A Flocculator-settling Tank Using Fluent CFD Software. *WIT Transactions on Ecology and the Environment*, 33, 1999. doi: https://doi.org/10.2495/WP990251.

Beate Lange, Till Markus, Lutz Philipp Helfst, and Dr Michaela Mayer. Impacts of Scrubbers on the environmental situation in ports and coastal waters. Technical report, Umweltbundesamt, 6 2015.

Philipp Lau and Matthias Kind. CFD-PBE simulation to predict particle growth in a fluidized bed melt granulation batch process. *Powder Technology*, 300:28–36, 10 2016. ISSN 1873328X. doi: 10.1016/J.POWTEC.2016.02.040.

B. E. Launder and D. B. Spalding. The numerical computation of turbulent flows. *Computer Methods in Applied Mechanics and Engineering*, 3(2):269–289, 3 1974. ISSN 0045-7825. doi: 10.1016/0045-7825(74)90029-2.

B. E. Launder, G. J. Reece, and W. Rodi. Progress in the development of a Reynolds-stress turbulence closure. *Journal of Fluid Mechanics*, 68(3):537–566, 1975. ISSN 1469-7645. doi: 10.1017/S0022112075001814.

Chai Siah Lee, John Robinson, and Mei Fong Chong. A review on application of flocculants in wastewater treatment. *Process Safety and Environmental Protection*, 92(6):489–508, 11 2014. ISSN 0957-5820. doi: 10.1016/J.PSEP.2014.04.010.

R. Lehnigk, W. Bainbridge, Y. Liao, D. Lucas, T. Niemi, J. Peltola, and F. Schlegel. An open-source population balance modeling

framework for the simulation of polydisperse multiphase flows. *AIChE Journal*, page e17539, 12 2021. ISSN 1547-5905. doi: 10.1002/AIC.17539.

Ronald Lehnigk. *A generalized population balance model for the simulation of polydisperse multiphase flows within the Euler-Euler framework*. PhD thesis, Technischen Universität Dresden, 2020.

Dongyue Li, Zhengming Gao, Antonio Buffo, Wioletta Podgorska, and Daniele L. Marchisio. Droplet breakage and coalescence in liquid–liquid dispersions: Comparison of different kernels with EQMOM and QMOM. *AIChE Journal*, 63(6):2293–2311, 6 2017. ISSN 1547-5905. doi: 10.1002/AIC.15557.

Y. Liao, R. Oertel, S. Kriebitzsch, F. Schlegel, and D. Lucas. A discrete population balance equation for binary breakage. *International Journal for Numerical Methods in Fluids*, 87(4):202–215, 6 2018. ISSN 1097-0363. doi: 10.1002/FLD.4491.

Congmin Liu, Shuzo Nemoto, and Satoshi Ogano. Effect of soot properties in diesel engine oils on frictional characteristics. *Tribology Transactions*, 46(1):12–18, 2003. ISSN 1547397X. doi: 10.1080/10402000308982593.

J. Liu, M. Crapper, and G.L. McConnachie. An accurate approach to the design of channel hydraulic flocculators. *Water Research*, 38(4):875–886, 2 2004. ISSN 0043-1354. doi: 10.1016/J.WATRES.2003.10.014.

C. K. K. Lun and S. B. Savage. The effects of an impact velocity dependent coefficient of restitution on stresses developed by sheared granular materials. *Acta Mechanica 1986 63:1*, 63(1):15–44, 11 1986. ISSN 1619-6937. doi: 10.1007/BF01182538.

C. K. K. Lun, S. B. Savage, D. J. Jeffrey, and N. Chepurniy. Kinetic theories for granular flow: inelastic particles in Couette flow and slightly inelastic particles in a general flowfield. *Journal of Fluid Mechanics*, 140:223–256, 1984. ISSN 1469-7645. doi: 10.1017/S0022112084000586.

Changgen Luo. *Distribution of velocities and velocity gradients in mixing and flocculation vessels: comparison between LDV data and CFD predictions*. PhD thesis, Net Jersey institute of Technology, 1997.

Xiaofei Ma, Christopher D Zangmeister, Julien Gigault, George W Mulholland, and Michael R Zachariah. Soot aggregate restructuring during water processing. *Journal of Aerosol Science*, 66: 209–219, 2013. doi: 10.1016/j.jaerosci.2013.08.001.

E. Madadi-Kandjani and A. Passalacqua. An extended quadrature-based moment method with log-normal kernel density functions. *Chemical Engineering Science*, 131:323–339, 7 2015. ISSN 00092509. doi: 10.1016/j.ces.2015.04.005.

Kerstin Magnusson, Peter Thor, and Maria Granberg. Scrubbers: Closing the loop Activity 3: Task 2 Risk Assessment of marine exhaust gas scrubber water. Technical report, IVL Swedish Environmental Research Institute, 2018.

Malvern Panalytical. Mastersizer 3000.

Benoit B Mandelbrot. Self-Affine Fractals and Fractal Dimension. *Physica Scripta*, 32(4):257, 10 1985. ISSN 1402-4896. doi: 10.1088/0031-8949/32/4/001.

Daniele L. Marchisio and Rodney O. Fox. Solution of population balance equations using the direct quadrature method of moments. *Journal of Aerosol Science*, 36(1):43–73, 1 2005. ISSN 0021-8502. doi: 10.1016/J.JAEROSCI.2004.07.009.

Daniele L. Marchisio, R. Dennis Vigil, and Rodney O. Fox. Implementation of the quadrature method of moments in CFD codes for aggregation - breakage problems. *Chemical Engineering Science*, 58(15):3337–3351, 8 2003. ISSN 00092509. doi: 10.1016/S0009-2509(03)00211-2.

Elizabeth Marden Marshall and André Bakker. Computational Fluid Mixing. *Handbook of industrial mixing: science and practice*, pages 257–343, 2004.

Robert McGraw. Description of Aerosol Dynamics by the Quadrature Method of Moments. *http://dx.doi.org/10.1080/02786829708965471*, 27(2):255–265, 1 1997. ISSN 15217388. doi: 10.1080/02786829708965471.

R. Mei. An approximate expression for the shear lift force on a spherical particle at finite reynolds number. *International Journal of Multiphase Flow*, 18(1):145–147, 1 1992. ISSN 0301-9322. doi: 10.1016/0301-9322(92)90012-6.

MEPC. Resolution MEPC.340(77): 2021 Guidelines for Exhaust Gas Cleaning Systems. Technical report, Marine Environment Protection Committee, 2021.

V. A. Mhaisalkar, R. Paramasivam, and A. G. Bhole. Optimizing physical parameters of rapid mix design for coagulation-flocculation of turbid waters. *Water Research*, 25(1):43–52, 1 1991. ISSN 0043-1354. doi: 10.1016/0043-1354(91)90097-A.

E. F. Mikhailov, S. S. Vlasenko, Igor A. Podgorny, V. Ramanathan, and C. E. Corrigan. Optical properties of soot–water drop agglomerates: An experimental study. *Journal of Geophysical Research: Atmospheres*, 111(D7):7209, 4 2006. ISSN 2156-2202. doi: 10.1029/2005JD006389.

Jun Nan, Meng Yao, Ting Chen, Zhenbei Wang, Qinggui Li, and Dan Zhan. Experimental and numerical characterization of floc morphology: role of changing hydraulic retention time under flocculation mechanisms. *Environmental Science and Pollution Research*, 23(4):3596–3608, 2 2016. ISSN 0944-1344. doi: 10.1007/s11356-015-5539-7.

F Nicoud and F Ducros. Subgrid-Scale Stress Modelling Based on the Square of the Velocity Gradient Tensor. *Flow, Turbulence and Combustion*, 62:183–200, 1999.

D. S. Oliveira and E. C. Teixeira. Swirl number in helically coiled tube flocculators: theoretical, experimental, and CFD modeling analysis. *International Journal of Environmental Science and Technology*, 16(3):3735–3744, 2018. doi: 10.1007/s13762-018-2027-x.

D. S. Oliveira, E. C. Teixeira, and C. B. Donadel. Novel approaches for predicting efficiency in helically coiled tube flocculators using regression models and artificial neural networks. *Water and Environment Journal*, 34(4):550–562, 11 2020. ISSN 1747-6593. doi: 10.1111/WEJ.12484.

Danieli Soares de Oliveira and Clainer Bravin Donadel. Global velocity gradient evaluation: An innovative approach using CFD modeling applied to water and wastewater treatment plants. *Journal of Water Process Engineering*, 28:21–27, 4 2019. ISSN 2214-7144. doi: 10.1016/J.JWPE.2018.12.009.

St Palzer. Agglomeration of pharmaceutical, detergent, chemical and food powders — Similarities and differences of materials and processes. *Powder Technology*, 206(1-2):2–17, 1 2011. ISSN 0032-5910. doi: 10.1016/J.POWTEC.2010.05.006.

A. Passalacqua, F. Laurent, E. Madadi-Kandjani, J. C. Heylmun, and R. O. Fox. An open-source quadrature-based population balance solver for OpenFOAM. *Chemical Engineering Science*, 176:306–318, 2 2018. ISSN 0009-2509. doi: 10.1016/J.CES.2017.10.043.

C. P. Priesing. A theory of coagulation useful for design. *Industrial and Engineering Chemistry*, 54(8):38–45, 8 1962. ISSN 00197866. doi: 10.1021/IE50632A006/ASSET/IE50632A006.FP.PNG{_}V03.

Liu-Chao Qiu, Jia-Jie Liu, Yi Liu, Peng-Zhi Lin, and Yu Han. CFD-DEM Simulation of Flocculation and Sedimentation of Cohesive Fine Particles. In *Proceedings of the 7th International Conference on Discrete Element Methods*, pages 537–542, 2016. ISBN 10.1007/9789811. doi: 10.1007/978-981-10-1926-5{_}55.

Osbourne Reynolds. IV. On the dynamical theory of incompressible viscous fluids and the determination of the criterion. *Philosophical Transactions of the Royal Society of London. (A.)*, 186:123–164, 12 1895. ISSN 0264-3820. doi: 10.1098/RSTA.1895.0004.

Stephen K. Robinson. Coherent motions in the turbulent boundary layer. *Annual Review of Fluid Mechanics*, 23(1):601–639, 11 1991. ISSN 00664189. doi: 10.1146/annurev.fl.23.010191.003125.

Gerta Rocklage-Marliani, Maren Schmidts, and Venkatesa I. Vasanta Ram. Three-Dimensional Laser-Doppler Velocimeter Measurements in Swirling Turbulent Pipe Flow. *Flow, Turbulence and Combustion 2003 70:1*, 70(1):43–67, 2003. ISSN 1573-1987. doi: 10.1023/B:APPL.0000004913.82057.81.

R. Röhrig, S. Jakirlić, and C. Tropea. Comparative computational study of turbulent flow in a 90° pipe elbow. *International Journal of Heat and Fluid Flow*, 55:120–131, 10 2015. ISSN 0142727X. doi: 10.1016/j.ijheatfluidflow.2015.07.011.

M. Rowe. Measurements and computations of flow in pipe bends. *Journal of Fluid Mechanics*, 43(4):771–783, 10 1970. ISSN 14697645. doi: 10.1017/S0022112070002732.

Roland Rzehak and Eckhard Krepper. CFD modeling of bubble-induced turbulence. *International Journal of Multiphase Flow*, 55:138–155, 10 2013. ISSN 0301-9322. doi: 10.1016/J.IJMULTIPHASEFLOW.2013.04.007.

P. Saffman. The lift on a small sphere in a slow shear flow. *Journal of Fluid Mechanics1*, 22(2):385–400, 1965. doi: 10.1017/S0022112065000824.

P. G. Saffman and J. S. Turner. On the collision of drops in turbulent clouds. *Journal of Fluid Mechanics*, 1(1):16–30, 1956. ISSN 1469-7645. doi: 10.1017/S0022112056000020.

F. Salehi, M. J. Cleary, and A. R. Masri. Population balance equation for turbulent polydispersed inertial droplets and particles. *Journal of Fluid Mechanics*, 831:719–742, 11 2017.

F. Salehi, M. J. Cleary, A. R. Masri, and A. Kronenburg. Large eddy simulation of polydispersed inertial particles using two-way coupled PDF-PBE. *International Journal of Heat and Fluid Flow*, 83:108585, 6 2020. ISSN 0142-727X. doi: 10.1016/J.IJHEATFLUIDFLOW.2020.108585.

André Luís Sotero Salustiano Martim, José Gilberto Dalfré Filho, Yvone de Faria Lemos De Lucca, and Ana Ines Borri Genovez. Electromagnetic flowmeter evaluation in real facilities: Velocity profiles and error analysis. *Flow Measurement and Instrumentation*, 66:44–49, 4 2019. ISSN 09555986. doi: 10.1016/j.flowmeasinst.2019.01.001.

M. Sartori, D. S. Oliveira, E. C. Teixeira, W. B. Rauen, and N. C. Reis. CFD modelling of helically coiled tube flocculators for velocity gradient assessment. *Journal of the Brazilian Society of Mechanical Sciences and Engineering*, 37(1):187–198, 1 2015. ISSN 18063691. doi: 10.1007/s40430-014-0141-3.

S. S. Sattarzadeh. *Experimental study of complex pipe flows*. PhD thesis, KTH Mechanics, 2011.

Fabian Schlegel, Kasper Gram Bilde, Mazen Draw, Ilya Evdokimov, Susann Hänsch, Harris Khan, Ronald Lehnigk, Jiadong Li, Hongmei Lyu, Richard Meller, Gašper Petelin, and Matej Tekavčič. HZDR Multiphase Addon for OpenFOAM, 9 2022.

Lalita Kanwar Shekhawat, Jayati Sarkar, Rachit Gupta, Sandeep Hadpe, and Anurag S Rathore. Application of CFD in Bioprocessing: Separation of mammalian cells using disc stack centrifuge during production of biotherapeutics. *Journal of Biotechnology*, 267:1–11, 2 2018. ISSN 0168-1656. doi: 10.1016/J.JBIOTEC.2017.12.016.

Mohsen Shiea, Antonio Buffo, Marco Vanni, and Daniele Marchisio. Numerical Methods for the Solution of Population Balance Equations Coupled with Computational Fluid Dynamics. *Annu. Rev. Chem. Biomol. Eng*, 2020. doi: 10.1146/annurev-chembioeng.

Anuj Kumar Shukla and Anupam Dewan. OpenFOAM based LES of slot jet impingement heat transfer at low nozzle to plate spacing using four SGS models. *Heat and Mass Transfer/Waerme- und Stoffuebertragung*, 55(3):911–931, 3 2019. ISSN 14321181. doi: 10.1007/S00231-018-2470-8/FIGURES/14.

Anders Schou Simonsen. *Modelling and Analysis of Seawater Scrubbers for Reducing SOx Emissions from Marine Engines*. PhD thesis, Aalborg University, Aalborg, 2018.

J. Smagorinsky. General circulation experiments with the primitive equations. *Monthly Weather Review*, 91(3):99–164, 1963. ISSN 00368075. doi: 10.1126/science.12.306.731-a.

M. v. Smoluchowski. Versuch einer mathematischen Theorie der Koagulationskinetik kolloider Lösungen. *Zeitschrift für Physikalische Chemie*, 92(1):129–168, 11 1917. ISSN 2196-7156. doi: 10.1515/ZPCH-1918-9209.

Charles G. Speziale, Sutanu Sarkar, and Thomas B. Gatski. Modelling the pressure–strain correlation of turbulence: an invariant dynamical systems approach. *Journal of Fluid Mechanics*, 227:245–272, 1991. ISSN 1469-7645. doi: 10.1017/S0022112091000101.

Otto Stern. Zur Theorie der Elektrolytischen Doppelschicht. *Zeitschrift für Elektrochemie und angewandte physikalische Chemie*, 30(21-22):508–516, 11 1924. ISSN 0005-9021. doi: 10.1002/BBPC.192400182.

George Gabriel Stokes. On the effect of the internal friction of fluids on the motion of pendulumns. *Transactions of the Cambridge Philosophical Society*, 3:8–106, 1850.

M. Strelets. Detached eddy simulation of massively separated flows. *39th Aerospace Sciences Meeting and Exhibit*, 2001. doi: 10.2514/6.2001-879.

K. Sudo, M. Sumida, and H. Hibara. Experimental investigation on turbulent flow in a circular-sectioned 90-degree bend. *Experiments in Fluids*, 25:42–49, 1998. doi: 10.1007/s003480050206.

K. Sudo, M. Sumida, and H. Hibara. Experimental investigation on turbulent flow through a circular-sectioned 180° bend. *Experiments in Fluids*, 28(1):51–57, 1 2001. ISSN 07234864. doi: 10.1007/s003480050007.

Josef Tausendschön, Jari Kolehmainen, Sankaran Sundaresan, and Stefan Radl. Coarse graining Euler-Lagrange simulations of cohesive particle fluidization. *Powder Technology*, 364:167–182, 3 2020. ISSN 1873328X. doi: 10.1016/j.powtec.2020.01.056.

The OpenFOAM Foundation. OpenFOAM-dev, 2022.

Zhenbo Tong, Wenqi Zhong, Aibing Yu, Hak-Kim Chan, and Runyu Yang. CFD–DEM investigation of the effect of agglomerate–agglomerate collision on dry powder aerosolisation. *Journal of Aerosol Science*, 92:109–121, 2 2016. ISSN 0021-8502. doi: 10.1016/J.JAEROSCI.2015.11.005.

Den Toonder and J M J Nieuwstadt. Reynolds number effects in a turbulent pipe flow for low to moderate Re. *Physics of Fluids*, 9(11):3398–3409, 1997. doi: 10.1063/1.869451.

Olle Törnblom. Turbulent Shear and Breakup of Flocculated Biomaterial in Centrifuge Inlets. *Chemical Engineering & Technology*, 41(12):2366–2374, 12 2018. ISSN 09307516. doi: 10.1002/ceat.201800297.

Una Trivanovic, Joel C Corbin, Alberto Baldelli, Weihan Peng, Jiacheng Yang, Patrick Kirchen, J Wayne Miller, Prem Lobo, Stéphanie Gagné, and Steven N Rogak. Size and morphology of soot produced by a dual-fuel marine engine. *Journal of Aerosol Science journal*, 138:105448, 2019. doi: 10.1016/j.jaerosci.2019.105448.

Yamuna S. Vadasarukkai, Graham A Gagnon, D. Reid Campbell, and Sarah C. Clark. Assessment of hydraulic flocculation processes using CFD. *American Water Works Association*, 103(11):66–80, 2011. doi: 10.1002/j.1551-8833.2011.tb11567.x.

B.G.M. van Wachem. Derivation, Implementation, and Validation of Computer Simulation Models for Gas-Solid Fluidized Beds, 2000.

T Von Kármán. Mechanische Ähnlichkeit und Turbulenz. *Göttinger Nachr*, pages 58–76, 1930.

Lasse Vrale and Roger M Jorden. RAPID MIXING IN WATER TREATMENT. *Journal (American Water Works Association)*, 63 (1):52–58, 1971.

Pei Wang, Shuai Shen, Ling Zhou, and Deyou Liu. Turbulent Aggregation and Deposition Mechanism of Respirable Dust Pollutants under Wet Dedusting using a Two-Fluid Model with the Population Balance Method. *International Journal of Environmental Research and Public Health*, 16, 2019. doi: 10.3390/ijerph16183359.

Xiaochen Wang, Ying Wang, Yuanqi Bai, Peng Wang, and Yuwei Zhao. An overview of physical and chemical features of diesel exhaust particles. *Journal of the Energy Institute*, 92:1864–1888, 2018a. doi: 10.1016/j.joei.2018.11.006.

Xuetao Wang, Baoyu Cui, Dezhou Wei, Zhenguo Song, Yi He, and Andrew E. Bayly. CFD-PBM modelling of tailings flocculation in a lab-scale gravity thickener. *Powder Technology*, 396:139–151, 1 2022. ISSN 1873328X. doi: 10.1016/J.POWTEC.2021.10.054.

Zhenbei Wang, Jun Nan, Xiaoyu Ji, and Yueming Yang. Effect of the micro-flocculation stage on the flocculation/sedimentation process: The role of shear rate. *Science of The Total Environment*, 633:1183–1191, 8 2018b. ISSN 0048-9697. doi: 10.1016/J.SCITOTENV.2018.03.286.

Zhixin Wang, Ramis Örlü, Philipp Schlatter, and Yongmann M. Chung. Direct numerical simulation of a turbulent 90° bend pipe flow. *International Journal of Heat and Fluid Flow*, 73 (January):199–208, 2018c. ISSN 0142727X. doi: 10.1016/j.ijheatfluidflow.2018.08.003.

M. Weickert, G. Teike, O. Schmidt, and M. Sommerfeld. Investigation of the LES WALE turbulence model within the lattice Boltzmann framework. *Computers & Mathematics with Applications*, 59(7):2200–2214, 4 2010. ISSN 0898-1221. doi: 10.1016/J.CAMWA.2009.08.060.

C.Y. Wen and Y.H. Yu. Mechanics of Fluidization. *The Chemical Engineering Progress Symposium Series*, 162:100–111, 1966.

Hulda Winnes, Erik Fridell, and Jana Moldanová. Marine Science and Engineering Effects of Marine Exhaust Gas Scrubbers on Gas and Particle Emissions. *Journal of Marine Science and Engineering*, 8(4):299, 2020. doi: 10.3390/jmse8040299.

Ping Xiang, Yihui Wan, Xun Wang, and Huilan Lian. Numerical simulation and experimental study of electrocoagulation grid flocculation tank. *Water Science and Technology*, 78(4):786–794, 2018. ISSN 02731223. doi: 10.2166/wst.2018.348.

V. Yakhot, S. A. Orszag, S. Thangam, T. B. Gatski, and C. G. Speziale. Development of turbulence models for shear flows by a double expansion technique. *Physics of Fluids A*, 4(7):1510–1520, 1992. ISSN 08998213. doi: 10.1063/1.858424.

Victor Yakhot and Steven A. Orszag. Renormalization group analysis of turbulence. I. Basic theory. *Journal of Scientific Computing 1986 1:1*, 1(1):3–51, 3 1986. ISSN 1573-7691. doi: 10.1007/BF01061452.

Ya Yao, Yi Jun He, Zheng Hong Luo, and Lan Shi. 3D CFD-PBM modeling of the gas-solid flow field in a polydisperse polymerization FBR: The effect of drag model. *Advanced Powder Technology*, 25(5):1474–1482, 9 2014a. ISSN 15685527. doi: 10.1016/J.APT.2014.04.001.

Ya Yao, Jun-Wei Su, and Zheng-Hong Luo. CFD-PBM modeling polydisperse polymerization FBRs with simultaneous particle growth and aggregation: The effect of the method of moments. *Powder Technology*, 272:142–152, 2014b. doi: 10.1016/j.powtec.2014.11.037.

Ya Yao, Jun-Wei Wei Su, and Zheng-Hong Hong Luo. CFD-PBM modeling polydisperse polymerization FBRs with simultaneous particle growth and aggregation: The effect of the method of moments. *Powder Technology*, 272:142–152, 3 2015. ISSN 0032-5910. doi: https://doi.org/10.1016/j.powtec.2014.11.037.

A. Yoshizawa. Statistical theory for compressible turbulent shear flows, with the application to subgrid modeling. *The Physics*

of Fluids, 29(7):2152, 6 1998. ISSN 0031-9171. doi: 10.1063/1.865552.

C. Yuan, F. Laurent, and R. O. Fox. An extended quadrature method of moments for population balance equations. *Journal of Aerosol Science*, 51:1–23, 9 2012. ISSN 0021-8502. doi: 10.1016/J.JAEROSCI.2012.04.003.

Cansheng Yuan, Bo Kong, Alberto Passalacqua, and Rodney O. Fox. An extended quadrature-based mass-velocity moment model for polydisperse bubbly flows. *The Canadian Journal of Chemical Engineering*, 92(12):2053–2066, 12 2014. ISSN 1939-019X. doi: 10.1002/CJCE.22006.

Minshu Zhan, Minghao You, Lingling Liu, Yilin Zhang, Fang Yuan, Baoyu Guo, Guojian Cheng, and Wei Xu. Numerical simulation of mechanical flocculation in water treatment. *Journal of Environmental Chemical Engineering*, 9(4):105536, 8 2021. ISSN 22133437. doi: 10.1016/j.jece.2021.105536.

Zhengjie Zhu, Carlos A. Dorao, D. Lucas, and Hugo A. Jakobsen. On the Coupled Solution of a Combined Population Balance Model Using the Least-Squares Spectral Element Method. *Industrial and Engineering Chemistry Research*, 48(17):7994–8006, 9 2009. ISSN 08885885. doi: 10.1021/IE900088Q.

Istvan Zoltan Jenei, Fabrice Dassenoy, Thierry Epicier, Arash Khajeh, Ashlie Martini, Dairene Uy, Hamed Ghaednia, and Arup Gangopadhyay. Mechanical characterization of diesel soot nanoparticles: in situ compression in a transmission electron microscope and simulations. *Nanotechnology*, 29(8):85703, 1 2018. doi: 10.1088/1361-6528/aaa2aa.

Part II

Papers

Paper A

On the agglomeration and breakage of particles in turbulent flows through pipe bends using CFD-PBE

Kasper Gram Bilde, Ronald Lehnigk, Jakob Hærvig, Fabian Schlegel, Kim Sørensen

The paper has been published in the
Journal of Chemical Engineering Science Vol. 260, pp. 117915, 2022.

The layout has been revised.

On the agglomeration and breakage of particles in turbulent flows through pipe bends using CFD-PBE

Kasper Gram Bilde[1], Ronald Lehnigk[2], Jakob Hærvig[1], Fabian Schlegel[2], Kim Sørensen[1]

[1] *Aalborg University, Department of Energy, Pontoppidanstræde 111, 9220 Aalborg, Denmark*
[2] Helmholtz-Zentrum Dresden-Rossendorf, Institute of Fluid Dynamics, Bautzner Landstraße 400, Dresden 01328, Germany

Keywords: *Multiphase flows; Population balance equation; Population balance modelling; CFD-PBE; Agglomeration and breakage; Turbulence; Flocculation*

Abstract

Predicting the agglomeration and breakage of solid particles is important when designing a compact and efficient water purification process. A coupled computational fluid dynamics model is presented where the population balance equation is applied to track the particle size distribution for a periodic turbulent pipe flow with 180° bends for fluid Reynolds numbers of $15,000 < Re_f < 35,000$ *and pipe bend radii of* $r_B = d_h$, $r_B = 1.5d_h$ *and* $r_B = 2.5d_h$. *The critical parameters in the Euler-Euler model are analysed and values are chosen to describe the agglomeration of soot particles based on an experimentally obtained particle size distribution measured using a Malvern Mastersizer 3000. It is concluded that the particle Sauter mean diameter converges to a constant value independent of the pipe bend radius when* $Re_f > 30,000$. *The Sauter mean diameter increases from* $d_{32} = 42.7\,\mu m$ *to* $d_{32} = 95\,\mu m$ *without changing the total length of the static flocculator by choosing* $r_B = d_h$ *and* $Re_f = 15,000$.

A.1 Introduction

The aggregation and breakage of particles in turbulent flows are relevant to a wide range of industries and applications, involving several topics in the chemical sector. In both the wastewater- and clean water industry, the aggregation and breakage of solid particles are commonly a problem which is investigated and analysed using both experimental and numerical techniques. Examples of industrial applications are the formation of powders (Tong et al., 2016), production of pharmaceuticals (Palzer, 2011), the formation of soot during combustion (Bhandari et al., 2019) and in flocculation systems for water purification purposes (Lee et al., 2014). In this paper, we focus on water purification where the scope of the study is to analyse the particle size distribution for different geometrical configurations and fluid Reynolds numbers.

In wastewater treatment plants solid particles are agglomerated in a stirred reactor or by in-line mixers to reduce sedimentation time (Bratby, 2016). Several researchers have, since the 1970s, carried out experimental studies on particle aggregation systems

(Vrale and Jorden, 1971; David Griffith and Williams, 1972; Mhaisalkar et al., 1991; Adachi et al., 1994; Haarhoff and van der Walt, 2001; Liu et al., 2004; Nan et al., 2016; Wang et al., 2018b). In more recent years, computational fluid dynamics (CFD) has been extensively applied to improve the understanding of applications that are used to agglomerate particles. Traditionally, the performance of wastewater pretreatment systems has been characterised by the velocity gradient and energy dissipation rate, as proposed by Camp and Stein (1943). As these parameters are directly available using CFD, this approach is highly advantageous.

Ducoste and Clark (1999) were among the first to apply CFD to describe particle aggregation in flocculation systems. The authors used the CFD code FIDAP to evaluate the fluid mechanics in a flocculator using the standard k-ε turbulence model. The numerical results were compared to experimental results using laser Doppler velocimetry. However, the CFD code applied by the researchers did not produce accurate results for the energy dissipation for the swirling flow in the reactor.

Bridgeman et al. (2010) highlighted the applicability of CFD in the development of particle aggregation systems for wastewater treatment plants. They analysed the difference and impact of several turbulence models within the Reynolds averaged Navier Stokes (RANS) framework. The authors were successful in highlighting zones in the system where high-velocity gradients were present, causing particles to break up. Historically, flocculation systems have been designed from a global perspective using either the total pressure loss or the power input to the mechanical actuator (Vrale and Jorden, 1971; Mhaisalkar et al., 1991) but Bridgeman et al. (2010) proposed that a local design perspective using CFD improves the overall performance of the application.

To simulate the aggregation and breakage of discrete particles in a continuous flow, several different multiphase methods have been used. A widely applied approach is to couple CFD and the discrete element model (DEM), where discrete particles are tracked using a Lagrangian soft-sphere model. Hærvig et al. (2018) analysed particle deposition and aggregation in straight turbulent pipe flows with a large eddy simulation (LES) in order to adequately describe the turbulence in the continuous phase. A periodic boundary condition was applied to the pipe section, thereby effectively resulting in an infinitely long straight circular pipe. The CFD-DEM model successfully described the aggregation and breakage of dilute particles in a turbulent gas using the surface adhesion theory proposed by Johnson et al. (1971). Dizaji et al. (2019) analysed the collision and breakage of loosely coupled agglomerates in a shear flow using a four-way coupled CFD-DEM approach. The authors demonstrated in high detail, how agglomerates break into several fragments when placed in a shear flow. Furthermore, they showed how two agglomerates can merge into a single agglomerate, bounce off each other, or fragment into several new smaller agglomerates during a collision. The details of the modelling framework for both the particle and fluid phase are extensive, thereby producing accurate results but at a high computational cost.

Due to the high computational demand of the Euler-Lagrangian CFD-DEM approach, alternative methods have been proposed, which are computationally less demanding. They involve an approximate solution of the population balance equation (PBE), which tracks the temporal and spatial evolution of the particle number density function. Several methods have been proposed to solve the PBE, including the least-square spectral element method (Zhu et al., 2009), the finite element method (Ganesan,

2012) and the family of various method of moments (MOM). One of the most widely used approaches is the quadrature method of moments (QMOM), first implemented into the commercial CFD code Fluent by Marchisio et al. (2003) for modelling simultaneous aggregation and breakage of particles. The QMOM solves for a consecutive set of lower-order integer moments of the number density function and utilises Gaussian quadrature for approximating the integral source terms of the PBE. The QMOM was extended by Yuan et al. (2012) to solve the continuous number density function in the Extended QMOM (EQMOM) approach. Passalacqua et al. (2018) implemented the EQMOM into the OpenFOAM CFD library under the OpenQBMM module. The authors successfully described the aggregation of dilute particles in a Taylor-Couette flow reactor.

Another approach to solving the PBE is the class method, alternatively referred to as the sectional or discrete method. Using this approach, the number density function is discretised into a range of size classes, resulting in a set of source term coupled transport equations for individual number concentrations. The integral source terms are transformed into summations over subintervals. Lehnigk et al. (2021) successfully implemented the class method of Kumar and Ramkrishna (1996) into the Euler-Euler model, also referred to as the two-fluid model, of OpenFOAM. They applied it to simulate both the co-current flow of air and water in a vertical pipe as well as the synthesis of titania in a tubular furnace reactor.

The advantage of the QMOM is that it requires a low number of transported scalars to account for statistical moments which makes this method computationally advantageous. This modelling approach, however, does not provide direct information about the number density function, meaning its shape is unknown. It can be obtained with the EQMOM, as it approximates the number density function through a combination of kernel density functions. However, Li et al. (2017) report that the EQMOM can be up to 30 times as computationally demanding as the QMOM, resulting from costly source term calculations. Class methods are costly as well and require a priori knowlegde of the size range, but the number density function is readily available at any point in the computational domain.

In this study, the PBE is solved using the class method implementation of Lehnigk et al. (2021), as the scope of this study is to analyse the impact on the shape of the number density function when altering the geometrical configuration and the fluid Reynolds number. Furthermore, the class method allows for a direct comparison with experimental data, as the size distribution is directly available. The aggregation and breakage of solid particles throughout circular pipe U-bends are modelled and analysed for fluid Reynolds numbers ranging from $15,000 < Re_{\mathrm{f}} < 35,000$ using the Euler-Euler model of OpenFOAM. Special care is taken to model the aggregation, breakage and external force acting on the solid particles and agglomerates suspended in the flow. The numerical results are compared to an experimentally obtained particle size distribution for an in-line flocculator designed to agglomerate soot particles.

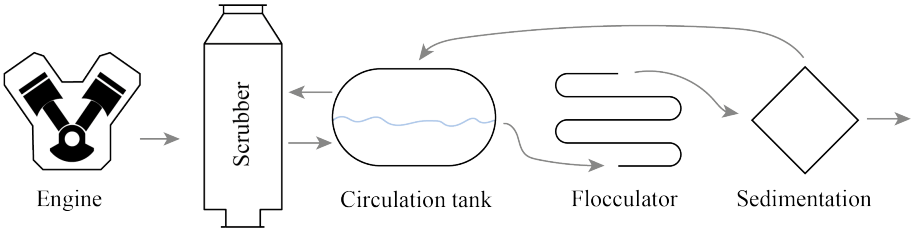

Fig. A.1: Process overview of the system that produces the soot that is agglomerated in the flocculator. Flue gas from a 2 MW engine is cleaned using a wet scrubber, where the soot is trapped in the wet scrubber by a water film. The dirty water is recirculated over the scrubber and through a water purification application. The soot particles are agglomerated in a static flocculator, which is where the particle size distribution is measured.

A.2 Experimental setup

A particle size distribution of agglomerated soot particles was measured and presented in this study for the process seen in Fig. A.1. A 2 MW engine (MAN 9L28/32H) is operated on heavy fuel oil with a sulphur content of 2.5% w/w. As the fuel contains a high sulphur content, a wet scrubber is used to remove the sulphur content from the exhaust gas by scrubbing the exhaust gas with a water film inside the wet scrubber. As a bi-product, up to 40% of the particulate mass in the exhaust gas is trapped by the water film and transferred from the gas phase to the water phase (Simonsen, 2018). The trapped particulate mass in the wet scrubber is primarily soot and black carbon, which is formed within the cylinder of the engine during combustion, and a percentage of residual lube oil. In this study, the particulate mass is assumed as a single component, namely as soot. The water is recirculated over the wet scrubber through a circulation tank and continuously cleaned in a water purification system through fast sedimentation using a high-speed centrifugal separator. The clean water is recirculated back to the circulation tank and the particles are removed from the system as a sludge. To achieve a shorter sedimentation time, the suspended soot particles are agglomerated using an in-line static flocculator consisting of 11x straight pipes followed by 180° pipe bends, which is also seen in Fig. A.2. By producing larger agglomerates over the static flocculator, the water purification process becomes more effective, as a shorter sedimentation time is needed. Aluminium chloride (Kemira PAX-18) is dosed as a metal coagulant at the inlet of the static flocculator to reduce the net surface charge of the soot particles. Further, a highly cationic polymer flocculant (BASF Zetag 9048FS) is dosed into the process stream, in a Venturi-like static mixer after a total of 4x 180° pipe bends, to strengthen and further agglomerate the particles. The net surface charge of the particles is reduced as the soot particles are negatively charged and this makes the particles stable within the suspension.

The static flocculator, shown in more detail in Fig. A.2, features a pipe bend radius of $r_\mathrm{B} = 1.5d_\mathrm{h}$ and is operated at a fluid Reynolds number of $Re_\mathrm{f} = 22,500$, which corresponds to a fluid bulk velocity of $\bar{u}_\mathrm{f} = 0.563\,\mathrm{m/s}$. The particle size distribution of the agglomerated soot is measured for the wet scrubber re-circulation water prior to sedimentation in the water purification application. Agglomerated soot particles

Fig. A.2: In-line pre-treatment static flocculator. The flocculator consists of a set of 180° pipe bends and a metal coagulant is dosed at the inlet of the application and the dosing of the cationic polymer is performed after a total of 4x 180° pipe bends. The particle size distribution is measured at the outlet of the static flocculator.

are extracted at the outlet of the static flocculator and the particle size distribution is analysed using a Malvern Mastersizer 3000, which uses the technique of laser diffraction to measure the particle size distribution. The total suspended solid concentration is measured using EN 872:2005 to determine the particle mass concentration. The volumetric concentration is then estimated using the assumption that soot primarily consists of graphite layers, (Wang et al., 2018a), with a density of $\rho_\mathrm{p} = 1400\ \mathrm{kg/m^3}$ yielding a bulk volumetric concentration of $\alpha_\mathrm{p} = 0.1\%$.

A.3 Numerical framework

The simulations are carried out with the mesh shown in Fig. A.3. The computational domain is designed to use periodic boundary conditions, i.e. the outgoing velocity profile, turbulence characteristics and particle properties are reapplied at the inlet. This effectively results in an infinite number of U-bends followed by a straight section with a length of $L = 20d_\mathrm{h}$, which allows a steady-state solution to be obtained. Pipe bend radii of $r_\mathrm{B} = d_\mathrm{h}$, $r_\mathrm{B} = 1.5d_\mathrm{h}$ and $r_\mathrm{B} = 2.5d_\mathrm{h}$ are analysed in this study, as those are commonly used in industrial applications.

The Euler-Euler model is applied to simulate the fluid and particle flow. In the following sections, the governing equations for the fluid and particle phases as well as the particle-particle interaction are presented.

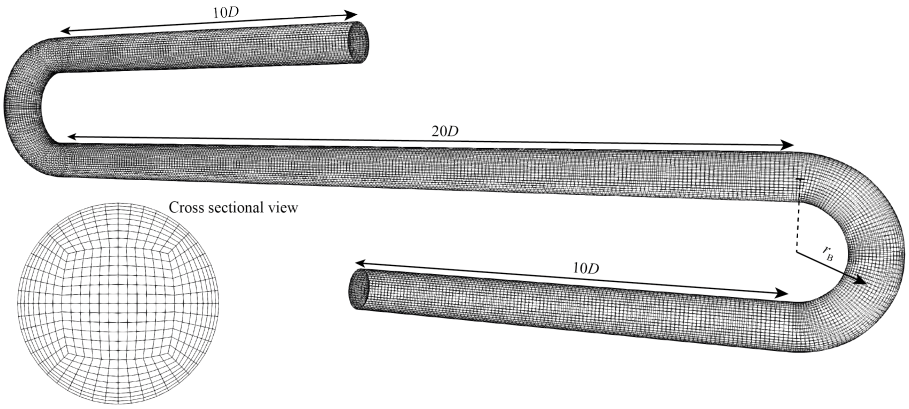

Fig. A.3: Geometrical setup for the computational domain. The domain is periodic, effectively resulting in an infinite number of 180° bends followed by a straight pipe section with lengths of $L = 20d_\mathrm{h}$. In this figure $r_\mathrm{B} = 1.5d_\mathrm{h}$. The mesh resolution of the cross-sectional view is also seen in the figure.

A.3.1 Governing equations for multiphase flow

In the Euler-Euler model, a separate set of equations for continuity and momentum is solved for each phase φ as seen in Eq. (A.1) and (A.2), respectively.

$$\frac{\partial}{\partial t}\left(\alpha_\varphi \rho_\varphi\right) + \nabla \cdot \left(\alpha_\varphi \rho_\varphi \boldsymbol{u}_\varphi\right) = 0 \tag{A.1}$$

$$\begin{aligned}\frac{\partial}{\partial t}\left(\alpha_\varphi \rho_\varphi \boldsymbol{u}_\varphi\right) + \nabla \cdot \left(\alpha_\varphi \rho_\varphi \boldsymbol{u}_\varphi \boldsymbol{u}_\varphi\right) - \nabla \cdot \tau_\varphi = &-\alpha_\varphi \nabla p + \alpha_\varphi \rho_\varphi \boldsymbol{g} \\ &+ \boldsymbol{M}_\varphi + \boldsymbol{S}_\varphi,\end{aligned} \tag{A.2}$$

where α is the volumetric fraction, ρ the density, $\boldsymbol{u}$ the velocity, $\boldsymbol{S}$ represents the momentum source due to volume forces, $\boldsymbol{g}$ the gravitational acceleration, p the pressure, $\boldsymbol{\tau}$ the stress tensor, which also includes the Reynolds stresses for the fluid phase and $\boldsymbol{M}_\varphi$ is the rate of interfacial momentum transfer between the phases which is given by

$$\boldsymbol{M}_\varphi = \sum_{\varphi=0, \varphi\neq\psi}^{N} \left(\boldsymbol{F}_{\mathrm{D},\varphi\psi} + \boldsymbol{F}_{\mathrm{L},\varphi\psi} + \boldsymbol{F}_{\mathrm{VM},\varphi\psi} + \boldsymbol{F}_{\mathrm{disp},\varphi\psi}\right), \tag{A.3}$$

where the subscripts denotes drag force, D, lift force, L, virtual mass force, VM, and turbulent dispersion force, disp, between phase φ and ψ. Conservation of momentum implies that $\sum_\varphi \boldsymbol{M}_\varphi = 0$. It is assumed that the pressure is shared between the phases. A momentum source term $\boldsymbol{S}_\varphi$ is applied for the fluid phase in this study to balance the pressure gradient in the periodic domain, which acts to ensure a mean bulk velocity corresponding to the fluid Reynolds number chosen. To this end, a pressure gradient increment is added to the existing pressure gradient of the fluid phase for each iteration, based on the difference between the fluid velocity and the desired bulk velocity at the given time step.

Turbulence modelling

Several authors have applied the re-normalisation group turbulence model (RNG) by Yakhot and Orszag (1986), to successfully describe the turbulence in swirling flows, such as flow through a pipe bend or fluid separation flows (Hilgenstock and Ernst, 1996; Kim et al., 2014; Cai et al., 2019; Marshall and Bakker, 2004). Kim et al. (2014) analysed the accuracy of several turbulence models for a 90° pipe bend including the standard k-ε, realizable k-ε, RNG-k-ε, k-ω SST model. The authors concluded that the RNG k-ε model yields good agreement for the primary stream-wise velocity and secondary swirling velocity profile compared to the other turbulence models.

Escue and Cui (2010) compared the accuracy of the RNG k-ε to the Reynolds stress model (RSM) which generally has a better prediction of turbulence, but is also more computationally expensive. The authors concluded that the results obtained by the RNG k-ε model were in better agreement with experimental data compared to the RSM for low swirling flows. Since the swirling flow is produced by a pipe bend, it is assumed that the RNG k-ε produces suitable turbulence results for this study.

The two-equation RNG k-ε model is developed by applying statistical methods used in re-normalisation group theory to resolve the smallest eddies in the inertial range. The RNG procedure removes the small scales of motion by expressing their effects in terms of larger-scale motion and modifying the turbulent viscosity. The governing equations for the RNG k-ε model by Yakhot et al. (1992) are

$$\frac{\partial}{\partial t}\left(\alpha_\mathrm{f}\rho_\mathrm{f}k\right) + \nabla\cdot\left(\alpha_\mathrm{f}\rho_\mathrm{f}k\boldsymbol{u}_\mathrm{f}\right) = \nabla\left[\left(\mu_\mathrm{f} + \frac{\mu_\mathrm{t}}{\sigma_\mathrm{k}}\right)\nabla k\right] + P_k - \alpha_\mathrm{f}\rho_\mathrm{f}\varepsilon \tag{A.4}$$

and

$$\begin{aligned}\frac{\partial}{\partial t}\left(\alpha_\mathrm{f}\rho\varepsilon\right) + \nabla\cdot\left(\alpha_\mathrm{f}\rho_\mathrm{f}\varepsilon\boldsymbol{u}_\mathrm{f}\right) = \nabla\left[\left(\mu_\mathrm{f} + \frac{\mu_\mathrm{t}}{\sigma_\varepsilon}\right)\nabla\varepsilon\right] + C_{1\varepsilon}\frac{\varepsilon}{k}P_k \\ -C_{2\varepsilon}\alpha_\mathrm{f}\rho\frac{\varepsilon^2}{k}\,,\end{aligned} \tag{A.5}$$

where the subscript f denotes the fluid phase and P_k the generation of turbulence due to the mean velocity gradients. The model coefficients chosen for the RNG k-ε model used in this work are the default values.

Kinetic theory of granular flows

The stress tensor for the dispersed particle phase, $\boldsymbol{\tau}_\mathrm{p}$, is modelled using the kinetic theory of granular flows to account for the particle-particle interactions (Lun et al., 1984; van Wachem, 2000; Yao et al., 2015; Shekhawat et al., 2018). An extensive description of the KTGF model and a comparison of the submodels included is presented by van Wachem (2000). The submodels selected here are listed in Table A.1 and the corresponding mathematical expressions can be found in A.A.

A.3.2 Interfacial momentum transfer models

The rate of interfacial momentum transfer can be divided into several submodels accounting for the different fluid forces acting on the particles. The interfacial forces

Table A.1: Submodels applied for the KTGF.

Description	Author
Conductivity of granular energy	Hrenya and Sinclair (1997)
Frictional stress	Johnson and Jackson (1987)
Generation and dissipation of granular energy	Lun et al. (1984)
Particle shear viscosity	Hrenya and Sinclair (1997)
Particle phase pressure	Lun et al. (1984)
Radial distribution function	Lun and Savage (1986)

are defined by the drift velocity between the two phases, $\boldsymbol{u}_\mathrm{r} = \left|\boldsymbol{u}_\mathrm{p} - \boldsymbol{u}_\mathrm{f}\right|$ or the particle Reynolds number, $\mathrm{Re}_\mathrm{p} = \boldsymbol{u}_\mathrm{r} d_\mathrm{p}/\nu_\mathrm{f}$.

Drag force

The drag force acting on the particles is described by Eq. (A.6)

$$\boldsymbol{F}_\mathrm{D} = \frac{1}{2}\rho_\mathrm{f} \left|\boldsymbol{u}_\mathrm{r}\right| \boldsymbol{u}_\mathrm{r} C_\mathrm{D} A_\mathrm{p}\,, \tag{A.6}$$

where C_D is the drag coefficient and A_p is the projected surface area of the particles as seen by the fluid. The particles are assumed spherical and the drag force coefficient presented by Wen and Yu (1966) is used in this study which reads

$$C_\mathrm{D} = \begin{cases} \frac{24}{Re_\mathrm{p}}\alpha_\mathrm{f}^{-2.65} & \text{for } Re_\mathrm{p} < 0.5 \\ \frac{24}{Re_\mathrm{p}}\left(1 + 0.15 Re_\mathrm{p}^{0.687}\right)\alpha_\mathrm{f}^{-2.65} & \text{for } 0.5 \leq Re_\mathrm{p} < 1000 \\ 0.44\alpha_\mathrm{f}^{-2.65} & \text{for } Re_\mathrm{p} \geq 1000\,. \end{cases} \tag{A.7}$$

Assuming the soot particles and agglomerates to be spherical is, of course, a simplification, as these are fractal-like in their nature. According to the observations of Mikhailov et al. (2006) and Ma et al. (2013) soot structures tend to collapse when entering a wet environment and thereby become quite spherical. Furthermore, as the particles are small, so is the Stokes number. For the largest particles it evaluates to $\mathrm{St} < 0.2$ and for the majority $\mathrm{St} << 1$, meaning that the relative velocity between the phases is small. The particles largely follow the flow and the effect of assuming sphericity is negligible.

Lift force

The dispersed particles are affected by shear and rotational forces in this study. The lift force acting on a dispersed phase by a continuous phase can be described as

$$\boldsymbol{F}_\mathrm{L} = -C_\mathrm{L}\rho_\mathrm{f}\alpha_\mathrm{p}\boldsymbol{u}_\mathrm{r} \cdot \boldsymbol{\omega}\,, \tag{A.8}$$

where C_L is the lift force coefficient and $\boldsymbol{\omega}$ is the vorticity defined by the curl operator as $\boldsymbol{\omega} = \nabla \times \boldsymbol{u}_f$. The lift force coefficient by Saffman (1965) describes the lift force coefficient for low Reynolds numbers as

$$C_L = \frac{3}{2\pi\sqrt{Re_\omega}} C'_L \tag{A.9}$$

where $C'_L = 6.46$ and the vorticity Reynolds number is given as $Re_\omega = |\boldsymbol{\omega}| d_p^2/\nu_f$. Mei (1992) extended the lift force coefficient to cover finite Reynolds numbers and extended the applicable range. The lift force coefficient, C'_L, is given as

$$C'_L = \begin{cases} 6.46\left[\left(1 - 0.3314\beta^{0.5}\right)e^{-0.1Re_p} + 0.3314\beta^{0.5}\right] & Re_p \leq 40 \\ 6.46 \cdot 0.0524\sqrt{\beta Re_p} & Re_p > 40\,, \end{cases} \tag{A.10}$$

where $\beta = 0.5\left(Re_\omega/Re_p\right)$.

Virtual mass force

The virtual mass force describing the additional mass of the fluid being accelerated along with the particulate mass is seen in Eq. (A.11).

$$\boldsymbol{F}_{VM} = -C_{VM}\rho_f\alpha_p\left(\frac{D_p}{Dt}\boldsymbol{u}_p - \frac{D_f}{Dt}\boldsymbol{u}_f\right), \tag{A.11}$$

where C_{VM} is the virtual mass force coefficient, and for this study, a constant value of $C_{VM} = 0.5$ is applied. The term D_p/Dt and D_f/Dt denotes the material derivative for the particle and fluid phase respectively.

Turbulent dispersion force

The turbulence in the continuous phase, described by the turbulent diffusion term, is based on the averaged velocity field when using the RANS methodology. This means that the turbulent eddies in the continuous phase do not directly impact the dispersed phase as the eddies are modelled and not resolved. To account for the turbulent dispersion of the dispersed phase, Burns et al. (2004) performed a Favre averaging of the drag force. The turbulent dispersion force is given as

$$\boldsymbol{F}_{disp} = -\frac{3}{4}C_D\frac{\alpha_p\rho_f}{d_p}\boldsymbol{u}_r\frac{\nu_t}{\sigma}\left(\frac{\nabla\alpha_f}{\alpha_f} - \frac{\nabla\alpha_p}{\alpha_p}\right), \tag{A.12}$$

where σ is the turbulent Schmidt number, which is set to a value of $\sigma = 0.9$ in this study.

A.3.3 Population balance equation

The evolution of the particle size distribution is described using the population balance equation, a transport equation for the number density function, $n(\xi, \mathbf{x}, t)$, where ξ is the internal coordinate and $\mathbf{x}$ is the spatial coordinate. In this study, the particle size distribution is of interest, which is why the internal coordinate is the volume of

the particles, $\xi = v_p$. For ease of notation and since all terms depend on the spatial dimension and time, the number density function is denoted by n_v. The population balance equation is given as

$$\frac{\partial}{\partial t} n_v + \nabla \cdot (\boldsymbol{u} n_v) = S_v \,, \tag{A.13}$$

where S_v is the source term accounting for the discontinuous changes in the number density function such as aggregation and breakage, given by

$$S_v = \frac{1}{2} \int_0^v n_{v'} n_{v-v'} a_{v',v-v'} \mathrm{d}v' - n_v \int_0^\infty n_{v'} a_{v,v'} \mathrm{d}v' + \int_v^\infty n_{v'} b_{v'} \beta_{v,v'} \mathrm{d}v' - n_v b_v \,. \tag{A.14}$$

The birth and death by aggregation are given by the first two terms on the right-hand side and $a_{v,v'}$ denotes the corresponding aggregation frequency. Birth and death by breakage are described by the third and fourth term on the right-hand side of Eq. (A.14), where $b_{v'}$ denotes the corresponding breakage frequency. During breakage, information about the number and distribution of daughter particles is given by the daughter size distribution function, $\beta_{v,v'}$, which must satisfy the constraints

$$\int_0^{v'} v \beta_{v,v'} \mathrm{d}v = v' \,, \tag{A.15}$$

and

$$\int_0^{v'} \beta_{v,v'} \mathrm{d}v = n_\beta \,, \tag{A.16}$$

where n_β is the total number of daughter particles born from particle breakage. The daughter size distribution function for this study is presented in section A.3.3.

Eq. (A.13) is solved by discretising the particle size domain into a set of size classes with an upper and lower boundaries, v_i and v_{i+1}, respectively. The number concentration, N, is given by integrating over the resulting size class

$$N_i = \int_{v_i}^{v_{i+1}} n_v \mathrm{d}v \,. \tag{A.17}$$

The discretised version of Eq. (A.13) using Eq. (A.17) yields

$$\frac{\partial N_i}{\partial t} + \nabla \cdot (\mathbf{u} N_i) = S_i \,. \tag{A.18}$$

The source term in Eq. (A.18) is obtained using the formulation proposed by Kumar and Ramkrishna (1996), where it is assumed that the population is concentrated at pivotal volumes and the mean value theorem is applied for computing the frequencies.

A separate transport equation is solved for each size class. The volume concentration of the particle phase is then given as:

$$\alpha_{\mathrm{p}} = \sum_{i=0}^{k} x_i N_i \,, \tag{A.19}$$

where x_i is the pivotal volumes of the size class. For further details of the algorithm, the reader is referred to the work of Lehnigk et al. (2021).

Aggregation kernel

The birth and death of new particles due to aggregation are based on an aggregation kernel describing the aggregation frequency. In this work, the aggregation kernel proposed by Adachi et al. (1994) is adopted. It has been applied successfully by Marchisio et al. (2003) and Cai et al. (2019) to describe the aggregation of particles in turbulent flows. The aggregation frequency model is

$$a_{d,d'} = \frac{4}{3}\sqrt{\frac{3\pi}{10}}\sqrt{\frac{\varepsilon_{\mathrm{f}}}{\nu_{\mathrm{f}}}}\left(d + d'\right)^3 \,, \tag{A.20}$$

where ε_{f} is the turbulent dissipation rate of the continuous phase and ν_{f} is the kinematic viscosity of the continuous phase.

Breakage kernel

The birth and death of particles due to breakage are described by the breakage kernel. Here, the model proposed by Kusters (1991) is adopted. The breakage frequency model is an exponential kernel given by

$$b_{v'} = \sqrt{\frac{4}{15\pi}}\sqrt{\frac{\varepsilon}{\nu_{\mathrm{f}}}}\exp\left(-\frac{\varepsilon_{\mathrm{cr}}}{\varepsilon}\right) \,, \tag{A.21}$$

where $\varepsilon_{\mathrm{cr}}$ is the critical rate of energy dissipation required for the agglomerate to break up. The critical rate of energy dissipation is defined as

$$\varepsilon_{\mathrm{cr}} = \frac{B}{r_{\mathrm{c}}} \,, \tag{A.22}$$

where B is a strength parameter that accounts for the critical shear velocity needed to break an agglomerate and r_{c} is the collision radius, which is based on a correlation proposed by Mandelbrot (1985):

$$r_{\mathrm{c}} = r_0\left(\frac{n_i}{k_{\mathrm{c}}}\right)^{1/D_{\mathrm{f}}} \,. \tag{A.23}$$

Herein, r_0 is the radius of the primary particle in the agglomerate, n_i is the number of primary particles in the agglomerate, k_c is a constant relative to the packing density which is generally assumed to be unity (Jeldres et al., 2017) and D_{f} is the fractal

dimension. The number of primary particles , n_i, is given by Eq. (A.24), where r_i is the radius of the agglomerate.

$$n_i = \left(\frac{r_i}{r_0}\right)^{D_f} . \tag{A.24}$$

The critical strength of the agglomerate is thereby a function of the fractal dimension and the number of primary particles in the agglomerate, meaning larger agglomerates are more likely to break compared to smaller agglomerates.

Daughter size distribution

A size distribution model is needed when an agglomerate breaks into smaller fragments (daughters particles). For this study a beta distribution function is chosen for the newly formed particles. Laakkonen et al. (2007) proposed a beta distribution that is a function of the number of daughter particles and is given as

$$\beta_{v,v'} = (1 + C_4)(2 + C_4)(3 + C_4)(4 + C_4)\left(\frac{1}{3}\right)\left(\frac{1}{v'}\right)\left(\frac{v}{v'}\right)^2 \left(1 - \frac{v}{v'}\right)^{C_4} , \tag{A.25}$$

where v is the volume of the daughter particle and v' is the volume of the mother particle. The total number of daughters generated is a function of the coefficient, C_4:

$$n_i = \frac{4}{3} + \frac{C_4}{3} . \tag{A.26}$$

A.4 Results and Discussion

A.4.1 Simulation parameters

The particle properties used for the simulations are seen in Table A.2. The primary particle size of the agglomerates is chosen based on the measurements of Trivanovic et al. (2019) and the fractal dimension selected according to the measurements of Mikhailov et al. (2006) and Ma et al. (2013). The particle size range is discretised into 50 size classes that are distributed equally on the logarithmic scale in the range of $1\ \mu\text{m} < d_\text{p} < 1000\ \mu\text{m}$ as

$$\log_{10}\left(\frac{d_{\text{p},i}}{d_{\text{p},i-1}}\right) = \frac{\log_{10}\left(\frac{d_{\text{p},N}}{d_{\text{p},1}}\right)}{N-1} \qquad 1 < i < N . \tag{A.27}$$

To ensure computational stability the Courant–Friedrichs– Lewy (CFL) condition, which determines the maximum allowed time step by considering the mesh size, is set to a maximum value of $\text{CFL} = |\boldsymbol{u}_\text{f}|\,\Delta t/\Delta x < 1$. The simulations were continued until a steady-state solution was obtained, which was found to be dependent on the fluid Reynolds number and the geometrical setup for the specific case. Dependent

Table A.2: Particle properties applied for the simulations.

Property	Symbol	Value	Unit
Density	ρ_p	1400	$\mathrm{kg/m^3}$
Primary particle size	d_0	250	nm
Fractal dimension	D_f	2.4	-
Coefficient of restitution	e	0.75	-

on the case, a steady-state solution was obtained after a dimensionless flow length of $300 < \tilde{L} < 1000$, where $\tilde{L} = t \cdot \bar{u}_\mathrm{f}/d_\mathrm{h}$ and $\bar{u}_\mathrm{f}$ is the mean bulk velocity of the fluid. Common for all geometrical cases was that the steady-state solution was obtained faster with increasing fluid Reynolds number.

The experiment features a total dimensionless length of $\tilde{L} = 500$. A length of $\tilde{L} = 350$ is experienced by the fluid after the polymer flocculant is dosed into the process stream. In the simulation, the particulate phase is inserted into a fully developed flow field and then the dimensionless flow length needed to obtain a steady-state solution for the particle size distribution is analysed. For the numerical simulation with a fluid Reynolds number of $Re_\mathrm{f} = 22,500$, the dimensionless length to reach the steady-state solution is seen in Fig. A.4. The steady-state solution for the particle size distribution is obtained after a dimensionless flow length of $\tilde{L} \approx 450$. It is therefore concluded that a periodic computational domain can be used to obtain steady-state solutions for the given geometry. The no-slip condition is applied to the walls of the domain for both phases.

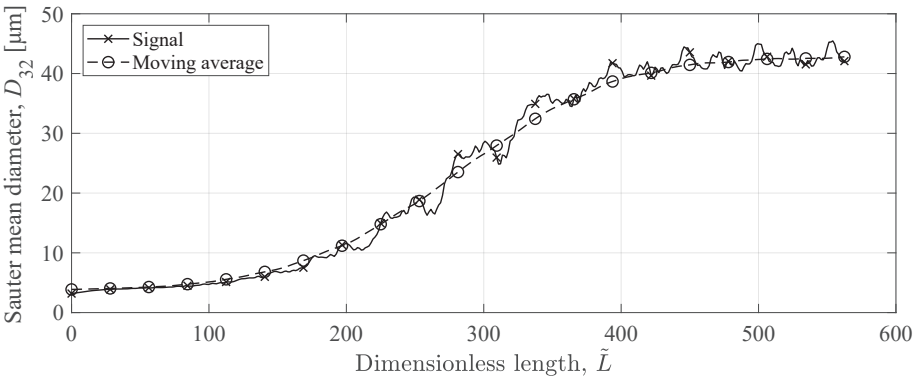

Fig. A.4: Sauter mean diameter as a function of the dimensionless flow length, $\tilde{L}$ for $r_\mathrm{B} = 1.5d_\mathrm{h}$, $Re_\mathrm{f} = 22,500$, $B = 50 \cdot 10^{-7}$ and $C_4 = 2$.

A.4.2 Mesh independence study

The number of computational cells in the domain is increased to a point where a solution that is independent of the number of computational cells is obtained. The parameter

of interest in this study is the particle size distribution and the volume-averaged Sauter mean diameter which is seen in Fig. A.5 for three different mesh sizes. The coarse mesh consists of 97,000 cells, the medium mesh consists of 313,000 cells and the fine mesh consists of 521,000 cells. The mesh is refined in the axial and radial direction, but keeping a constant minimum cell size at the wall. A mesh independent particle size distribution is obtained using the medium-sized mesh, which is also the computational mesh seen in Fig. A.3.

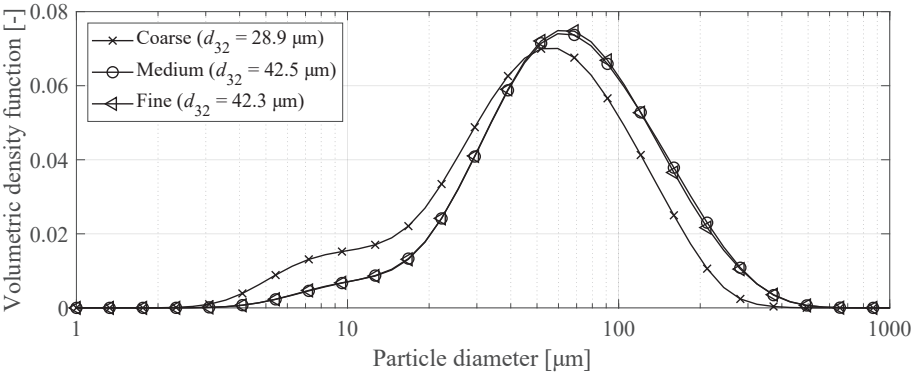

Fig. A.5: Particle size distribution for three different computational mesh sizes with the parameters of $Re_f = 22,500$, $r_B = 1.5d_h$, $B = 50 \cdot 10^{-7}$ and $C_4 = 2$.

A.4.3 Validation of model parameters

Two model properties are varied to find particle characteristics that resemble the experimental measurements. The particle critical strength parameter, B, and the daughter size distribution coefficient, C_4, is varied to see the effect of that given parameter and to find suitable properties for the particles.

Critical strength parameter

The particle strength parameter, B, is varied for a constant fluid Reynolds number, to analyse the effect on the particle size distribution when changing the critical strength. The fluid Reynolds number resembles that of the experimental measurements, $Re_f = 22,500$, and the strength parameter was varied from $40 \cdot 10^{-7} < B < 60 \cdot 10^{-7}$. The daughter size distribution coefficient C_4 is set to $C_4 = 2$ for this parameter study. The steady-state particle size distribution at the outlet of the domain is seen in Fig. A.6. The shape of the particle size distribution is similar for the three values of B, but the peak of the particle size distribution increases as B decreases. Using a strength parameter of $B = 50 \cdot 10^{-7}$ m^3/s^3 produces results that are in good agreement with the experimentally obtained particle size distribution. This value will be used for further analysis of the impact of the fluid Reynolds number and the effect of the pipe bend radius.

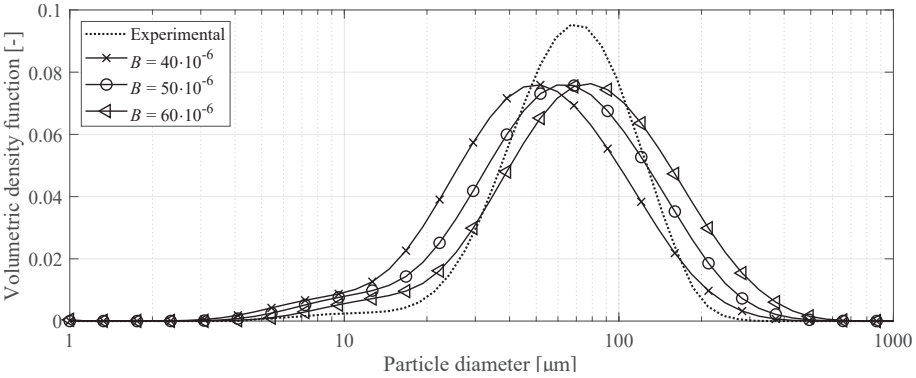

Fig. A.6: Particle size distribution for strength parameters, B, compared to experimentally obtained particle size distribution using a Malvern Mastersizer 3000. Lowering the strength parameters results in an increased number of smaller particles.

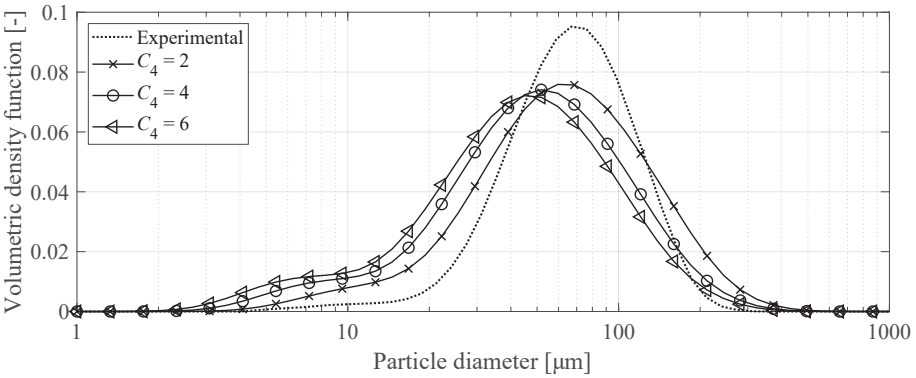

Fig. A.7: Particle size distribution of $Re_f = 22,500$ and $r_B = 1.5d_h$ for different daughter size distribution coefficients, C_4, with the experimentally obtained particle size distribution for reference.

Daughter size distribution coefficient

For studying the impact of the daughter size distribution coefficient C_4, simulations are carried out using $C_4 = 2$, $C_4 = 4$ and $C_4 = 6$. The number of agglomerate fragments increases with the coefficient, meaning that smaller daughter particles are favoured. The particle size distribution for the different daughter distribution coefficients is seen in Fig. A.7, where the experimentally measured particle size distribution is shown for reference. An increased concentration of smaller particles is observed when C_4 increases, as expected. It is seen that a daughter size distribution coefficient of $C_4 = 2$ produces a particle size distribution in good agreement with the experimental results, which corresponds to binary breakage according to Eq. (A.26).

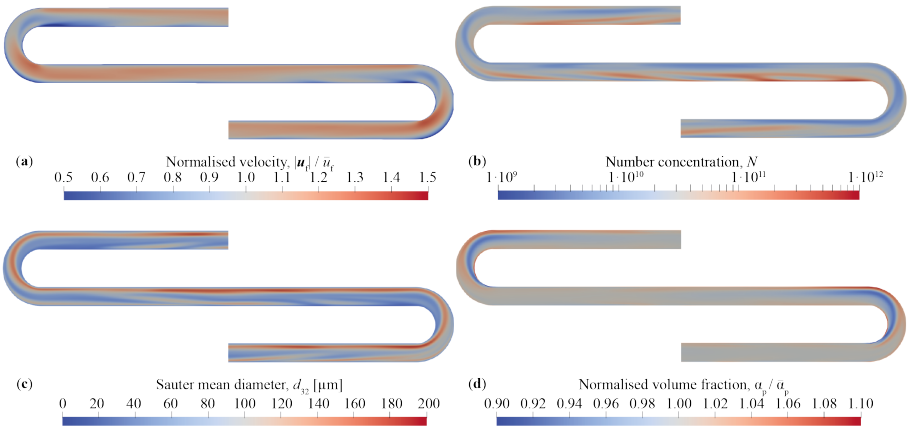

Fig. A.8: Steady-state contour plots for the geometrical symmetry plane of the computational domain for $Re_f = 22,500$, $B = 50 \cdot 10^{-7}$ and $C_4 = 2$. (**a**): Normalised fluid velocity, $|\boldsymbol{u}_f| / \bar{u}_f$. (**b**): Number concentration of the particle phase. (**c**): Sauter mean diameter, d_{32}, of the particle phase. (**d**): Normalised volume fraction of the particle phase, $\alpha_f / \bar{\alpha}_f$.

A.4.4 Flow field

The normalised fluid velocity, $|\boldsymbol{u}_f| / \bar{u}_f$, is seen, as a contour in the middle of the pipe, in Fig. A.8a for $Re_f = 22,500$ and $r_B = 1.5 d_h$. Larger absolute velocities are observed at the beginning of the pipe U-bend, as the fluid is forced towards the outer radius of the bend, due to the strong curvature which effectively causing a downstream separation zone. The separation zone is a function of the curvature of the bend and also of the velocity of the fluid, as the fluid is more prone to stay attached at lower velocities. The high-velocity zones are also the zones with the highest velocity gradients, as the fluid changes direction within the U-bends. Therefore, the U-bends are the zones where the particles are most prone to breakage, which is seen when analysing the contours of the particle number concentration and the Sauter mean diameter in Fig. A.8b and A.8c, respectively. The high curvature of the bend forces the two phases to separate and a larger volume fraction is observed in the 180° bend, as seen when analysing the normalised volume fraction of the particle phase in Fig. A.8d. The heavier particle phase is forced towards the circumference of the bend.

A.4.5 Variation of flow parameters

The fluid Reynolds number and the geometrical setup of the 180° bend are varied to study their effect on the particle size distribution. These parameters are chosen to analyse the effect of increasing the volumetric flow rate through the same static flocculator or changing the bend radius of the static flocculator in the design process.

Fluid Reynolds number

The fluid Reynolds number is varied in the range of $15,000 < Re_f < 35,000$ and the resulting steady-state particle size distributions are seen in Fig. A.9. When the

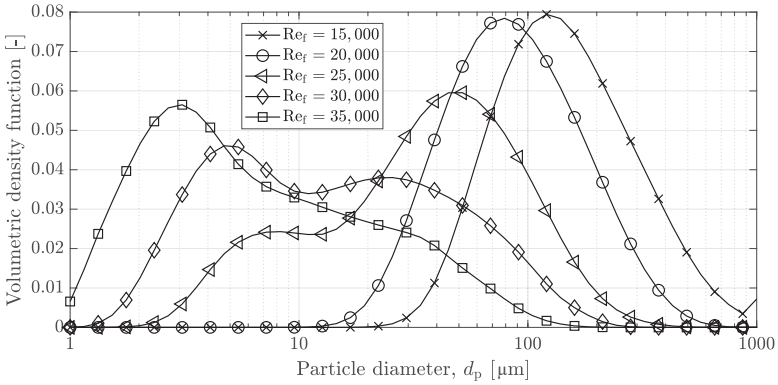

Fig. A.9: Particle size distribution for different fluid Reynolds numbers for $r_B = 1.5d_h$.

fluid Reynolds number increases, more turbulence is generated. This means that the turbulent energy dissipation rate increases overall in the computational domain and also at the 180° bends. As a result, breakage outweighs aggregation, thereby resulting in a distribution that is shifted towards smaller sizes.

It is observed how the mean particle diameter decreases along the inner circumference of the 180° bend when analysing the contour plot of the Sauter mean diameter in Fig. A.8c. This is also where the turbulent energy dissipation rate is largest, which is causing the particles to break up. Downstream of the U-bend the mean particle diameter increases again as the turbulent dissipation rate decreases, resulting in an increased agglomeration.

Pipe bend radius

To analyse the impact of the geometrical setup, the bend radius of the pipe is varied. Three of the most common industrial bend radii are used: $r_B = d_h$, $r_B = 1.5d_h$ and $r_B = 2.5d_h$. The fluid Reynolds number is again varied within the range of $15,000 < Re_f < 35,000$ and the Sauter mean diameter is plotted as a function of the fluid Reynolds number in Fig. A.10. It is seen that as the fluid Reynolds number increases, the particle Sauter mean diameter decreases and converges to a constant value for all pipe bend radii. This effect is due to more turbulence being induced in the fluid domain, thereby increasing the turbulent energy dissipation rate in the overall computational domain. It is therefore observed that the bend radius of the pipe has a negligible impact on the Sauter mean diameter of the particles if the fluid Reynolds number exceeds $Re_f > 30,000$, for the particle properties chosen.

When analysing the dimensionless length needed to obtain a steady-state solution, $\tilde{L}_{SS}$, in Fig. A.11, it is seen that the response length of the system increases with the bend radius of the pipe. It is also observed that the response length decreases when

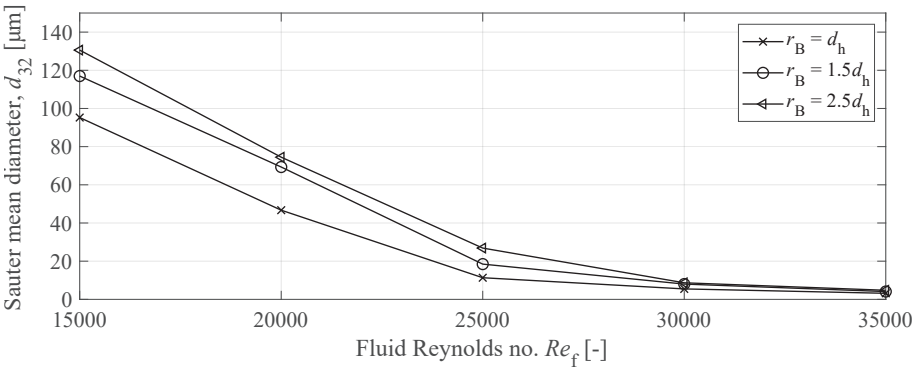

Fig. A.10: Sauter mean diameter, d_{32}, as a function of the fluid Reynolds number for three different pipe bend radii.

the fluid Reynolds number increases. The experimental setup, see Fig. A.2, has a total dimensionless length of $\tilde{L} = 500$, and therefore the largest particle size distribution that can be obtained within this length is given by choosing a bend radius of $r_B = d_h$ and a fluid Reynolds number of $Re_f = 15,000$. By choosing this configuration, the Sauter mean diameter increases from $d_{32} = 42.7\,\mu m$ to $d_{32} = 95\,\mu m$ without changing the dimensionless length of the experimental setup.

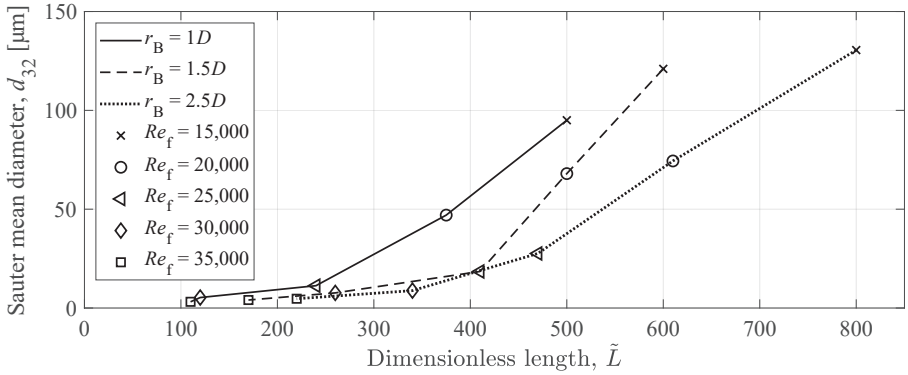

Fig. A.11: Sauter mean diameter, d_{32}, as a function of the dimensionless length $\tilde{L}_{SS}$ needed to obtain a steady-state solution for the different bend radii and fluid Reynolds numbers.

A.5 Conclusion

A numerical model for predicting the particle size distribution when accounting for particle agglomeration and breakage is presented in this study in conjunction with an experimentally obtained particle size distribution of flocculated soot particles. The fluid and particle phases are modelled using the multi-fluid model , where the particle

number density function is tracked by solving the population balance equation with the method of classes. Special care is taken to account for the interfacial momentum transfer between the fluid and solid phase. Furthermore, agglomeration and breakage kernels are applied for the turbulent regime, to obtain a steady-state solution for the particle size distribution.

Several simulations are carried out to analyse and find suitable parameters that describe the agglomeration and breakage of soot-like particles in the Euler-Euler model. Using the critical turbulent energy dissipation rate and daughter size distribution, suitable numerical parameters are presented which obtain results in good agreement with the experimental data.

The particle size distribution for fluid Reynolds numbers in the range of $15,000 < Re_\mathrm{f} < 35,000$ is analysed for three different pipe bend radii of $r_\mathrm{B} = d_\mathrm{h}$, $r_\mathrm{B} = 1.5d_\mathrm{h}$ and $r_\mathrm{B} = 2.5d_\mathrm{h}$. It is shown that the pipe bend radius has a negligible impact on the Sauter mean diameter when the fluid Reynolds number exceeds $Re_\mathrm{f} > 30,000$ for the selected particle parameters. It has been shown that the Sauter mean diameter can be increased from $d_{32} = 42.7\,\mu\mathrm{m}$ to $d_{32} = 95\,\mu\mathrm{m}$ by decreasing the pipe bend radius from $r_\mathrm{B} = 1.5d_\mathrm{h}$ to $r_\mathrm{B} = d_\mathrm{h}$ and decreasing the fluid Reynolds number from $Re_\mathrm{f} = 22,500$ to $Re_\mathrm{f} = 15,000$ while maintaining a maximum flow length of $\tilde{L} = 500$.

A.6 Acknowledgements

This work is financially supported by the Danish Innovation Foundation under grant no. 9065-00188B. Special appreciation is given to Anders Schou Simonsen and Thomas Condra for their valuable inputs and comments during this work.

A.7 Additional information

The implementation of the aggregation- and breakage kernels as well as the Saffman-Mei lift force models is published through the HZDR Multiphase Addon for OpenFOAM (Schlegel et al., 2022) and has also been contributed to the main OpenFOAM release (The OpenFOAM Foundation, 2022).

A.A Submodels applied for KTGF theory

Mathematical equations for the submodels applied for the kinetic theory of granular flow is presented in this appendix to support Table A.1.

A.A.1 Radial distribution function

The mathematical expression for the radial distribution function, g_0, by Lun and Savage (1986) is given as

$$g_0 = \left(1 - \frac{\alpha_\mathrm{p}}{\alpha_\mathrm{p,max}}\right). \tag{A.28}$$

A.A.2 Conductivity of granular energy

The mathematical expression of Hrenya and Sinclair (1997) to account for conductivity of granular energy is given by

$$\kappa = \frac{25\sqrt{\pi\Theta}}{128}\rho_\mathrm{p} d_\mathrm{p}\left[\left(\frac{1}{1+\frac{\lambda_\mathrm{mfp}}{R}}\frac{8}{\eta g_0}+\frac{96\alpha_\mathrm{p}}{5}\right)\left(\frac{1+\frac{12}{5}\eta^2(4\eta-3)\alpha_\mathrm{p} g_0}{41-33\eta}\right)+\frac{512}{25\pi}\eta\alpha_\mathrm{p}^2 g_0\right], \tag{A.29}$$

where Θ is the granular energy, λ_{mfg} is the mean free path, e is the coefficient of restitution, $\eta = 1/2\,(1+e)$ and R is the characteristic length.

A.A.3 Frictional stress

The semi-empirical equation proposed by Johnson and Jackson (1987) for the normal frictional stress, P_f, is given as

$$P_\mathrm{f} = \mathrm{Fr}\frac{\left(\alpha_\mathrm{p}-\alpha_\mathrm{p,min}\right)^n}{\left(\alpha_\mathrm{p,max}-\alpha_\mathrm{p}\right)^p}, \tag{A.30}$$

where Fr, n and p are empirical material constants and $\alpha_\mathrm{p} > \alpha_\mathrm{p,min}$. The volume fraction at where frictionla stresses become significant is denoted by $\alpha_\mathrm{p,min}$ and in this study this value chosen $\alpha_\mathrm{p,min} = 0.01$, meaning frictional stresses are assumed negligible for dilute particle flow.

A.A.4 Generation and dissipation of granular energy

The mathematical expression for generation and dissipation of granular energy, λ_p, by Lun et al. (1984) is given as

$$\lambda_\mathrm{p} = 12\left(1-e^2\right)\frac{\alpha_\mathrm{p}\rho_\mathrm{p} g_0}{d_\mathrm{p}\sqrt{\pi}}\Theta^{3/2}. \tag{A.31}$$

A.A.5 Particle shear viscosity

The mathematical expression for particle shear viscosity, μ_p of Hrenya and Sinclair (1997) is given by

$$\mu_\mathrm{p} = \frac{5\sqrt{\pi\Theta}}{96}\rho_\mathrm{p} d_\mathrm{p}\left[\left(\frac{1}{\eta g_0}+\frac{8\alpha_\mathrm{p}}{5}\right)\left(\frac{1+\frac{8}{5}\eta(3\eta-2)\alpha_\mathrm{p} g_0}{2-\eta}\right)+\frac{768}{25\pi}\eta\alpha_p^2 g_0\right]. \tag{A.32}$$

A.A.6 Particle phase pressure

The solid-phase pressure, P_p, represents the normal forces due to particle-particle collisions. The mathematical formulation of Lun et al. (1984) is given as

$$P_p = \rho_p \alpha_p \Theta \left[1 + 2\,(1 + e)\, g_0 \alpha_p\right] . \tag{A.33}$$

References

Y. Adachi, M. A. Cohen Stuart, and R. Fokkink. Kinetics of Turbulent Coagulation Studied by Means of End-over-End Rotation. *Journal of Colloid and Interface Science*, 165(2):310–317, 7 1994. ISSN 0021-9797. doi: 10.1006/JCIS.1994.1234.

Janarjan Bhandari, Swarup China, Kamal Kant Chandrakar, Greg Kinney, Will Cantrell, Raymond A. Shaw, Lynn R. Mazzoleni, Giulia Girotto, Noopur Sharma, Kyle Gorkowski, Stefania Gilardoni, Stefano Decesari, Maria Cristina Facchini, Nicola Zanca, Giulia Pavese, Francesco Esposito, Manvendra K. Dubey, Allison C. Aiken, Rajan K. Chakrabarty, Hans Moosmüller, Timothy B. Onasch, Rahul A. Zaveri, Barbara V. Scarnato, Paulo Fialho, and Claudio Mazzoleni. Extensive Soot Compaction by Cloud Processing from Laboratory and Field Observations. *Scientific Reports 2019 9:1*, 9(1):1–12, 8 2019. ISSN 2045-2322. doi: 10.1038/s41598-019-48143-y.

John Bratby. *Coagulation and flocculation in water and wastewater treatment*. IWA Publishing, 2016. ISBN 9781843391067. doi: 10.2166/9781780407500.

J. Bridgeman, B. Jefferson, and S.A. A. Parsons. The development and application of CFD models for water treatment flocculators. *Advances in Engineering Software*, 41(1): 99–109, 1 2010. ISSN 09659978. doi: 10.1016/J.ADVENGSOFT.2008.12.007.

A. D. Burns, Thomas Frank, Ian Hamill, and J. M. Shi. The Favre averaged drag model for turbulent dispersion in Eulerian multi-phase flows. *5th International Conference on Multiphase Flow*, 4(392):1–17, 2004.

Lingling Cai, Zhiqiang Liu, Sha Mi, Chun Luo, Kebo Ma, Aixiang Xu, and Sheng Yang. Investigation on flow characteristics of ice slurry in horizontal 90° elbow pipe by a CFD-PBM coupled model. *Advanced Powder Technology journal*, 30:2299–2310, 2019. doi: 10.1016/j.apt.2019.07.010.

Thomas R. Camp and Philip C. Stein. Velocity Gradients and Internal Work in Fluid Motion. *Journal of Boston Society of Civil Engineering*, 30:219–237, 1943.

J David Griffith and Robert G Williams. Application of Jar-Test Analysis at Phoenix, Ariz. *Journal (American Water Works Association)*, 64(12):825–830, 1972.

Farzad F. Dizaji, Jeffrey S. Marshall, and John R. Grant. Collision and breakup of fractal particle agglomerates in a shear flow. *Journal of Fluid Mechanics*, 862:592–623, 3 2019. ISSN 14697645. doi: 10.1017/jfm.2018.959.

Joel J Ducoste and Mark M Clark. Turbulence in flocculators: Comparison of measurements and CFD simulations. *AIChE Journal*, 45(2):432–436, 1999. doi: 10.1002/aic.690450222.

Andrew Escue and Jie Cui. Comparison of turbulence models in simulating swirling pipe flows. *Applied Mathematical Modelling*, 34(10):2840–2849, 10 2010. ISSN 0307-904X. doi: 10.1016/J.APM.2009.12.018.

Sashikumaar Ganesan. An operator-splitting Galerkin/SUPG finite element method for population balance equations : stability and convergence. *ESAIM: Mathematical Modelling and Numerical Analysis*, 46(6):1447–1465, 11 2012. ISSN 0764-583X. doi: 10.1051/M2AN/2012012.

Johannes Haarhoff and Jeremia J van der Walt. Towards optimal design parameters for around-the-end hydraulic flocculators. *Journal of Water Supply: Research and Technology-Aqua*, 50(3):149–160, 5 2001. ISSN 0003-7214. doi: 10.2166/aqua.2001.0014.

J. Hærvig, K. Sørensen, and T.J. J. Condra. Early stages of agglomeration of adhesive particles in fully-developed turbulent pipe flows. *International Journal of Multiphase Flow*, 106:254–267, 9 2018. ISSN 0301-9322. doi: 10.1016/J.IJMULTIPHASEFLOW.2018.04.017.

A. Hilgenstock and R. Ernst. Analysis of installation effects by means of computational fluid dynamics—CFD vs experiments? *Flow Measurement and Instrumentation*, 7(3-4):161–171, 9 1996. ISSN 0955-5986. doi: 10.1016/S0955-5986(97)88066-1.

Christine M. Hrenya and Jennifer L. Sinclair. Effects of particle-phase turbulence in gas-solid flows. *AIChE Journal*, 43(4):853–869, 4 1997. ISSN 1547-5905. doi: 10.1002/AIC.690430402.

Ricardo I Jeldres, Phillip D Fawell, and Brendan J Florio. Population balance modelling to describe the particle aggregation process: A review. *Powder Technology*, 326:190–207, 2017. doi: 10.1016/j.powtec.2017.12.033.

K. L. Johnson, K. Kendall, and A. D. Roberts. Surface energy and the contact of elastic solids. *Proceedings of the Royal Society of London Series A*, 324:301–313, 1971. doi: 10.1098/rspa.1971.0141.

P. C. Johnson and R. Jackson. Frictional–collisional constitutive relations for granular materials, with application to plane shearing. *Journal of Fluid Mechanics*, 176:67–93, 1987. ISSN 1469-7645. doi: 10.1017/S0022112087000570.

Jongtae Kim, Mohan Yadav, and Seungjin Kim. Characteristics of Secondary Flow Induced by 90-Degree Elbow in Turbulent Pipe Flow. *Engineering Applications of Computational Fluid Mechanics*, 8(2):229–239, 2014. ISSN 1994-2060. doi: 10.1080/19942060.2014.11015509.

Sanjeev Kumar and D. Ramkrishna. On the solution of population balance equations by discretization—I. A fixed pivot technique. *Chemical Engineering Science*, 51(8):1311–1332, 4 1996. ISSN 0009-2509. doi: 10.1016/0009-2509(96)88489-2.

K. A. Kusters. *The influence of turbulence on aggregation of small particles in agitated vessels*. PhD thesis, Technische Universiteit Eindhoven, 1991.

Marko Laakkonen, Pasi Moilanen, Ville Alopaeus, and Juhani Aittamaa. Modelling local bubble size distributions in agitated vessels. *Chemical Engineering Science*, 62(3): 721–740, 2 2007. ISSN 0009-2509. doi: 10.1016/J.CES.2006.10.006.

Chai Siah Lee, John Robinson, and Mei Fong Chong. A review on application of flocculants in wastewater treatment. *Process Safety and Environmental Protection*, 92 (6):489–508, 11 2014. ISSN 0957-5820. doi: 10.1016/J.PSEP.2014.04.010.

R. Lehnigk, W. Bainbridge, Y. Liao, D. Lucas, T. Niemi, J. Peltola, and F. Schlegel. An open-source population balance modeling framework for the simulation of polydisperse multiphase flows. *AIChE Journal*, page e17539, 12 2021. ISSN 1547-5905. doi: 10.1002/AIC.17539.

Dongyue Li, Zhengming Gao, Antonio Buffo, Wioletta Podgorska, and Daniele L. Marchisio. Droplet breakage and coalescence in liquid–liquid dispersions: Comparison of different kernels with EQMOM and QMOM. *AIChE Journal*, 63(6):2293–2311, 6 2017. ISSN 1547-5905. doi: 10.1002/AIC.15557.

J. Liu, M. Crapper, and G.L. McConnachie. An accurate approach to the design of channel hydraulic flocculators. *Water Research*, 38(4):875–886, 2 2004. ISSN 0043-1354. doi: 10.1016/J.WATRES.2003.10.014.

C. K. K. Lun and S. B. Savage. The effects of an impact velocity dependent coefficient of restitution on stresses developed by sheared granular materials. *Acta Mechanica 1986 63:1*, 63(1):15–44, 11 1986. ISSN 1619-6937. doi: 10.1007/BF01182538.

C. K. K. Lun, S. B. Savage, D. J. Jeffrey, and N. Chepurniy. Kinetic theories for granular flow: inelastic particles in Couette flow and slightly inelastic particles in a general flowfield. *Journal of Fluid Mechanics*, 140:223–256, 1984. ISSN 1469-7645. doi: 10.1017/S0022112084000586.

Xiaofei Ma, Christopher D Zangmeister, Julien Gigault, George W Mulholland, and Michael R Zachariah. Soot aggregate restructuring during water processing. *Journal of Aerosol Science*, 66:209–219, 2013. doi: 10.1016/j.jaerosci.2013.08.001.

Benoit B Mandelbrot. Self-Affine Fractals and Fractal Dimension. *Physica Scripta*, 32(4): 257, 10 1985. ISSN 1402-4896. doi: 10.1088/0031-8949/32/4/001.

Daniele L. Marchisio, R. Dennis Vigil, and Rodney O. Fox. Implementation of the quadrature method of moments in CFD codes for aggregation - breakage problems. *Chemical Engineering Science*, 58(15):3337–3351, 8 2003. ISSN 00092509. doi: 10.1016/S0009-2509(03)00211-2.

Elizabeth Marden Marshall and André Bakker. Computational Fluid Mixing. *Handbook of industrial mixing: science and practice*, pages 257–343, 2004.

R. Mei. An approximate expression for the shear lift force on a spherical particle at finite reynolds number. *International Journal of Multiphase Flow*, 18(1):145–147, 1 1992. ISSN 0301-9322. doi: 10.1016/0301-9322(92)90012-6.

V. A. Mhaisalkar, R. Paramasivam, and A. G. Bhole. Optimizing physical parameters of rapid mix design for coagulation-flocculation of turbid waters. *Water Research*, 25 (1):43–52, 1 1991. ISSN 0043-1354. doi: 10.1016/0043-1354(91)90097-A.

E. F. Mikhailov, S. S. Vlasenko, Igor A. Podgorny, V. Ramanathan, and C. E. Corrigan. Optical properties of soot–water drop agglomerates: An experimental study. *Journal of Geophysical Research: Atmospheres*, 111(D7):7209, 4 2006. ISSN 2156-2202. doi: 10.1029/2005JD006389.

Jun Nan, Meng Yao, Ting Chen, Zhenbei Wang, Qinggui Li, and Dan Zhan. Experimental and numerical characterization of floc morphology: role of changing hydraulic retention time under flocculation mechanisms. *Environmental Science and Pollution Research*, 23(4):3596–3608, 2 2016. ISSN 0944-1344. doi: 10.1007/s11356-015-5539-7.

St Palzer. Agglomeration of pharmaceutical, detergent, chemical and food powders — Similarities and differences of materials and processes. *Powder Technology*, 206(1-2): 2–17, 1 2011. ISSN 0032-5910. doi: 10.1016/J.POWTEC.2010.05.006.

A. Passalacqua, F. Laurent, E. Madadi-Kandjani, J. C. Heylmun, and R. O. Fox. An open-source quadrature-based population balance solver for OpenFOAM. *Chemical Engineering Science*, 176:306–318, 2 2018. ISSN 0009-2509. doi: 10.1016/J.CES.2017.10.043.

P. Saffman. The lift on a small sphere in a slow shear flow. *Journal of Fluid Mechanics1*, 22(2):385–400, 1965. doi: 10.1017/S0022112065000824.

Fabian Schlegel, Kasper Gram Bilde, Mazen Draw, Ilya Evdokimov, Susann Hänsch, Harris Khan, Ronald Lehnigk, Jiadong Li, Hongmei Lyu, Richard Meller, Gašper Petelin, and Matej Tekavčič. HZDR Multiphase Addon for OpenFOAM, 9 2022.

Lalita Kanwar Shekhawat, Jayati Sarkar, Rachit Gupta, Sandeep Hadpe, and Anurag S Rathore. Application of CFD in Bioprocessing: Separation of mammalian cells using disc stack centrifuge during production of biotherapeutics. *Journal of Biotechnology*, 267:1–11, 2 2018. ISSN 0168-1656. doi: 10.1016/J.JBIOTEC.2017.12.016.

Anders Schou Simonsen. *Modelling and Analysis of Seawater Scrubbers for Reducing SOx Emissions from Marine Engines*. PhD thesis, Aalborg University, Aalborg, 2018.

The OpenFOAM Foundation. OpenFOAM-dev, 2022.

Zhenbo Tong, Wenqi Zhong, Aibing Yu, Hak-Kim Chan, and Runyu Yang. CFD–DEM investigation of the effect of agglomerate–agglomerate collision on dry powder aerosolisation. *Journal of Aerosol Science*, 92:109–121, 2 2016. ISSN 0021-8502. doi: 10.1016/J.JAEROSCI.2015.11.005.

Una Trivanovic, Joel C Corbin, Alberto Baldelli, Weihan Peng, Jiacheng Yang, Patrick Kirchen, J Wayne Miller, Prem Lobo, Stéphanie Gagné, and Steven N Rogak. Size and morphology of soot produced by a dual-fuel marine engine. *Journal of Aerosol Science journal*, 138:105448, 2019. doi: 10.1016/j.jaerosci.2019.105448.

B.G.M. van Wachem. Derivation, Implementation, and Validation of Computer Simulation Models for Gas-Solid Fluidized Beds, 2000.

Lasse Vrale and Roger M Jorden. RAPID MIXING IN WATER TREATMENT. *Journal (American Water Works Association)*, 63(1):52–58, 1971.

Xiaochen Wang, Ying Wang, Yuanqi Bai, Peng Wang, and Yuwei Zhao. An overview of physical and chemical features of diesel exhaust particles. *Journal of the Energy Institute*, 92:1864–1888, 2018a. doi: 10.1016/j.joei.2018.11.006.

Zhenbei Wang, Jun Nan, Xiaoyu Ji, and Yueming Yang. Effect of the micro-flocculation stage on the flocculation/sedimentation process: The role of shear rate. *Science of The Total Environment*, 633:1183–1191, 8 2018b. ISSN 0048-9697. doi: 10.1016/J.SCITOTENV.2018.03.286.

C.Y. Wen and Y.H. Yu. Mechanics of Fluidization. *The Chemical Engineering Progress Symposium Series*, 162:100–111, 1966.

V. Yakhot, S. A. Orszag, S. Thangam, T. B. Gatski, and C. G. Speziale. Development of turbulence models for shear flows by a double expansion technique. *Physics of Fluids A*, 4(7):1510–1520, 1992. ISSN 08998213. doi: 10.1063/1.858424.

Victor Yakhot and Steven A. Orszag. Renormalization group analysis of turbulence. I. Basic theory. *Journal of Scientific Computing 1986 1:1*, 1(1):3–51, 3 1986. ISSN 1573-7691. doi: 10.1007/BF01061452.

Ya Yao, Jun-Wei Wei Su, and Zheng-Hong Hong Luo. CFD-PBM modeling polydisperse polymerization FBRs with simultaneous particle growth and aggregation: The effect of the method of moments. *Powder Technology*, 272:142–152, 3 2015. ISSN 0032-5910. doi: https://doi.org/10.1016/j.powtec.2014.11.037.

C. Yuan, F. Laurent, and R. O. Fox. An extended quadrature method of moments for population balance equations. *Journal of Aerosol Science*, 51:1–23, 9 2012. ISSN 0021-8502. doi: 10.1016/J.JAEROSCI.2012.04.003.

Zhengjie Zhu, Carlos A. Dorao, D. Lucas, and Hugo A. Jakobsen. On the Coupled Solution of a Combined Population Balance Model Using the Least-Squares Spectral Element Method. *Industrial and Engineering Chemistry Research*, 48(17):7994–8006, 9 2009. ISSN 08885885. doi: 10.1021/IE900088Q.

Paper B

Decay of secondary motion downstream bends in turbulent pipe flows

Kasper Gram Bilde, Kim Sørensen, Jakob Hærvig

The paper has been published in the
AIP Physics of Fluids Vol. 35, pp. 015102, 2023.

Decay of secondary motion downstream bends in turbulent pipe flows

Kasper Gram Bilde*,[1], Kim Sørensen[1], Jakob Hærvig[1]

* *Corresponding author*
[1] *Aalborg University, Department of Energy, Pontoppidanstræde 111, 9220 Aalborg, Denmark*

Keywords: *Dean vortices; Fully developed flow; Turbulence; Secondary Motion; Large eddy simulation*

Abstract

Decay of secondary motion downstream 180° pipe bends are investigated using Large Eddy Simulations (LES) for bend radii of $1 \leq r_B/d_h \leq 3.375$ *at a Reynolds number of* $\mathrm{Re}_h = 10,000$. *The velocity and turbulence characteristics are validated against experimental data for a straight pipe section as well as against experimental- and DNS data for a 90° pipe bend. As the bend radius decreases, a larger magnitude of turbulence intensity is induced immediately downstream of the bend and for the largest magnitude, the highest gradient of the decay turbulence intensity is observed. As a result, the recovery length needed to re-establish the velocity profile downstream of the pipe bend decreases. Turbulence is transported at a higher rate, indicating that the recovery of the velocity profile is driven by turbulence transport. Secondary motions are induced by the curvature of the pipe bend and as the bend radius decreases, the magnitude of the secondary motion increases. The results show how the secondary motion decay in magnitude as the flow moves downstream the pipe bend. At the outlet of the bend, secondary motions are dominating at the walls and in the bulk flow. As the fluid moves further downstream, the secondary flows dominate close to the walls and at a length of* $x/d_h = 5$, *a negligible difference in secondary motion is observed for the different bend radii.*

B.1 Introduction

Transport of fluids in circular pipes is a part of most engineering applications and most often the fluid flow is in the turbulent regime. These applications include heat exchangers, chemical reactors, mixing devices and piping to and from various applications. For practical reasons the piping layout of the applications often includes both 90° and 180° pipe bends, where swirl, secondary motions and turbulence are induced downstream, which causes additional pressure losses and distorts the velocity profile (Kim et al., 2014). The characteristics of turbulence and secondary motions downstream of a bend are important parameters for various applications when, e.g., measuring the volumetric flow rate using an electromagnetic flowmeter. The distorted velocity profile, due to the pipe bend, may result in both systematic and random errors (Salustiano Martim et al., 2019).

Rowe (1970) was among the first to study the total pressure distribution throughout a 180° pipe bend and analysed the downstream effect of the pipe bend. Experimental measurements were performed on a 180° circular pipe bend with a bend radius of $r_B = 12d_h$ and Reynolds number of $Re_h = 23,600$. Secondary flow patterns induced by a pipe bend were some of the main findings and it was concluded that the secondary flow was most intense at an angle of about 30° through the pipe.

Azzola et al. (1986) extended the experimental work by measuring the longitudinal and azimuthal velocity components using laser Doppler velocimetry (LDV) for a 180° pipe bend with a bend radius of $r_B = 3.375d_h$ for Reynolds numbers of $Re_h = 57,400$ and $Re_h = 110,000$. Numerical results of the turbulence characteristics over the pipe bend were compared to the presented experimental results and the Reynolds stress tensor was modelled using the standard k-ε turbulence model (Launder and Spalding, 1974). It was reported that the numerical- and experimental results were in good agreement along the curvature of the pipe bend, but that the downstream results from the numerical model deviated from the experimental data.

Sudo et al. (2001) measured the velocity components in a 180° pipe bend with a bend radius of $r_B = 4d_h$ for a Reynolds number of $Re_h = 60,000$ using hot-wires in a similar setup to Sudo et al. (1998), who investigated the velocity profile through a 90° bend. It was reported that a recovery length of $x/d_h = 10$ was required to recover the symmetrical velocity profile for a 90° bend with a bend radius of $r_B = 4d_h$. Analysing the experimental results for the 180° pipe bend, it was concluded that the recovery length is longer for a 180° bend when compared to the 90° with similar inlet boundary conditions.

To achieve a better understanding of the downstream induced flow structures, Hellström et al. (2013) used time-resolved stereoscopic particle image velocimetry (PIV). The experimental results were obtained for a 90° pipe bend for Reynolds numbers of $Re_h = 20,000$ and $Re_h = 115,000$. It is reported that the recovery of the profiles appears to be driven by turbulent transport, which is expected to be more significant at higher Reynolds numbers.

Di Liberto et al. (2013) simulated the turbulent flow through a pipe with three bend radii, $r_B = 1.67d_h$, $r_B = 5d_h$ and $r_B = \infty$ (straight pipe), using direct numerical simulations (DNS). The authors simulated the flow with a constant friction Reynolds number of $Re_\tau = 500$, resulting in Reynolds numbers of $Re_h = 17,000$, $Re_h = 15,000$ and $Re_h = 12,000$ respectively. The domain was meshed using periodic boundary conditions, effectively giving an infinitely long curved pipe. The velocity profile within the pipe bend was reported with high accuracy as the smallest scale turbulence was resolved, but as an infinitely long pipe was simulated, the downstream effect was not in the scope of the study.

Röhrig et al. (2015) studied the characteristics of a turbulent flow through a 90° pipe bend at Reynolds numbers between $14,000 \leq Re_h \leq 34,000$ using both a RANS model and a large-eddy simulation (LES) to resolve and model the turbulence in the flow. The LES model successfully captured the time-averaged velocity profile, secondary motions and turbulence structures, whereas the RANS model generally underpredicted the velocity at the walls. The higher accuracy of the LES model comes at a higher computational cost when compared to the RANS model.

More recently, Gotfredsen et al. (2020) measured the velocity profile and concen-

tration profile of a tracer gas downstream of a 90° pipe bend using LDV. Numerical results of two different Reynolds averaged Navier-Stokes (RANS) using the k-ω SST and the k-ε turbulence models as well as results from a detached eddy simulation (DES) were compared to the experimental results. It was concluded that the k-ω SST model had difficulties when predicting the turbulence downstream and that the k-ε model produced better results except for the inlet of the 90° pipe bend. The DES model was successful in predicting the flow profile and turbulence up and downstream from the pipe bend.

In this study, the downstream flow characteristics of a 180° pipe bend are studied to evaluate the secondary motions, velocity fluctuations and turbulence induced by the bend. The time-averaged velocity profile and the recovery of this are also analysed in the present study to understand the recovery length needed to re-establish the velocity profile. The flow in the pipe is simulated for a Reynolds number of $\mathrm{Re_h} = 10,000$ using LES to resolve the velocity fluctuations. To analyse the effect of the bend radius of the 180° pipe bend, the flow characteristics are analysed for bend radii bounded by $d_\mathrm{h} \leq r_\mathrm{B} \leq 3.375 d_\mathrm{h}$.

B.2 Details on numerical setup

B.2.1 Geometrical configuration

The computational domain is seen in Fig. B.1, where the bend radius of the pipe bend is denoted by $r_\mathrm{B} = k\, d_\mathrm{h}$. Upstream of the 180° bend, a pipe with a length of $x = 10 d_\mathrm{h}$, is seen to make sure that a fully-developed turbulent velocity profile enters the pipe bend. Downstream from the bend, another straight pipe section of $x = 10 d_\mathrm{h}$ is applied to analyse the downstream turbulent properties of the fluid flow.

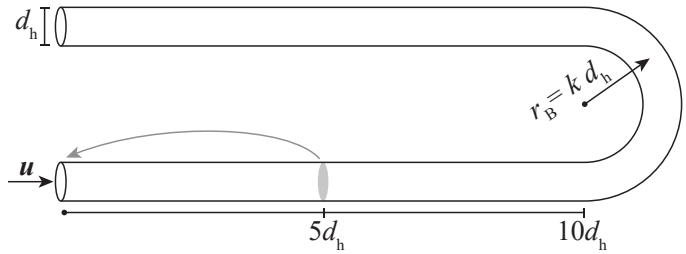

Fig. B.1: Representation of the geometrical configuration with a bend radius of $r_\mathrm{B} = k\, d_\mathrm{h}$. The inlet velocity profile is mapped at $x = 5 d_\mathrm{h}$ downstream and reapplied at the inlet.

B.2.2 Governing equations for the fluid flow

The filtered LES equations applied in this study are valid for an unsteady, incompressible, three-dimensional viscous flow and the continuity- and momentum equations are given by Eq. (B.1) and (B.2), respectively, as

$$\nabla \cdot \overline{\boldsymbol{u}} = 0\,, \tag{B.1}$$

$$\frac{\partial \overline{\boldsymbol{u}}}{\partial t} + \nabla \cdot (\overline{\boldsymbol{u}}\overline{\boldsymbol{u}}) = -\frac{1}{\rho}\nabla \overline{p} + \nabla \left(\left(\nu + \nu_{\text{sgs}} \right) \nabla \cdot \overline{\boldsymbol{u}} \right) , \tag{B.2}$$

where $\overline{\boldsymbol{u}}$ is the filtered velocity, $\overline{p}$ is the filtered pressure, ν is the fluid viscosity and ν_{sgs} is the sub-grid scale turbulent viscosity. A pressure correction term is applied to the inlet boundary condition to balance the mean fluid velocity, as the velocity profile at the inlet is re-applied from a distance of $x = 5d_{\text{h}}$ downstream from the inlet which is further described in section B.2.5 and illustrated in Fig. B.1.

The governing equations are discretised using the finite volume method and time advancements are performed using an implicit, second-order accurate scheme where a maximum Courant–Friedrichs–Lewy (CFL) condition of CFL $= \Delta x / (|\overline{\boldsymbol{u}}| \, \Delta t) < 1$ is restraining the time step advancements. All spatial terms are discretised using second-order accurate schemes to reduce numerical damping of the velocity fluctuations. The coupling of the pressure and velocity fields is performed using the PISO algorithm proposed by Issa (1986). All simulations in this study are carried out using the open-source CFD library OpenFOAM.

B.2.3 Sub-grid scale turbulence modelling

The sub-grid scale (SGS) turbulent viscosity, ν_{sgs}, is modelled using the wall-adapting local eddy-viscosity (WALE) model, proposed by Nicoud and Ducros (1999), to account for the sub-grid scale eddy dissipation. The SGS model is given as

$$\nu_{\text{sgs}} = \left(C_W V^{1/3} \right)^2 \frac{\left(\overline{s}_{ij}^d \overline{s}_{ij}^d \right)^{3/2}}{\left(\overline{s}_{ij} \overline{s}_{ij} \right)^{5/2} + \left(\overline{s}_{ij}^d \overline{s}_{ij}^d \right)^{5/4}} . \tag{B.3}$$

Herein, V is the volume of the local control volume and $C_W = 0.325$. The traceless symmetric part of the square of the velocity gradient tensor is defined as

$$\overline{s}_{ij}^d = \frac{1}{2} \left(\overline{g}_{ij}^2 + \overline{g}_{ji}^2 \right) - \frac{1}{3} \delta_{ij} \overline{g}_{kk}^2 , \tag{B.4}$$

where δ_{ij} is the Kronecker delta, $\overline{s}_{ij}$ is the strain-rate tensor and the $\overline{g}_{ij}$ is the velocity gradient defined as $\overline{g}_{ij} = \partial \overline{u}_i / \partial x_j$.

When comparing the WALE model to the traditional Smagorinsky-type SGS turbulence models, the WALE model is well-suited for wall-bounded flows such as a pipe flow, as the SGS viscosity automatically goes to zero at the wall, resulting in no damping functions or dynamic constant adjustments to correct for the wall.

B.2.4 Computational domain

To resolve the largest turbulent eddies within the flow field, a fine computational mesh is required. The first cell height, contacting the wall surface, is placed at $y^+ = \Delta y u_\tau / \nu = 1$ for all applied meshes to accurately resolve the viscous sub-layer part of the boundary layer. The frictional velocity, u_τ, denotes the velocity at the wall. The largest cell height, Δy_{max}, is placed in the centre of the pipe, as seen in the cross-sectional view of the pipe in Fig. B.2, where a quarter of the cross-sectional view of the computational mesh

is seen. The mesh is constructed with a maximum angle of 120° between each cell to ensure a high grid quality.

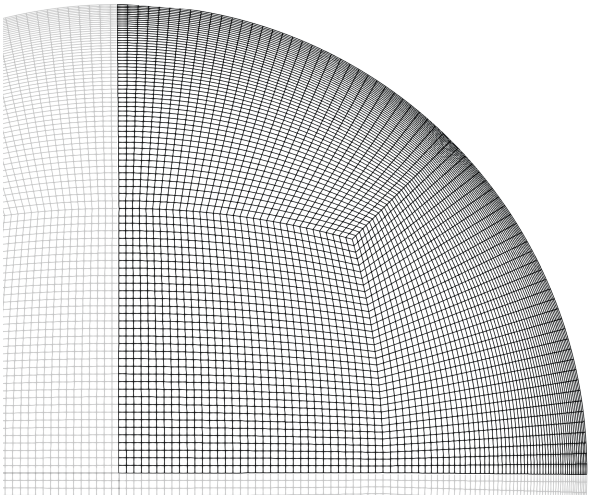

Fig. B.2: Cross-sectional view of a quarter of the round pipe mesh.

For the different simulations carried out in the present study, the total number of computational cells varies between $29.7 \cdot 10^6$ and $38.7 \cdot 10^6$ depending on the bend radius. Simulations are carried out using a single HB120rs_v3 in Microsoft Azure which is configured with 120 vCPUs of AMD EPYC 7V73X and 448 GB of RAM. Simulation time using all available vCPUs is in the order of 40 hours per simulation.

B.2.5 Boundary conditions

A fully-developed turbulent velocity profile is applied to the inlet of the domain by re-applying the 3-dimensional velocity field at a distance of $x = 5d_\mathrm{h}$ downstream of the inlet, which is also illustrated in Fig. B.1. The instantaneous velocity of the downstream patch is re-applied to the inlet boundary at the next time advancement and the pressure is corrected to ensure a mean velocity corresponding to the specified Reynolds number. This effectively creates an infinitely long straight upstream of the pipe bend with the sole purpose of creating a fully-developed turbulent velocity profile. To make sure no spatial correlations exist in the flow field from the inlet to the mapping plane, Robinson (1991) suggests turbulence structures in pipe flow to extend $L_x^+ = 1000$ in viscous units while Hærvig et al. (2018) used a computational domain of length $L_x^+ = 2500$ (corresponding to $L/d_\mathrm{h} = 4$) for a pipe flow with $\mathrm{Re}_\mathrm{h} = 10,000$. The velocity field is therefore updated each time step to account for both spatial and temporal changes in the velocity profile. Uniform pressure is applied at the outlet of the domain and the *no-slip* velocity condition is applied to all walls.

B.2.6 Validation

The near-wall velocity profile of the straight pipe section is compared to experimental results obtained by Toonder and Nieuwstadt (1997) for a straight pipe section. The velocity, normalised by the friction velocity $u_\tau = \sqrt{\tau/\rho}$, is evaluated downstream at a length of $x = 5d_\mathrm{h}$ relative to the inlet, which is also where the instantaneous velocity is re-applied to the inlet at every time advancement.

The numerical results obtained for three different mesh densities are compared to the experimental values of Toonder and Nieuwstadt (1997) in Fig. B.3 and B.4. The absolute and RMS velocities are normalised using the frictional velocity, u_τ, for the straight section of the pipe and it is found that the LES data is in good agreement with both the experimental data and also the theoretical law of the wall (Von Kármán, 1930). The finest mesh is in good agreement with both the streamwise velocity and the axial RMS velocity, however, it overpredicts the radial RMS velocity close to the wall, as seen in Fig. B.4b. The LES model is in good agreement with the radial RMS velocity when the flow moves further away from the wall. As the finest mesh is in good agreement with the experimental data and this grid density is chosen as the mesh size for the following results presented in this study.

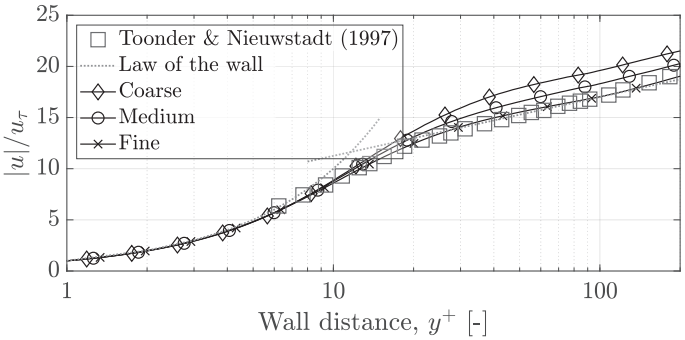

Fig. B.3: Normalised velocity, $|\boldsymbol{u}|/u_\tau$, as functions of the dimensionless boundary layer, distances to the wall y^+ for the straight pipe flow compared to experimental results obtained by Toonder and Nieuwstadt (1997) Toonder and Nieuwstadt (1997) and to the law of the wall (viscous sub-layer $u^+ = y^+$ and log-law layer $u^+ = 2.5 \cdot \ln(y^+) + 5.5$).

For validation purposes only, simulations through a 90° bend at $\mathrm{Re_d} = 5300$ and $\mathrm{Re_d} = 14000$ is carried out using the LES model and the results are compared against DNS data by Wang et al. (2018) as well as experimentally obtained data using combined Particle Image Velocimetry (PIV) and Hot-Wire (HW) by Sattarzadeh (2011) and Kalpakli Vester et al. (2016). The DNS data of Wang et al. (2018) is obtained for a 90° bend of $r_\mathrm{B} = 1.25d_\mathrm{h}$ for a fluid flow of $\mathrm{Re_d} = 5300$. The normalised velocity profile is in good agreement with the DNS data, as shown in Fig. B.5a. The PIV-HW data of both Sattarzadeh (2011) and Kalpakli Vester et al. (2016) is obtained for a 90° bend of $r_\mathrm{B} = 1.58d_\mathrm{h}$ at a flow of $\mathrm{Re_d} = 14000$. Sattarzadeh (2011) reports the data at a downstream length of $x/d_\mathrm{h} = 1.5$ whereas Kalpakli Vester et al. (2016) report the data at a downstream length of $x/d_\mathrm{h} = 0.67$. The normalised streamwise velocity profile is in good agreement with the experimental data at both locations, as shown in Fig. B.5b

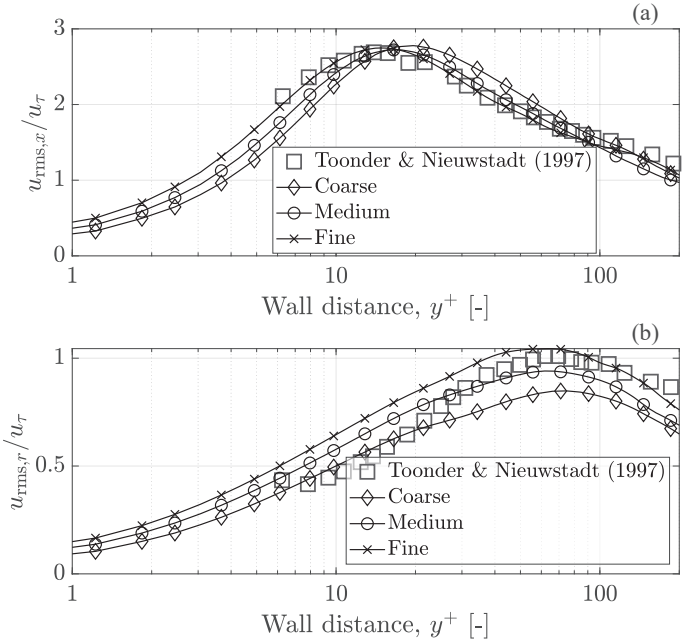

Fig. B.4: Normalised RMS velocity for the three mesh densities compared to experimental data of Toonder and Niuewstadt (1997)Toonder and Nieuwstadt (1997) for the straight pipe section. The normalised axial RMS velocity, $u_{\mathrm{rms},x}/u_\tau$, is shown in Fig. B.4a and the normalised radial RMS velocity, $u_{\mathrm{rms},r}/u_\tau$, is shown in Fig. B.4b.

and B.5c.

Sattarzadeh (2011) and Kalpakli Vester et al. (2016) report the turbulence intensity downstream of the 90° bend and the results at the downstream location of $x/d_\mathrm{h} = 1.5$ is seen in Fig. B.6a and at a downstream location of $x/d_\mathrm{h} = 0.67$ in Fig. B.6b. It is observed that the LES model overpredicts the turbulence intensity slightly at the inner radius, $r_\mathrm{B} < 0$, however, the data is in good agreement with the experimental data. The turbulence intensity measured at the outer radius is in very good agreement with the experimental data.

Comparing the LES results to the experimental results for the straight pipe section in Fig. B.3 and to the DNS and experimental data for a 90° pipe bend, it is shown that the LES model produces results that are in good agreement with both experimental and DNS data.

B.3 Results and Discussion

Five simulations are performed at $\mathrm{Re}_\mathrm{h} = 10,000$ with bend radii in the range of $d_\mathrm{h} \leq r_\mathrm{B} \leq 3.375 d_\mathrm{h}$. The number of computational cells applied in the computational domain is dependent on the bend radius, as the total length of the domain increases as the bend radius increases. A total of 29.7 million computational cells are applied for the smallest

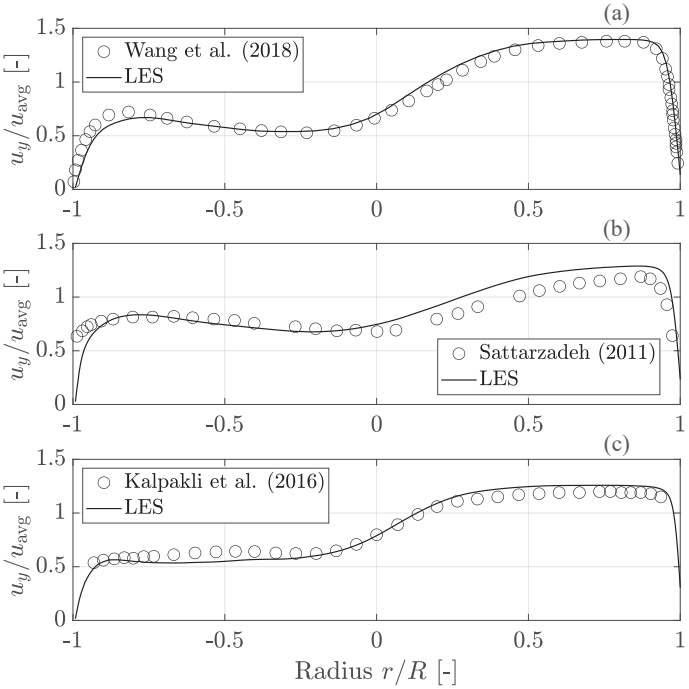

Fig. B.5: The normalised streamwise velocity, u_y/u_{avg}, for a pipe with a 90° bend. The streamwise velocity for $\mathrm{Re_d} = 5300$ and $r_\mathrm{B} = 1.25d_\mathrm{h}$ are compared to the DNS data of Wang et al. (2018) in Fig. B.5a. The streamwise velocity for $\mathrm{Re_d} = 14000$ and $r_\mathrm{B} = 1.58d_\mathrm{h}$ is compared to PIV-HW data of Sattarzadeh (2011) Sattarzadeh (2011) and Kalpakli et al. (2016) Kalpakli Vester et al. (2016) measured at a downstream length of $x/d_\mathrm{h} = 1.5$ in Fig. B.5b and at a downstream length of $x/d_\mathrm{h} = 0.67$ in Fig. B.5c.

bend radius, $r_\mathrm{B} = d_\mathrm{h}$, and a total of 38.7 million computational cells are applied for the largest bend radius, $r_\mathrm{B} = 3.375d_\mathrm{h}$.

B.3.1 Instantaneous velocity fields

Instantaneous velocity contours of the cross section after the pipe bend are seen in Fig. B.8, where the magnitude of the velocity is scaled by the bulk velocity of the flow. The contours are shown at a length of $0 \leq x \leq 4d_\mathrm{h}$ downstream of the 180° bend to highlight the instantaneous velocity profile and the turbulence induced by the curvature of the bend. It immediately indicates that the smallest bend radius, $r_\mathrm{B} = d_\mathrm{h}$ induces the largest magnitude of velocity fluctuations, as this contour has the largest magnitude of velocity. As the bend radius increases, it is seen how the velocity fluctuations decrease in magnitude and that the majority of the mass flow rate is located at the top half of the pipe. As the fluid moves downstream for the pipe, it is indicated that the velocity profile starts to recover, as the contours take a more homogeneous colour at $x = 4d_\mathrm{h}$ for all configurations when compared to $x = 0$.

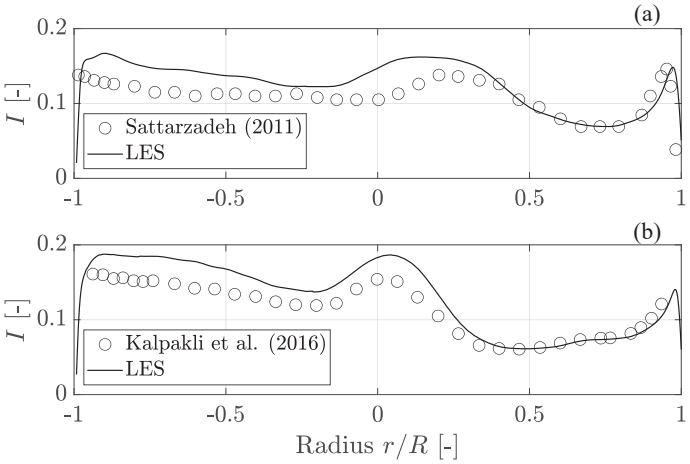

Fig. B.6: Turbulence intensity for a 90° bend with a fluid flow of Re = 14000 measured at a downstream location of x/d_h = 1.5 in Fig. B.6a and x/d_h = 0.67 in Fig. B.6b

B.3.2 Time-averaged velocity profiles

The instantaneous velocity contours provide insight into the velocity fluctuations in a very brief time period, which is why the time-averaged velocity profile provides a better understanding of the flow phenomena taking place downstream of the bend. The normalised time-averaged velocity, $\langle \boldsymbol{u} \rangle / u_{avg}$, is evaluated in the same cross-sectional planes as the instantaneous contours in Fig. B.8 and the contours are shown in Fig. B.7. The time-averaged velocity shows that a low-velocity zone is observed at the bottom of the pipe immediately after the bend, $x = 0$, for all bend radii. The low-velocity area is the largest for the smallest bend radius, $r_B = d_h$, which is due to the fluid streamlines slipping the wall due to the large curvature of the bend. The secondary flow streamlines are also visualised in Fig. B.7 and it is observed for all cases that Dean vortices are induced by the pipe bend, which is also reported by other researchers (Dean, 1928; Anwer et al., 1989; Kalpakli and Örlü, 2013). The secondary flow profile is further described in section B.3.3.

The time-averaged velocity profiles are evaluated in intervals of $\theta = 45°$ between $0° \leq \theta \leq 180°$ throughout the 180° bend for the different bend radii and shown in Fig. B.9. The inner radius of the pipe is denoted with $r/R = -1$ and the outer radius of the pipe is denoted with $r/R = 1$. It is seen that the velocity profile is skewed at the inlet of the pipe bend for the simulations with the smallest bend radius, $d_h \leq r_B \leq 1.5 d_h$. The velocity profile continues to become more skewed throughout the bend and the biggest difference between the velocity profiles is observed at an angle of $\theta = 45°$ through the bend. When the flow leaves the bend at an angle of $\theta = 180°$, there is only a small difference between the normalised velocity profiles produced by the different bend radii.

The streamwise velocity for the symmetrical plane from the outlet of the pipe bend to the outlet of the computational domain is plotted in Fig. B.10 to analyse the skewness and the recovery of the velocity profile downstream of the pipe bend. The

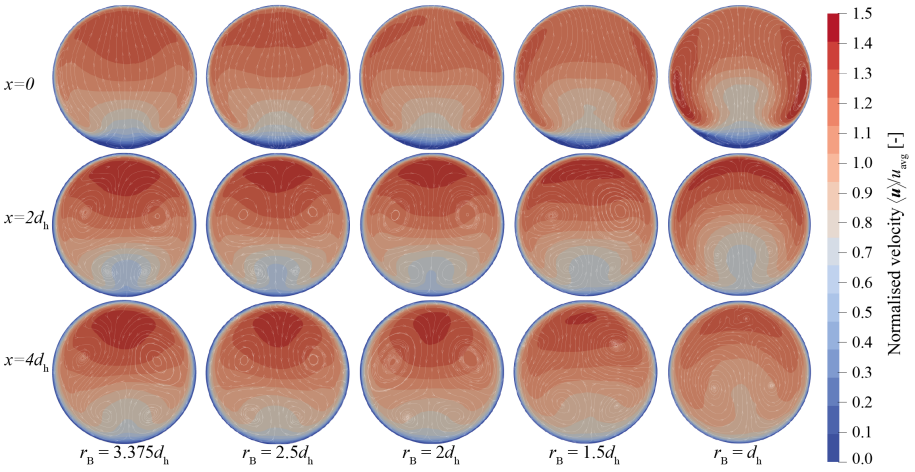

Fig. B.7: Normalised velocity, $\langle \boldsymbol{u} \rangle / u_{\text{avg}}$, at lengths of $x = 0$, $x = 2d_{\text{h}}$ and $x = 4d_{\text{h}}$ downstream of the bend for different bend radii. The secondary flows are visualised as streamlines.

velocity profile is normalised using the bulk velocity and plotted at a length of $x/d_{\text{h}} = 0$, $x/d_{\text{h}} = 2$, $x/d_{\text{h}} = 4$, $x/d_{\text{h}} = 6$ and $x/d_{\text{h}} = 8$ in Fig. B.10a to B.10e, respectively. It is observed that the skewed velocity profile that exits the pipe bend, as seen in Fig. B.9 at an angle of $\theta = 180°$, becomes even more skewed at a length of $x = d_{\text{h}}$ downstream from the bend, in Fig. B.10a. The velocity profile for the smallest bend radius is the most skewed velocity profile at this location. When the fluid moves further downstream from the bend, the velocity profile starts to recover and at the outlet of the domain, seen in Fig. B.10e, the most skewed velocity profile is observed for the simulation with the largest bend radius, $r_{\text{B}} = 3.375d_{\text{h}}$.

To quantify the skewness of the velocity profile over the cross-section of the pipe, the uniformity index, φ, of the velocity profile is evaluated, where the uniformity index is given by

$$\varphi = 1 - \frac{1}{2Au_{\text{avg}}} \int \left| \langle \boldsymbol{u} \rangle - u_{\text{avg}} \right| \mathrm{d}A \,. \tag{B.5}$$

A uniformity index of $\varphi = 1$ equals a plug flow where the same velocity is applied in all cells along the cross-section of the pipe. The evolution of the uniformity index of the time-averaged velocity downstream of the pipe bends is shown in Fig. B.11.

A relatively high uniformity index is observed at the outlet of the bend, $x = 0$ for all simulations. After a length of $x = d_{\text{h}}$, a drop is observed for all bend radii and this is where the flow experiences the lowest uniformity index. This is due to the fluid slipping the wall at the outlet as it cannot stay attached to the wall. Comparing the velocity profiles at the outlet of the bend in Fig. B.9 and at a distance of $x = d_{\text{h}}$ in Fig. B.10 show that a lower velocity occurs in the bottom part of the pipe due to the fluid flow not staying attached to the wall, causing the uniformity index to decrease in value. As the fluid moves further downstream from the bend, an increasing value for the uniformity index is observed, which is also qualitatively observed in Fig. B.10. It is noteworthy to mention that the uniformity index for the simulation with the smallest

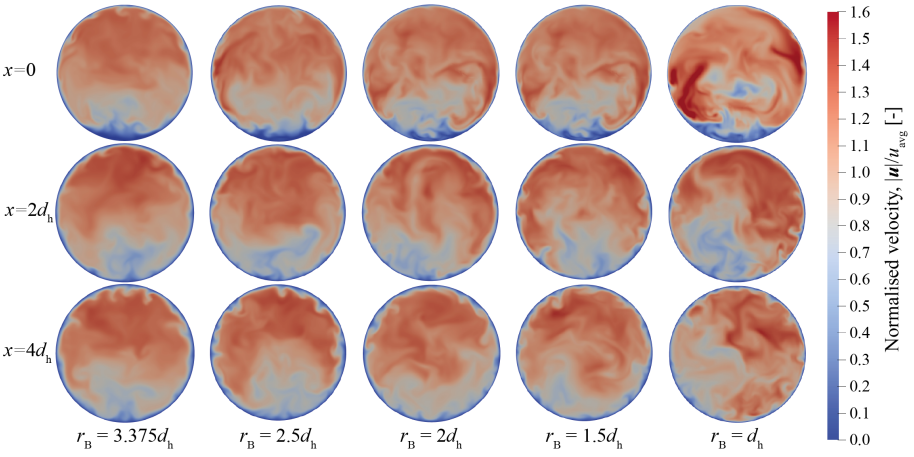

Fig. B.8: Cross-sectional instantaneous normalised velocity contours for all bend radii at lengths of $x = 0$, $x = 2d_\mathrm{h}$, $x = 4d_\mathrm{h}$ downstream the 180° bend.

bend radius reaches the overall lowest uniformity index of $\varphi = 0.87$ but increases in uniformity faster compared to the other configurations. In general, it is observed that the uniformity index increases faster when the bend radius decreases and the lowest uniformity index at $x = 10d_\mathrm{h}$ are observed for the largest bend radius.

B.3.3 Decay of secondary motion

The secondary motion, also seen as flow streamlines in Fig. B.7, is further analysed to study how the secondary flow decays as the flow moves downstream from the pipe bend. The secondary velocity is normalised using the bulk velocity as $(|u_y| + |u_z|)/u_\mathrm{avg}$ and the secondary velocities are shown in Fig. B.13 for the different bend radii. The secondary flow is largest in magnitude as the flow leaves the 180° bend which is seen in Fig. B.13a. At this location, it is observed that the simulations for bend radii in the range of $d_\mathrm{h} \leq r_\mathrm{B} \leq 2.5d_\mathrm{h}$ have two peaks which are at magnitudes of the same order. The first peak is observed closer to the wall, where a large secondary flow is present and a second peak is observed when moving towards the centre of the pipe.

When the fluid has moved a length of $x = d_\mathrm{h}$ downstream of the bend, it is observed that the secondary flow has decreased significantly in magnitude, as seen in Fig. B.13b. The secondary flow is now largest in magnitude close to the wall for all bend radii and the simulation with the smallest bend radii has the largest magnitude of secondary flow. This is the case until a length of $x = 4d_\mathrm{h}$ downstream of the bend, seen in Fig. B.13e, is reached, where it is observed that the secondary flow is still largest in magnitude for the smallest bend radius, but that the secondary flow is at a magnitude with small difference between the simulations.

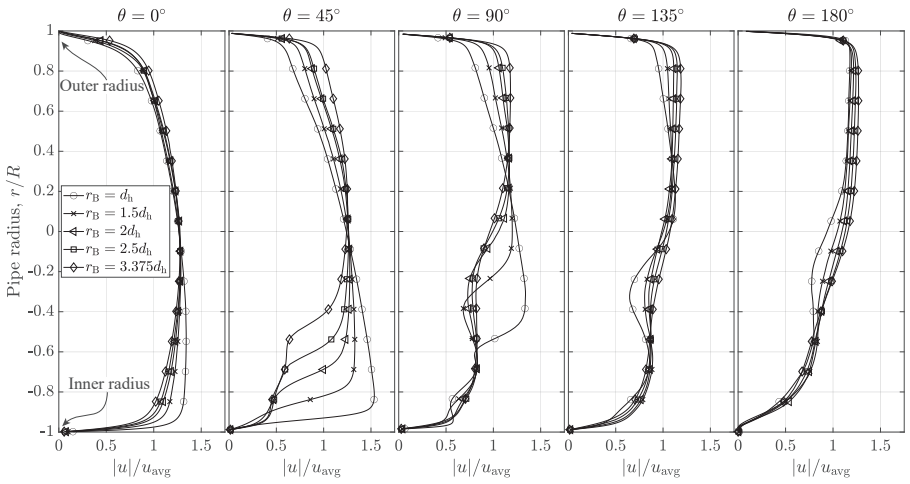

Fig. B.9: Normalised velocity profile $|\boldsymbol{u}|/u_{\text{avg}}$ throughout the 180° bend for angles between $0° \leq \theta \leq 180°$. The inner bend is denoted with $r/R = 1$ and the outer bend is denoted with $r/R = -1$.

B.3.4 Turbulence intensity

The turbulence intensity is used as a method to evaluate the root-mean-square (RMS) value for the velocity fluctuations and is evaluated as

$$I = \frac{u_{\text{rms}}}{u_{\text{avg}}} = \sqrt{\frac{1}{3}\left(\langle u_x' \rangle^2 + \langle u_y' \rangle^2 + \langle u_z' \rangle^2\right)} \cdot \frac{1}{u_{\text{avg}}} \,. \tag{B.6}$$

Herein, the velocity fluctuations are the time-averaged velocity fluctuations defined by

$$\langle \boldsymbol{u}' \rangle^2 = \frac{1}{N} \sum_{i=0}^{N} (\boldsymbol{u} - \langle \boldsymbol{u} \rangle)^2 \,. \tag{B.7}$$

The turbulence intensity is evaluated downstream of the pipe bend to analyse the turbulence induced and how it evolves as a function of the downstream length. Fig. B.14 shows the turbulence intensity profiles at the outlet of the bend, $x = 0$, at a downstream distance of $x = 5d_h$ and close to the outlet of the computational domain, $x = 9d_h$. It is observed that the smallest bend radius induces the largest magnitude of turbulence, shown in Fig. B.14a. When the flow leaves the bend, a skewed turbulence intensity profile is observed for the two smallest bend radii. A larger turbulence intensity at the inner radius compared to the outer radius. Combining the turbulence intensity profile with the time-averaged velocity profile in Fig. B.10 shows that the largest magnitude of turbulence intensity is induced at the location where the streamwise velocity is the lowest. As the bend radius increases, smaller magnitudes of turbulence intensity are observed at the outlet of the bend shown. Comparing the turbulence intensity profile at the outlet of the bend to the profile at the outlet of the domain shows that the turbulence decreases for the smallest bend radii and increases downstream of the

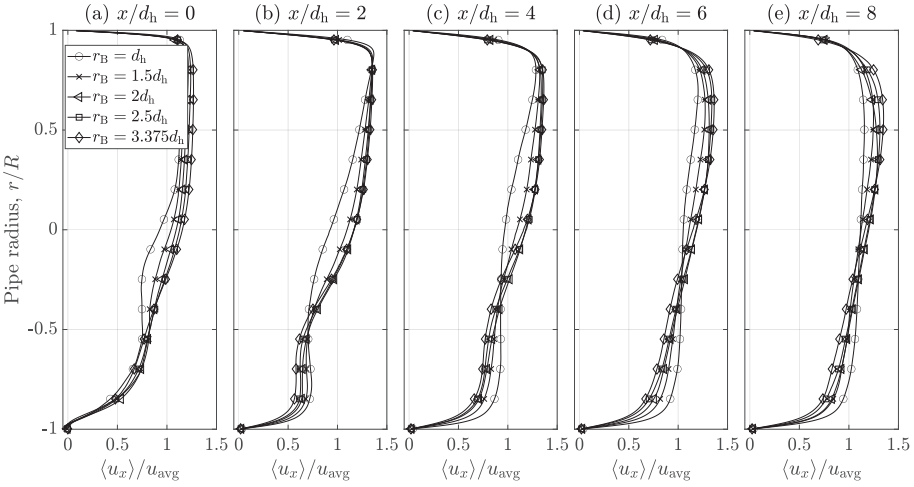

Fig. B.10: Normalised streamwise velocity profile downstream of the pipe bend for the geometrical symmetry plane of the pipe.

bend for the largest bend radii. A decreasing magnitude of turbulence intensity is observed for the two smallest bend radii, $d_h \leq r_B \leq 1.5d_h$, in Fig. B.14a and B.14b. A relative small change is observed for the configuration with a bend radius of $r_B = 2d_h$ in Fig. B.14c and an increasing trend is observed for the bend radii of $2d_h \leq r_B \leq 2.5d_h$ in Fig. B.14d and B.14e.

Averaging the turbulence intensity over the cross-sectional plane downstream of the bend shows how the evolution of the turbulence as a function of the downstream length. Fig. B.12 shows the area-averaged turbulence intensity, $\bar{I}$, for the five different bend radii. As shown in the profile in Fig. B.14, the simulation with the smallest bend radius induces significantly more turbulence at the outlet of the bend compared to the other configurations. The turbulence intensity for the smallest bend radius decreases with a larger gradient compared to the other bend radii, meaning that the turbulence dissipates faster at this configuration.

Another interesting observation, when analysing the area-averaged turbulence intensity is that the two simulations with the smallest bend radii, $r_B = d_h$ and $r_B = 1.5d_h$, both have a lower magnitude of turbulence intensity at the outlet of the pipe bend compared to the outlet of the domain. It is shown, in Fig. B.10, how the velocity profile becomes skewed downstream of the bend as the bend radius increases. A higher velocity profile is observed at the outer radius of the pipe which serves to induce more turbulence which is shown in the turbulence intensity profile in Fig. B.14. The configuration with a bend radius of $r_B = 2d_h$ remains almost constant downstream of the bend. This is also seen when analysing the turbulence intensity profile in Fig. B.14c.

At the outlet of the computational domain, $x = 10d_h$, the area-averaged turbulence intensity for the configurations is between 8.4 % and 9 % . There is only a small difference between the different bend radii when observing the area-averaged turbulence intensity at the outlet of the domain. The smallest bend radii have the lowest value which is approaching the area-averaged turbulence intensity observed at the inlet. To achieve

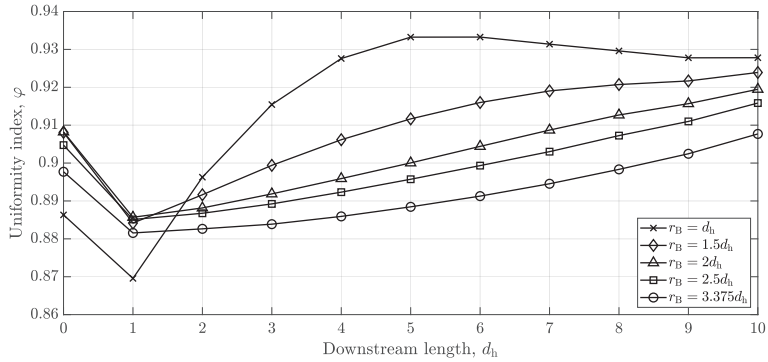

Fig. B.11: Uniformity index, φ, for the velocity profile as a function of the pipe length.

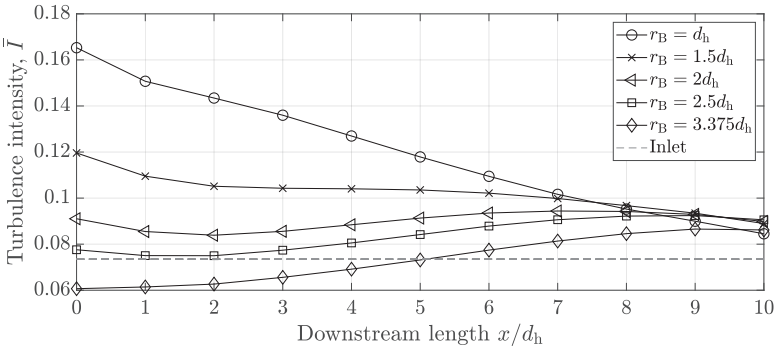

Fig. B.12: Cross-sectional area-averaged turbulence intensity, $\bar{I}$, as a function of the length after the pipe bend for the different bend radii.

a turbulence intensity magnitude of the same order as is observed at the inlet, the downstream length would have to be extended to analyse at what position the impact of the upstream bend is negligible.

Combining the results from the area-averaged turbulence intensity in Fig. B.12, the turbulence intensity profile in Fig. B.14 and the uniformity index of the velocity profile in Fig. B.11 provides information about the recovery length for the velocity profile. The turbulence intensity is largest at the outlet of the bend for the smallest bend radius and decays with the largest gradient. This configuration is also where the shortest recovery length is observed, which supports the indication of Hellström et al. (2013) that the recovery of the velocity profile is driven by turbulent transport.

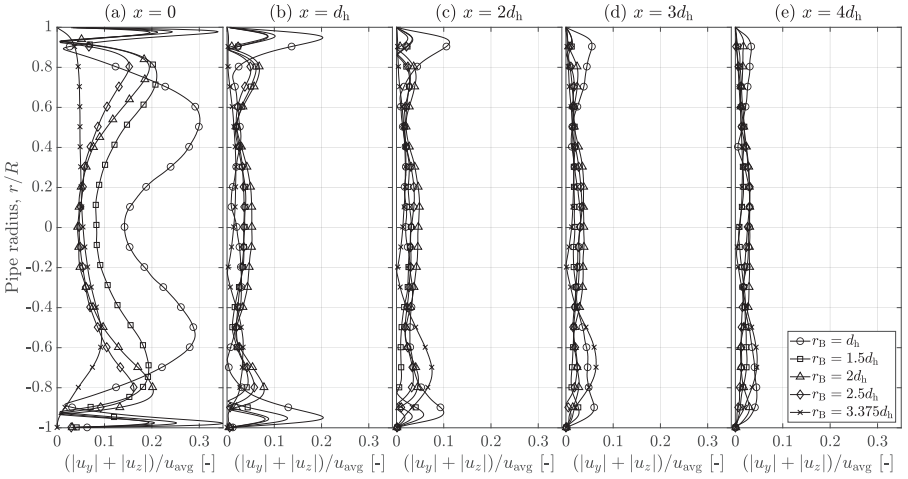

Fig. B.13: Normalised secondary velocity, $\left(\left|u_y\right| + |u_z|\right)/u_{avg}$, at B.13a: $x = 0$ after the pipe bend, B.13b: $x = 1d_h$ after the pipe bend, B.13c: $x = 2d_h$ after the pipe bend, B.13d: $x = 3d_h$ after the pipe bend and B.13e: $x = 4d_h$ after the pipe bend.

B.4 Conclusion

In this study, large-eddy simulations have been carried out for a straight pipe with a length of $x = 10d_h$ followed by a 180° pipe bend which transitions to another straight pipe with a length of $x = 10d_h$ with the focus on studying the decay of secondary motion and turbulence intensity when having different bend radii. A total of 5 simulations are carried out with different bend radii, namely $r_B = d_h$, $r_B = 1.5d_h$, $r_B = 2d_h$, $r_B = 2.5d_h$ and $r_B = 3.375d_h$ at a Reynolds number of $Re_h = 10,000$. The numerical model is validated against experimental data presented by Toonder and Nieuwstadt (1997) for the straight pipe section and against DNS data of Wang et al. (2018) as well as experimental PIV-HS data of Sattarzadeh (2011) and Kalpakli Vester et al. (2016) for 90° bend. Normalised velocity profiles and contours, secondary flow patterns, velocity profile uniformity index and turbulence intensity of the different bend radii are analysed downstream of the 180° bend.

The secondary flow vortices induced by the pipe bend increase in magnitude as the bend radius decreases. It shows how two peaks of secondary flow are dominating immediately after the bend and as the flow moves further downstream, the secondary flow is dominating closer to the walls. The normalised velocity profile becomes skewed with a higher normalised velocity at the outer radius of the bend as the flow is forced towards this outer radius. At the outlet of the bend, a small difference in the normalised velocity profiles is observed, meaning that the transition between the curvature of the bend and the straight pipe is an important factor in inducing downstream turbulence.

Like the increasing magnitude of secondary flow, the turbulence intensity increases as the bend radius decreases. For the two simulations with the smallest bend radii, $r_B = d_h$ and $r_B = 1.5d_h$, a decreasing gradient of turbulence intensity is observed

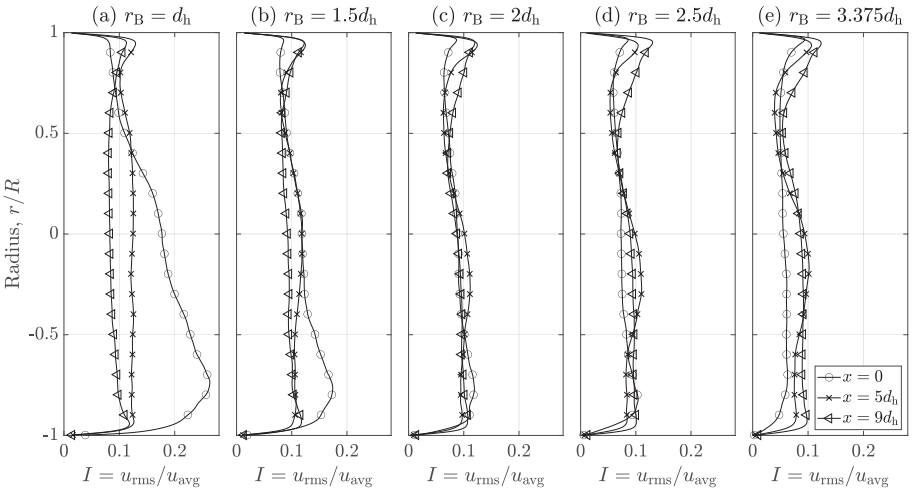

Fig. B.14: Turbulence intensity profiles at the outlet of the bend, $x = 0$, at a downstream distance of $x = 5d_h$ and $x = 9d_h$ for the different bend radii. The inner pipe radius is defined by $r/R = -1$ and the outer is defined by $r/R = 1$.

downstream of the bend and an increasing gradient for the turbulence intensity is observed for the two simulations with the largest bend radii, $r_B \geq 2.5d_h$. It is shown that the large magnitude of induced turbulence at the outlet of the bend, causes the velocity profile to recover faster, as the uniformity index of the velocity profile increases faster for the smallest bend radius. As the turbulence dissipates with a larger gradient, the velocity profile recovers over a shorter distance. This observation supports the statement of Hellström et al. (2013), who state that the recovery of the velocity profile is driven by turbulence transport.

References

M. Anwer, R. M.C. So, and Y. G. Lai. Perturbation by and recovery from bend curvature of a fully developed turbulent pipe flow. *Physics of Fluids A*, 1(8):1387–1397, 1989. ISSN 08998213. doi: 10.1063/1.857315.

J. Azzola, J. A.C. Humphrey, H. lacovides, and B. E. Launder. Developing turbulent flow in a u-bend of circular cross-section: Measurement and computation. *Journal of Fluids Engineering, Transactions of the ASME*, 108(2):214–221, 1986. ISSN 1528901X. doi: 10.1115/1.3242565.

W.R. Dean. The stream-line motion of fluid in a curved pipe. *The London, Edinburgh, and Dublin Philosophical Magazine and Journal of Science*, 5(30):673–695, 4 1928. ISSN 1941-5982. doi: 10.1080/14786440408564513.

Massimiliano Di Liberto, Ivan Di Piazza, and Michele Ciofalo. Turbulence structure and

budgets in curved pipes. *Computers and Fluids*, 88:452–472, 12 2013. ISSN 00457930. doi: 10.1016/j.compfluid.2013.09.028.

Erik Gotfredsen, Jens Dahl Kunoy, Stefan Mayer, and Knud Erik Meyer. Experimental validation of RANS and DES modelling of pipe flow mixing. *Heat and Mass Transfer/Waerme- und Stoffuebertragung*, pages 2211–2224, 2020. ISSN 14321181. doi: 10.1007/s00231-020-02835-8.

J. Hærvig, K. Sørensen, and T.J. J. Condra. Early stages of agglomeration of adhesive particles in fully-developed turbulent pipe flows. *International Journal of Multiphase Flow*, 106:254–267, 9 2018. ISSN 0301-9322. doi: 10.1016/J.IJMULTIPHASEFLOW.2018.04.017.

Leo H.O. Hellström, Metodi B. Zlatinov, Guangjun Cao, and Alexander J. Smits. Turbulent pipe flow downstream of a 90° bend. *Journal of Fluid Mechanics*, 735:R7, 2013. ISSN 14697645. doi: 10.1017/jfm.2013.534.

R. I. Issa. Solution of the implicitly discretised fluid flow equations by operator-splitting. *Journal of Computational Physics*, 62(1):40–65, 1 1986. ISSN 10902716. doi: 10.1016/0021-9991(86)90099-9.

A. Kalpakli and R. Örlü. Turbulent pipe flow downstream a 90° pipe bend with and without superimposed swirl. *International Journal of Heat and Fluid Flow*, 41:103–111, 6 2013. ISSN 0142727X. doi: 10.1016/j.ijheatfluidflow.2013.01.003.

Athanasia Kalpakli Vester, Sohrab S. Sattarzadeh, and Ramis Örlü. Combined hot-wire and PIV measurements of a swirling turbulent flow at the exit of a 90° pipe bend. *Journal of Visualization*, 19(2):261–273, 2016. ISSN 18758975. doi: 10.1007/s12650-015-0310-1.

Jongtae Kim, Mohan Yadav, and Seungjin Kim. Characteristics of Secondary Flow Induced by 90-Degree Elbow in Turbulent Pipe Flow. *Engineering Applications of Computational Fluid Mechanics*, 8(2):229–239, 2014. ISSN 1994-2060. doi: 10.1080/19942060.2014.11015509.

B. E. Launder and D. B. Spalding. The numerical computation of turbulent flows. *Computer Methods in Applied Mechanics and Engineering*, 3(2):269–289, 3 1974. ISSN 0045-7825. doi: 10.1016/0045-7825(74)90029-2.

F Nicoud and F Ducros. Subgrid-Scale Stress Modelling Based on the Square of the Velocity Gradient Tensor. *Flow, Turbulence and Combustion*, 62:183–200, 1999.

Stephen K. Robinson. Coherent motions in the turbulent boundary layer. *Annual Review of Fluid Mechanics*, 23(1):601–639, 11 1991. ISSN 00664189. doi: 10.1146/annurev.fl.23.010191.003125.

R. Röhrig, S. Jakirlić, and C. Tropea. Comparative computational study of turbulent flow in a 90° pipe elbow. *International Journal of Heat and Fluid Flow*, 55:120–131, 10 2015. ISSN 0142727X. doi: 10.1016/j.ijheatfluidflow.2015.07.011.

M. Rowe. Measurements and computations of flow in pipe bends. *Journal of Fluid Mechanics*, 43(4):771–783, 10 1970. ISSN 14697645. doi: 10.1017/S0022112070002732.

André Luís Sotero Salustiano Martim, José Gilberto Dalfré Filho, Yvone de Faria Lemos De Lucca, and Ana Ines Borri Genovez. Electromagnetic flowmeter evaluation in real facilities: Velocity profiles and error analysis. *Flow Measurement and Instrumentation*, 66:44–49, 4 2019. ISSN 09555986. doi: 10.1016/j.flowmeasinst.2019.01.001.

S. S. Sattarzadeh. *Experimental study of complex pipe flows*. PhD thesis, KTH Mechanics, 2011.

K. Sudo, M. Sumida, and H. Hibara. Experimental investigation on turbulent flow in a circular-sectioned 90-degree bend. *Experiments in Fluids*, 25:42–49, 1998. doi: 10.1007/s003480050206.

K. Sudo, M. Sumida, and H. Hibara. Experimental investigation on turbulent flow through a circular-sectioned 180° bend. *Experiments in Fluids*, 28(1):51–57, 1 2001. ISSN 07234864. doi: 10.1007/s003480050007.

Den Toonder and J M J Nieuwstadt. Reynolds number effects in a turbulent pipe flow for low to moderate Re. *Physics of Fluids*, 9(11):3398–3409, 1997. doi: 10.1063/1.869451.

T Von Kármán. Mechanische Ähnlichkeit und Turbulenz. *Göttinger Nachr*, pages 58–76, 1930.

Zhixin Wang, Ramis Örlü, Philipp Schlatter, and Yongmann M. Chung. Direct numerical simulation of a turbulent 90° bend pipe flow. *International Journal of Heat and Fluid Flow*, 73(January):199–208, 2018. ISSN 0142727X. doi: 10.1016/j.ijheatfluidflow.2018.08.003.

Paper C

On the design of compact hydraulic pipe flocculators using CFD-PBM

Kasper Gram Bilde, Jakob Hærvig, Kim Sørensen

The paper is under review in the
Journal of Chemical Engineering Research and Design.

The layout has been revised.

On the design of compact hydraulic pipe flocculators using CFD-PBM

Kasper Gram Bilde*,[1], Jakob Hærvig[1], Kim Sørensen[1]

* *Corresponding author*
[1] *Aalborg University, Department of Energy, Pontoppidanstræde 111, 9220 Aalborg, Denmark*

Keywords: *Multiphase flow; Particle aggregation; Particle breakage; Population balance equation; CFD-PBE*

Abstract

Designing a compact hydraulic pipe flocculator is a common challenge for various water purification and wastewater processes where space is limited. Various geometrical parameters are analysed to identify the most important parameters when designing an efficient system for a Reynolds number of $Re_D = 20,000$*. A coupled CFD-PBE model is applied to a total of 123 geometrical configurations to simulate particle aggregation and breakage due to the local velocity gradients in the configurations. The shear present in the 90° pipe bends is the dominating factor in the final aggregate size and therefore the most important geometrical factor is the bend radius. Secondly, it is observed that the primary length,* L_1*, has the second-largest impact as a linearly increasing particle diameter is observed during the straight pipe. Helically coiled geometrical configurations with no straight sections,* $L_1 = L_2 = 0$*, and a bend radius of* $r_b \geq 2d_h$ *result in large particles as a constant but moderate cross-sectionally averaged turbulent energy dissipation is observed throughout the pipe. The largest volume-averaged particle size is observed for a configuration with a primary length of* $L_1 = 20d_h$*, a secondary length of* $L_2 = 0$ *and a bend radius of* $r_b = 2.5d_h$*.*

C.1 Introduction

Flocculation of micron-sized particles is an important operation for a large range of freshwater and wastewater treatment plants to achieve an efficient liquid-solid separation. As many wastewater treatment plants rely on the separation of solids due to sedimentation it is important to obtain large stable agglomerates, as the sedimentation velocity, v_s, is a function of the effective particle diameter, $v_s \propto d_p^2$ according to Stokes law of settling.

Flocculation systems can generally be categorised into two groups, namely mechanical- and hydraulic flocculation. In mechanical flocculation systems, a mechanical stirrer is operated to introduce sufficient magnitudes of velocity fluctuations in the fluid which causes the particles to collide and agglomerate. The turbulence in hydraulic flocculation systems is driven by the fluid flow as the fluid passes through the application

which introduces velocity fluctuations, e.g. a baffled basin, where the velocity fluctuations in the flow are driven by flow obstructions caused by the baffles. In land-based wastewater treatment systems, baffled basins with a large surface area, often referred to as the footprint, are often used, but some industries do not have the space for such large basins or tanks. This is the case for marine water treatment plants, where a compact pipe flocculator can be utilised, which consists of a series of consecutive circular pipe bends.

Historically, Smoluchowski (1917) formulated a mathematical model describing the theoretical orthokinetic flocculation of particles under laminar conditions. In practice, flocculation happens under turbulent conditions, which is why Camp and Stein (1943) replaced the velocity gradient term, $\mathrm{d}v/\mathrm{d}z$ with a measurable average value using the root mean square (RMS) velocity gradient. The RMS velocity gradient then becomes a function of the total power dissipated in the entire system. In more recent years, computational fluid dynamics (CFD) has proven to be a reliable method to describe the local energy dissipation within a system and several researchers have shown the capabilities of using CFD to predict orthokinetic flocculation in both mechanical and hydraulic systems (Bridgeman, 2006; Vadasarukkai et al., 2011; Törnblom, 2018; Oliveira and Donadel, 2019; Zhan et al., 2021).

Laine et al. (1999) were among the early researchers to use CFD to study the settling of particles in a flocculation tank. Three different regimes were determined inside the settling tank, namely rapid agitation, slow agitation and laminar flow. The turbulence in the flow was modelled using the Re-Normalisation Group (RNG) k-ε model proposed by Yakhot et al. (1992) and from the velocity contours the researchers concluded that the fluid motion sometimes caused aggregates to flow to the surface and thereby float instead of sink.

Bridgeman et al. (2008) used CFD to study the local velocity gradient with a focus on particle agglomeration and breakage. The authors studied the local velocity gradient using a single-phase steady-state Reynolds-averaged Navier Stokes
(RANS) model to simulate the shear introduced by a mechanical stirrer in a flocculation tank. The experimental- and numerical data obtained were in good agreement and expressions for the strength and breakage of an aggregate as a function of the local velocity gradient were presented.

Several researchers have applied the single-phase RANS modelling approach to simulate the hydraulics within a flocculation system with the focus on describing the local velocity gradient (Bridgeman et al., 2010; Sartori et al., 2015; Gar Alalm et al., 2016; Xiang et al., 2018; Oliveira and Donadel, 2019). The referred studies have shown that a local large velocity gradient is found inside the hydraulic domain, which leads to a local zone where the agglomerates are highly prone to breakage.

In more recent years, researchers have simulated the agglomeration and breakage of agglomerates using multiphase CFD. Focusing on a small 2-dimensional domain, Qiu et al. (2016) described the agglomeration and sedimentation of spherical particles using a coupling of CFD and discrete element modelling (DEM) using the Johnson-Kendall-Roberts adhesion theory. The researchers showed how agglomerated particles within lid-driven cavity sediments sink as opposed to small non-agglomerated particles.

The CFD-DEM models have high predicting capabilities as collisions between particles are resolved, but due to their nature of resolving each Lagrangian particle, this

limits the use within flocculation systems as particles are usually within the micron-sized range. For industrial applications, this means that the number of Lagrangian particles quickly exceeds $n_p > 10^{12}$ making it unfeasible even with modern computing capacities. Therefore, coarse-graining of the particles is often used (Tausendschön et al., 2020; Jiang et al., 2020), or alternative, other methods are applied to solve the particle phase and the momentum exchange between the phases.

Another approach, which has been applied successfully, is to use the coupled population balance equation (PBE) to track the number density function of the disperse phase within the computational domain (Marchisio et al., 2003; Yao et al., 2014a,b; Lau and Kind, 2016; Wang et al., 2022). Different solutions of the PBE have been applied throughout the literature, but the majority of the papers from recent years are based on the methods of moments (MOM) and its derivatives. Marchisio et al. (2003) applied the quadrature MOM (QMOM) to solve the PBE and describe the aggregation and breakage of solid particles in a Taylor-Couette flow. As the QMOM is based on solving a consecutive set of low-order integer moments of the number density function, the integral source terms of the PBE are approximated using Gaussian quadrature. To solve for a continuous number density function, Yuan et al. (2012) proposed the Extended QMOM (EQMOM) and Passalacqua et al. (2018) implemented this approach as the OpenQBMM module for the OpenFOAM CFD library. Kumar and Ramkrishna (1996) proposed another solution to the PBE by discretising the PBE into several classes, which is why this method is often referred to as the class method or sometimes also the discrete- or sectional method. Lehnigk et al. (2021) implemented the class method into the OpenFOAM CFD library as part of the Euler-Euler model and used it to successfully simulate the synthesis of titania powder in a tubular reactor. The QMOM requires a low number of scalar equations, making this method the least computationally expensive, but this method has the drawback that there is no direct information about the number density function and its shape. The EQMOM provides this additional information as the number density function is approximated using a combination of kernel density functions. The EQMOM is, however, more computationally expensive compared to the QMOM and Li et al. (2017) reports that the EQMOM is up to 30x more computationally expensive than the QMOM. The class method is also more computationally expensive than the QMOM, as a set of discrete PBE has to be solved for each size class, and this method also requires some knowledge of the particle size range in advance. The advantage of the class method is that the number density function and its shape are readily available at any point and time in the computational domain. This also means that this method is highly intuitive to apply, as knowledge of the particle size range is often known and the shape of the number density function is often the parameter of interest.

In this study the geometrical parameters of a hydraulic pipe flocculator are varied to analyse the effects on the particle size distribution. The geometrical parameters are the primary length, L_1, the secondary length, L_2, the bend radius r_b and the pitch of inclination, φ. A visualisation of the geometrical parameters are shown in Fig. C.1. The parameters are varied as a function of the hydraulic diameter of the pipe, d_h.

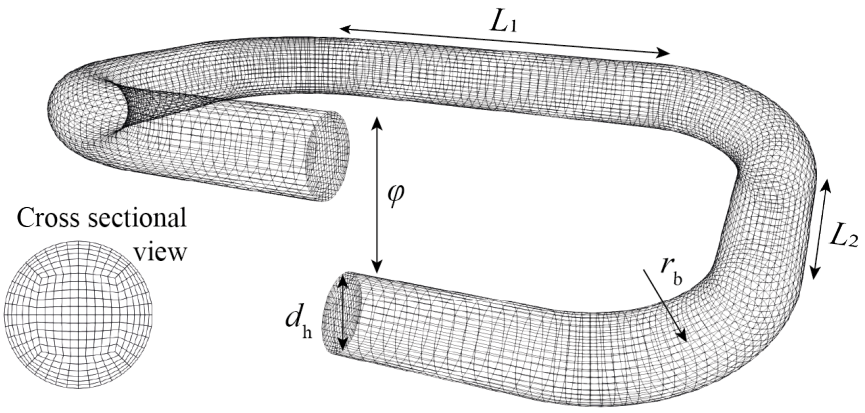

Fig. C.1: The geometrical configuration of the setup. The pitch of inclination, φ, denotes the height between each pass, the primary and secondary lengths, L_1 and L_2, denote the length in the primary and secondary direction and the bend radius of the pipe is denoted by r_b.

C.2 Numerical framework

All geometrical configurations presented in this study are constructed with the same cross-sectional mesh, which is seen in Fig. C.1. The computational mesh is made of hexahedral cells with a maximum angle of 120°.

C.2.1 Governing equations

The multiphase flow is described by the governing equations in the Euler-Euler framework, where a set of continuity and momentum equations is solved for each phase, φ. The fluid- and particle phases are assumed incompressible and isothermal, resulting in the governing equations seen in Eq. (C.1) and (C.2).

$$\frac{\partial}{\partial t}\left(\alpha_\varphi \rho_\varphi\right) + \nabla \cdot \left(\alpha_\varphi \rho_\varphi \boldsymbol{u}_\varphi\right) = 0 \tag{C.1}$$

$$\begin{aligned}\frac{\partial}{\partial t}\left(\alpha_\varphi \rho_\varphi \boldsymbol{u}_\varphi\right) + \nabla \cdot \left(\alpha_\varphi \rho_\varphi \boldsymbol{u}_\varphi \boldsymbol{u}_\varphi\right) - \nabla \cdot \tau_\varphi = &-\alpha_\varphi \nabla p + \alpha_\varphi \rho_\varphi \boldsymbol{g} \\ &+ \boldsymbol{M}_\varphi + \boldsymbol{S}_\varphi,\end{aligned} \tag{C.2}$$

where α is the volume fraction, ρ is the density, $\boldsymbol{u}$ is the velocity, τ is the stress tensor, p is the pressure which is shared by the continuous- and dispersed phase, $\boldsymbol{g}$ is the gravitational acceleration, $\boldsymbol{S}$ is the momentum source term. $\boldsymbol{M}$ is the momentum exchange at the interface between the phases which is defined as

$$\boldsymbol{M}_\varphi = \sum_{\varphi=0, \varphi\neq\xi}^{N} \left(\boldsymbol{F}_{\mathrm{L},\varphi\xi} + \boldsymbol{F}_{\mathrm{D},\varphi\xi} + \boldsymbol{F}_{\mathrm{T},\varphi\xi} + \boldsymbol{F}_{\mathrm{VM},\varphi\xi}\right), \tag{C.3}$$

where $\boldsymbol{F}_{\mathrm{L}}$ is the lift force, $\boldsymbol{F}_{\mathrm{D}}$, is the drag force, $\boldsymbol{F}_{\mathrm{T}}$ is the turbulent dispersion force and $\boldsymbol{F}_{\mathrm{VM}}$ is the virtual mass force transferred between phase φ and ξ. As momentum is conserved, it is implied that $\sum_{\varphi} \boldsymbol{M}_{\varphi} = 0$. A source term is added in the continuous phase to maintain a desired velocity by adding a pressure gradient increment to the pressure gradient in Eq. (C.2) to maintain the desired bulk velocity. The governing equations are solved using the Reynolds averaged Navier Stokes (RANS) model, where the averaged components are solved and the fluctuating components are modelled.

C.2.2 Continuous phase turbulence modelling

To account for turbulence in the continuous phase, the stress tensor, τ_{f}, is modelled using the Re-Normalisation Group k-ε model by Yakhot et al. (1992). The statistical Re-Normalisation group theory is applied to resolve the smallest eddies in the inertial range. This procedure effectively removes small scales of turbulence by modifying the turbulent viscosity. The two-equation RNG k-ε provides the closure equations for modelling the turbulence. The governing equations for the RNG k-ε are given by

$$\frac{\partial}{\partial t}\left(\alpha_{\mathrm{f}}\rho_{\mathrm{f}}k\right) + \nabla\cdot\left(\alpha_{\mathrm{f}}\rho_{\mathrm{f}}k\boldsymbol{u}_{\mathrm{f}}\right) = \nabla\left[\left(\mu_{\mathrm{f}} + \frac{\mu_{\mathrm{t}}}{\sigma_{\mathrm{k}}}\right)\nabla k\right] + P_k - \alpha_{\mathrm{f}}\rho_{\mathrm{f}}\varepsilon \tag{C.4}$$

and

$$\begin{aligned}\frac{\partial}{\partial t}\left(\alpha_{\mathrm{f}}\rho\varepsilon\right) + \nabla\cdot\left(\alpha_{\mathrm{f}}\rho_{\mathrm{f}}\varepsilon\boldsymbol{u}_{\mathrm{f}}\right) = \nabla\left[\left(\mu_{\mathrm{f}} + \frac{\mu_{\mathrm{t}}}{\sigma_{\varepsilon}}\right)\nabla\varepsilon\right] + C_{1\varepsilon}\frac{\varepsilon}{k}P_k \\ -C_{2\varepsilon}\alpha_{\mathrm{f}}\rho\frac{\varepsilon^2}{k}\,,\end{aligned} \tag{C.5}$$

where P_k is the production of turbulence due to the mean velocity gradients. In this work, the default values of coefficients $C_{1\varepsilon} = 1.42$ and $C_{2\varepsilon} = 1.68$ are applied.

Escue and Cui (2010) compared the higher-order Reynolds stress turbulence model (RSM) and the lower-order RNG k-ε model to experimental data for swirling flow in a pipe and concluded that the RNG k-ε was superior to the RSM model for low swirling flows. Reasonable predictions of the high swirling flows were obtained using the RNG k-ε model. Due to its comparatively low computational cost and high accuracy in predicting turbulence in swirling flows, the RNG k-ε is chosen in this study.

C.2.3 Dispersed phase pressure

In this study no shear stress tensor is applied for the particle phase, as the volume fraction is low, meaning that particle-particle interactions are neglected in this study. As a high packing density in the smallest cells is still possible, even with low bulk volume fractions, an exponential phase pressure model is applied to the particle phase. This particle phase pressure increases exponentially when the particle volume fraction approaches a maximum packing density, thereby preventing the particle phase of exceeding the maximum packing density, $\alpha_{\mathrm{p,max}}$. A pressure gradient concerning the volume fraction is added to the momentum equation, as given by

$$p' = g_0 \cdot \min\left[\exp\left(\alpha_{\mathrm{p,exp}}\left(\alpha_{\mathrm{p}} - \alpha_{\mathrm{p,max}}\right)\right), p'_{\mathrm{max}}\right]\,, \tag{C.6}$$

where a maximum allowable packing density of $\alpha_{p,max} = 0.62$ is applied along with the default values of $g_0 = 1000$, $\alpha_{p,exp} = 500$ and $p'_{max} = 1000$.

C.2.4 Lift force

To account for the lift force generated by the swirling flow around the aggregates, a lift force is applied

$$\boldsymbol{F}_L = -C_L \rho_f \alpha_p \boldsymbol{u}_r \cdot \boldsymbol{\omega} \,, \tag{C.7}$$

where the $\boldsymbol{\omega}$ is the vorticity of the continuous phase defined by $\boldsymbol{\omega} = \nabla \times \boldsymbol{u}_f$. The lift force coefficient, C_L, of Saffman (1965) and later modified and extended for finite Reynolds numbers by Mei (1992) is applied. The lift force coefficient is given as

$$C_L = \frac{3}{2\pi\sqrt{Re_\omega}} C'_L \tag{C.8}$$

where the modified lift force coefficient, C'_L, is defined as

$$C'_L = \begin{cases} 6.46 \left[\left(1 - 0.3314\beta^{0.5}\right) e^{-0.1 Re_p} + 0.3314\beta^{0.5} \right] & Re_p \leq 40 \\ 6.46 \cdot 0.0524\sqrt{\beta Re_p} & Re_p > 40 \,. \end{cases} \tag{C.9}$$

Herein, Re_ω is the vorticity Reynolds number which is defined as $Re_\omega = |\boldsymbol{\omega}| \, d_p^2 / \nu_f$, Re_p is the particle Reynolds number, defined as $Re_p = \left|\boldsymbol{u}_p - \boldsymbol{u}_f\right| d_p / \nu_f$ and $\beta = 0.5 \left(Re_\omega / Re_p\right)$.

C.2.5 Drag force

The drag force acting on the particle phase by the fluid phase is the dominating interfacial momentum transfer term and is described by

$$\boldsymbol{F}_D = \frac{1}{2} \rho_f \left|\boldsymbol{u}_r\right| \boldsymbol{u}_r C_D A_p \,, \tag{C.10}$$

where A_p is the projected surface area of the aggregates and C_D is the drag force coefficient. The drag force coefficient model Wen and Yu (1966) is applied in this study and is given as

$$C_D = \begin{cases} \frac{24}{Re_p} \alpha_f^{-2.65} & \text{for } Re_p < 0.5 \\ \frac{24}{Re_p} \left(1 + 0.15 Re_p^{0.687}\right) \alpha_f^{-2.65} & \text{for } 0.5 \leq Re_p < 1000 \\ 0.44 \alpha_f^{-2.65} & \text{for } Re_p \geq 1000 \,. \end{cases} \tag{C.11}$$

The drag coefficient model is applicable for spherical particles meaning the particles are assumed to be spherical. This is a simplification of the particles, as they are fractal-like in their nature. Mikhailov et al. (2006) analysed the optical properties of soot using an experimental technique and concluded that soot fractals form a compact shape close to a sphere when the soot particles are subject to a wet environment. Fan et al. (2016) showed how soot particles age from a loosely coupled fractal to a strongly coupled fractal when subject to a wet environment. As the particles in this study are soot and are suspended in water, this justifies the assumption of spherical particles.

C.2.6 Turbulent dispersion force

As the Stokes number of the particles is small, $\mathrm{St} = t_0 u_\mathrm{p}/l_0 < 1$, they follow the streamlines of the flow. This also means that the particles tend to follow the velocity fluctuations of the continuous phase and as the turbulence is modelled using a k-ε model, the velocity fluctuations are only modelled. A turbulent dispersion force is therefore included to account for velocity fluctuations of the continuous phase. Burns et al. (2004) performed Favre averaging of the drag force acting on the dispersed phase and proposed the turbulent dispersion force as

$$\boldsymbol{F}_\mathrm{disp} = -\frac{3}{4}\mathrm{C_D}\frac{\alpha_\mathrm{p}\rho_\mathrm{f}}{d_\mathrm{p}}\boldsymbol{u}_\mathrm{r}\frac{\nu_\mathrm{t}}{Sc_\mathrm{t}}\left(\frac{\nabla\alpha_\mathrm{f}}{\alpha_\mathrm{f}} - \frac{\nabla\alpha_\mathrm{p}}{\alpha_\mathrm{p}}\right), \tag{C.12}$$

where Sc_t is the turbulent Schmidt number, which is assumed $Sc_\mathrm{t} = 0.9$ in this study.

C.2.7 Virtual mass force

When there is a relative acceleration between the dispersed and continuous phases, an additional force arises due to the acceleration of the fluid surrounding the particle. This virtual mass force is given by

$$\boldsymbol{F}_\mathrm{VM} = -C_\mathrm{VM}\rho_\mathrm{f}\alpha_\mathrm{p}\left(\frac{D_\mathrm{p}}{Dt}\boldsymbol{u}_\mathrm{p} - \frac{D_\mathrm{f}}{Dt}\boldsymbol{u}_\mathrm{f}\right), \tag{C.13}$$

where $C_\mathrm{VM} = 0.5$ is the virtual mass force coefficient for spherical particles, D_p/Dt and D_f/Dt are the material derivatives of the dispersed and continuous phase, respectively.

C.2.8 Population balance equation

The temporal evolution of the particle size distribution is modelled using the population balance equation, which is a transport equation for the number density function. The number density function, $n(\xi, \boldsymbol{x}, t)$, is a function of an internal value ξ, a spatial coordinate, $\boldsymbol{x}$ at a given time, t. For many studies (Wang et al., 2019; Liao et al., 2018; Salehi et al., 2017), including this study, the internal value of interest is the particle size, which is why the particle volume is used as the internal value, $\xi = v_\mathrm{p}$. The population balance equation for the number density function is given as

$$\frac{\partial}{\partial t}n_v + \nabla\cdot\left(\boldsymbol{u}_\mathrm{p}n_v\right) = S_v\,, \tag{C.14}$$

where the number density function as a function of the volume is denoted by n_v for the ease of notation and S_v is the source term accounting for the discontinuous changes in the number density function, e.g. aggregation and breakage. The source term of the PBE is given by

$$S_v = \frac{1}{2}\int_0^v n_{v'}n_{v-v'}a_{v',v-v'}\mathrm{d}v' - n_v\int_0^\infty n_{v'}a_{v,v'}\mathrm{d}v' + \int_v^\infty n_{v'}b_{v'}\beta_{v,v'}\mathrm{d}v' - n_v b_v\,, \tag{C.15}$$

where the two first terms on the right-hand side account for the changes due to aggregation and $a_{v,v'}$ is the aggregation frequency. The two last terms account for the changes due to breakage, where $b_{v'}$ is the breakage frequency and $\beta_{v,v'}$ is the daughter size distribution. For details on the algorithm and discretisation, the reader is referred to the work of Lehnigk et al. (2021) who describes how the class method is implemented into the OpenFOAM CFD library.

C.2.9 Breakage kernel

The breakage kernel Kusters (1991) is applied in this study to account for the birth and death of particles due to breakage. The breakage frequency is modelled as an exponential function accounting for a maximum particle strength required for the particle to break, as given by

$$b_{v'} = \sqrt{\frac{4}{15\pi}}\sqrt{\frac{\varepsilon}{\nu}}\exp\left(-\frac{\varepsilon_{\mathrm{cr}}}{\varepsilon}\right), \tag{C.16}$$

where $\varepsilon_{\mathrm{cr}}$ is the critical energy dissipation rate required for the aggregate to break, which is defined as

$$\varepsilon_{\mathrm{cr}} = \frac{B}{r_{\mathrm{c}}}, \tag{C.17}$$

where B is a parameter describing the strength of the particles which accounts for the critical energy dissipation rate required for the particle to break and r_{c} is the collision radius. Mandelbrot (1985) proposed the correlation for the collision radius as

$$r_{\mathrm{c}} = r_0\left(\frac{n_i}{k_c}\right)^{1/D_f}, \tag{C.18}$$

where r_0 is the radius of the primary particles within an aggregate, n_i is the number of primary particles in the aggregate and k_c is a coefficient relative to packing and is assumed unity in this study (Jeldres et al., 2017). A constant fractal dimension, D_f is assumed when using this approach, meaning aggregates with a high fractal dimension withstand a higher energy dissipation rate compared to aggregates with a lower fractal dimension.

In a previous study, Bilde et al. (2022) showed a good correlation between experimental and numerical particle size distributions when using a aggregate strength parameter of $B = 50 \cdot 10^{-7}$ $\mathrm{m}^3/\mathrm{s}^3$.

C.2.10 Daughter size distribution

The discretised daughter size distribution suggested by Laakkonen et al. (2007) is implemented in this study. The daughter size distribution is a beta distribution describing the distribution of daughter particles as a function of the number of daughter particles and is given as

$$\beta_{v,v'} = (1+C_4)(2+C_4)(3+C_4)(4+C_4)\left(\frac{1}{3}\right)\left(\frac{1}{v'}\right)\left(\frac{v}{v'}\right)^2 \left(1-\frac{v}{v'}\right)^{C_4}, \tag{C.19}$$

where v and v' are the volumes of the daughter and mother particle, respectively, and C_4 is a coefficient describing the total number of daughters generated. The number of daughter particles is given by

$$n_i = \frac{4}{3} + \frac{C_4}{3} \,. \tag{C.20}$$

Bilde et al. (2022) showed good agreement between experimental and numerical particle size distributions when using a binary breakage coefficient of $C_4 = 2$ (Bilde et al., 2022).

C.2.11 Aggregation kernel

The aggregation kernel of Adachi et al. (1994) is applied in this study to account for the birth and death of new aggregates due to aggregation. This model describes the orthokinetic aggregation of particles in turbulent flows and the aggregation frequency is given by

$$a_{d,d'} = \frac{4}{3}\sqrt{\frac{3\pi}{10}}\sqrt{\frac{\varepsilon}{\nu}}\left(d + d'\right)^3 \,, \tag{C.21}$$

where d and d' denotes the diameter of two colliding aggregates.

C.3 Numerical properties and initialisation

The results presented in the following section are time-averaged values, where the value of interest is averaged over the dimensionless time of $t^+ = t\,u/d_\mathrm{h} = 100$ after a steady-state solution has been obtained. The particle phase is initialised with a monodisperse particle size distribution where all particles are positioned in the smallest size group of $d_\mathrm{p} = 1$ µm. The fluid flow is initialised without the particle phase using a steady-state single-phase model until a converged flow is obtained and then the monodisperse particles are inserted into the fully-developed fluid velocity profile. A series of simulations are carried out for different geometrical configurations to study the impact of the different compact designs.

C.3.1 Geometrical configuration

To study the particle size distribution until a steady-state solution is obtained, periodic boundary conditions are applied to the geometrical configuration. This effectively creates an infinitely long pipe flocculator where the mass- and momentum transport leaving at the outlet is re-applied at the inlet. This approach decreases the amount of computational cells in the domain and a converged steady-state solution is obtained faster.

The pitch of inclination, φ, the primary and secondary lengths, L_1 and L_2, as well as the bend radius, r_b, are the geometrical parameters of interest in this study and these are seen in Fig. C.1. All the parameters of interest are scaled using the hydraulic diameter of the pipe, d_h.

The geometrical configuration allows for analysing the impact of various combinations including a helically coiled tube flocculator, as previously reported by Oliveira and Donadel (2019), when setting $L_1 = 0$ and $L_2 = 0$, as seen in Fig. C.2.

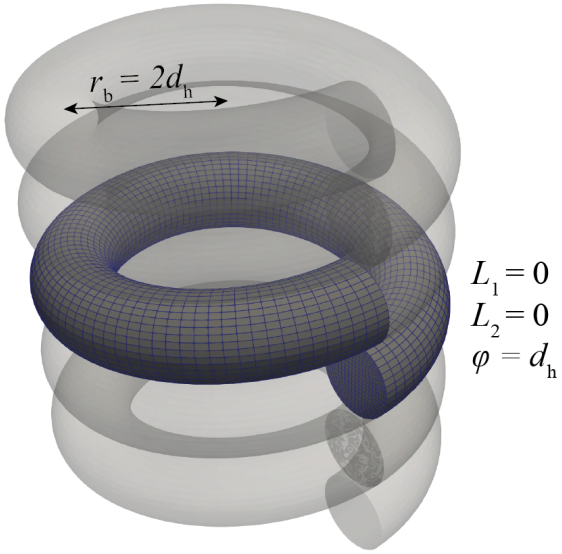

Fig. C.2: Example of a helical coiled tube flocculator with a bend radius of $r_b = 2d_h$, pitch inclination of $\varphi = d_h$ and primary and secondary lengths of $L_1 = L_2 = 0$.

In this study, the geometrical configurations are bounded by a set of values to limit the number of simulations carried out. In practice, this also means that the configuration is limited to a certain primary and secondary length, which makes out the footprint of the pipe flocculator. The primary length is bounded by $0 \leq L_1 \leq 20d_h$, the secondary length is bounded by $0 \leq L_2 \leq 10d_h$, the bend radius is bounded by $d_h \leq r_b \leq 2.5d_h$ and the pitch inclination is bounded by $d_h \leq \varphi \leq 3d_h$.

C.3.2 Simulation parameters

Particle properties from our previous study (Bilde et al., 2022) have been re-used in this study and can be seen in Table C.1. The particles analysed resembles soot particles suspended in water in terms of physical- and chemical properties, where soot is assumed to mainly consist of graphite. In our previous study, these parameters were validated against an experimentally obtained particle size distribution and a mesh independent particle size distribution was presented when using a grid with a first cell height of $y^+_{min} = 30$ and a maximum cell height of $y^+_{max} = 70$ in the middle of the pipe. The particles size distribution is bounded by a minimum size of $d_{p,min} = 1$ µm and a maximum size of $d_{p,max} = 1000$ µm. The particle size range is discretised into a total of 50 logarithmic spaced size classes with a spacing given by

$$\log_{10}\left(\frac{d_{p,i}}{d_{p,i-1}}\right) = \frac{\log_{10}\left(\frac{d_{p,N}}{d_{p,1}}\right)}{N-1} \qquad 1 < i < N\,. \tag{C.22}$$

Table C.1: Fluid- and particle properties applied for the CFD-PBM model.

Property	Symbol	Value	Unit
Daughter size coefficient	C_4	2	-
Fractal dimension	D_f	2.3	-
Kinematic viscosity	ν_f	10^{-6}	m^2/s
Particle density	ρ_p	1400	kg/m^3
Particle strength parameter	B	$50 \cdot 10^{-7}$	$\mathrm{m}^3/\mathrm{s}^3$
Primary particle size	d_0	250	nm

All simulations are carried out for a fluid flow with a turbulent Reynolds number of $Re_\mathrm{D} = 20,000$, corresponding to a plug flow velocity of $\overline{u} = 0.5$ m/s.

C.4 Results and Discussion

C.4.1 Inclination pitch

The impact of increasing the inclination pitch is analysed before analysing the other geometrical parameters, as this parameter is assumed to have a minor impact on the particle size distribution. A computational domain with a constant primary- and secondary length of $L_1 = 5d_\mathrm{h}$ and $L_2 = 2d_\mathrm{h}$ and a constant bend radius of $r_\mathrm{b} = 2d_\mathrm{h}$ is constructed. The pitch is bounded by $d_\mathrm{h} \leq \varphi \leq 3d_\mathrm{h}$ and varied by integer intervals, resulting in a total of 3 simulations.

The converged particle size distributions for the three simulations are seen in Fig. C.3, where the volumetric density function is plotted as a function of the particle diameter. The difference between the simulations is negligible, meaning that the pitch has a negligible impact on the particle size distribution for the liquid-solid flow in this study when dealing with a pitch of inclination within the range of $d_\mathrm{h} \leq \varphi \leq 3d_\mathrm{h}$ and will be analysed no further in this study.

In practice, this observation means that there is no performance difference for a pipe flocculator with a smaller pitch, which is, in many cases more desirable, as the pipe flocculator takes up less volume and thereby becomes more compact.

C.4.2 Geometrical parameters

The effect of the three remaining parameters, namely the bend radius, r_b, the primary length, L_1 and the secondary length L_2, are analysed to study the particle size distribution. As the parameters are bounded, a total of 120 simulations are carried out, varying the bend radius with intervals of $0.5d_\mathrm{h}$, the primary length by $5d_\mathrm{h}$ and the secondary length by $2d_\mathrm{h}$.

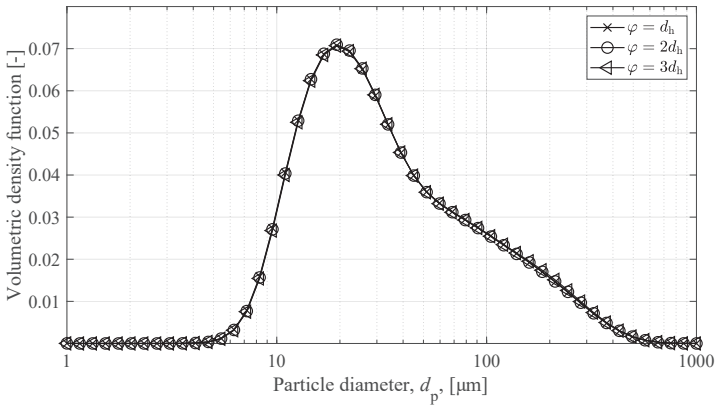

Fig. C.3: Particle size distribution for the 3 simulations with inclination pitches bounded by $d_h \leq \varphi \leq 3d_h$ as well as $L_1 = 5d_h$, $L_2 = 2d_h$ and $r_b = 2d_h$. The difference between the three simulations is negligible.

C.4.3 Particle size over the total length

The amount of turbulence induced within the pipe changes throughout the geometry depending on the given configuration and to visualise the impact of this, the area-average of the time-averaged Sauter mean diameter, $\tilde{d}_{32}$, is used to visualise the changing particle size distribution over the length of the pipe. As the geometrical configuration is periodic around the centre of length, the area averaged Sauter mean diameter is also periodic, which is evident from Fig. C.4 for 5 configurations. It is immediately visible that the Sauter mean diameter along the length of the pipe consists of some recognisable patterns for all configurations, except for the configuration with $L_1 = L_2 = 0$, where a constant particle diameter is observed. A constant particle diameter, $\tilde{d}_{32}$, is observed for all cases with no straight pipe lengths, as a constant turbulent energy dissipation rate is observed in these cases.

Between the start of the configuration, $L/L_T = 0$ and the first bend, a linear increasing trend is observed. When the flow is exposed to the first bend the mean diameter, $\tilde{d}_{32}$, decreases from its peak value to a lower value. As the flow passes the first bend, a linear increasing Sauter mean diameter is observed as particles have time to aggregate in the low shear region. As the second bend is encountered, the mean diameter drops once again and if the secondary length is sufficiently short, $L_2 \leq 6d_h$, the Sauter mean diameter drops to a smaller value compared to the first bend. This is observed for all cases, except for the configurations with $L_1 = L_2 = 0$, where the flow is subject to a constant curvature and the turbulent dissipation rate, ε, is therefore kept to a constant magnitude, resulting in a constant mean diameter over the length of the configuration.

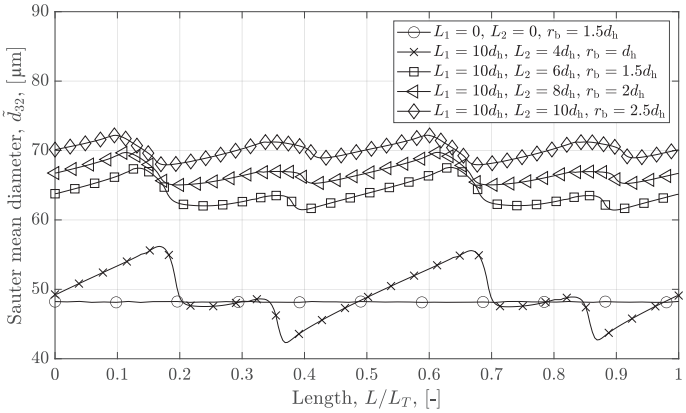

Fig. C.4: Area-averaged Sauter mean diameter, $\tilde{d}_{32}$, as a function of the relative length of the geometrical configuration for 5 different configurations. The mean particle diameter is symmetric around $L/L_T = 0.5$. The self-repeating mean particle diameter is observed for all cases.

C.4.4 Local aggregation and breakage

Analysing the area-averaged Sauter mean diameter in Fig. C.4, it is visible that aggregates are more prone to breakage throughout- and downstream of the 90° bend. Calculating the gradient of the mass flow of each size class, $\dot{m}_i$, throughout the length of the configurations using Eq. (C.24), it is visible what particle size range is affected by the given curvature and velocity profile at the inlet of the bend. This can be applied for each configuration, but the configuration with the smallest radius yields the largest curvature and hence introduces the most turbulence. The configurations with a primary lengths of $L_1 = 10d_h$ and secondary lengths of $4d_h < L_2 < 10d_h$ and a bend radius of $r_b = d_h$ are analysed. This is also the configuration used in Fig. C.4. The configurations are analysed at the inlet of the first bend, $\theta = 0°$, halfway through the first bend, $\theta = 45°$, at the outlet of the first bend, $\theta = 90°$ and halfway through the configuration, $L/L_T = 0.5$. The corresponding mass flow into a cell layer, j, is calculated for the given size group, i, as

$$\dot{m}_{i,j} = f_{i,j}\rho_p \, \boldsymbol{u}_{p,j} \cdot \boldsymbol{n}_j A \,, \tag{C.23}$$

where $\boldsymbol{n}$ is the normal direction of the face of the computational cell and A is the area of the computational cell.

The mass flow gradient is found by

$$\nabla \dot{m}_{i,j} = \frac{d}{dL}\left(\dot{m}_{i,j} - \dot{m}_{i,j-1}\right) \tag{C.24}$$

The mass flow gradient for the different particle size groups is seen in Fig. C.5. When the flow enters the first bend (Fig. C.5a) it is visible how medium to large aggregates, $10\,\mu m < d_p < 300\,\mu m$, are formed at a high rate, resulting in a positive production of these aggregates. This is due to a slightly larger turbulent dissipation rate being present at this location. At an angle of 45° through the first bend (Fig. C.5b) the

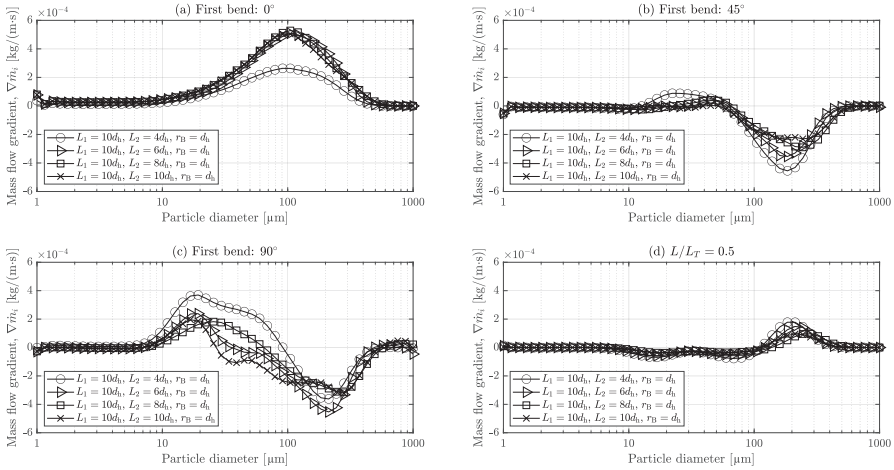

Fig. C.5: Mass flow gradient of the size classes before the first bend, Fig. C.5a, at an angle of 45° through the first bend, Fig. C.5b, at the outlet of the first bend, Fig. C.5c and halfway through the configurations, Fig. C.5d. A negative mass flow gradient means that the total mass of the size class decreases and the opposite when a positive gradient is observed.

turbulent dissipation rate increases to a magnitude where aggregates with a diameter of $d_p > 60$ µm breaks at a higher rate than they form, resulting in a negative production of the largest aggregates. This observation is also visible when inspecting the mass flow gradient at the outlet of the bend in Fig. C.5c, where it is visible that a positive production of medium sized aggregates takes place while a negative production of large aggregates is occurring due to the induced turbulence by the curvature of the bend. Halfway through the domain, shown in Fig. C.5d, it is visible that larger aggregates, $d_p > 100$ µm, are formed at a lower rate due to a sufficiently low turbulent dissipation rate, which is supported by the linearly increasing trend observed in Fig. C.4 for the straight pipe sections.

This approach provides an in-depth insight into which aggregate sizes form at any given location throughout the configurations and the same tendency is observed for the different bend radii. The magnitude of the mass flow gradient is, however, a function of the bend radius and the inlet velocity profile to a bend, which causes this value to change for the different configurations.

C.4.5 Downstream effect of a pipe bend

It is clear when analysing both Fig. C.4 and C.5 that the particle diameter decreases over the pipe bend and as the aggregates move downstream from the bend, they start to increase in size again. The gradient of the area-averaged Sauter mean diameter is evaluated along the length of the pipe downstream a bend, $\mathrm{d}\,\tilde{d}_{32}/\mathrm{d}L$, for the configurations with $L_1 = 10d_h$.

Analysing the gradient of the Sauter mean diameter it is immediately visible how

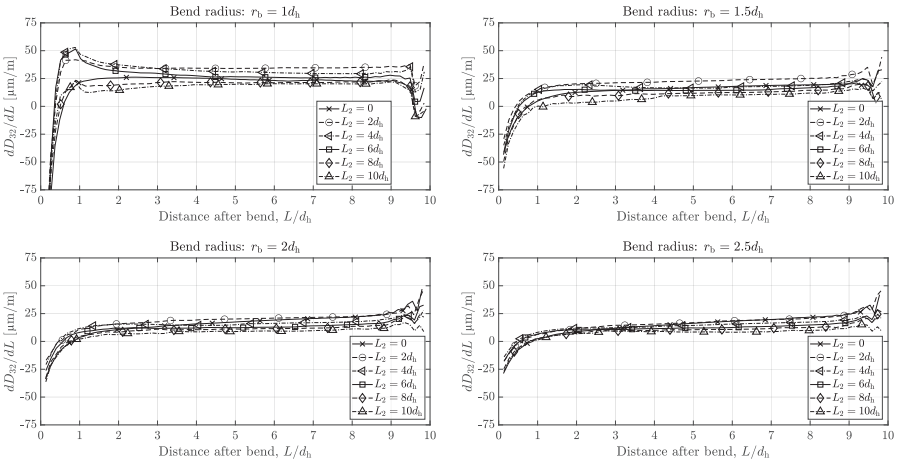

Fig. C.6: Gradient of the Sauter means diameter in the straight section of the pipe for the configurations where $L_1 = 10d_h$. The results are divided into plots according to the bend radius of the configurations, giving Fig. C.6a: $r_b = d_h$, Fig. C.6b: $r_b = 1.5d_h$, Fig. C.6c: $r_b = 2d_h$ and Fig. C.6d: $r_b = 2.5d_h$

the configurations experience the largest negative gradient immediately at the outlet of a bend, where the configuration with the smallest bend radius, $r_b = d_h$ experiences the largest magnitude when comparing the configurations. It is found that the particle size for all configurations starts to recover at a downstream distance of $L > d_h$ from a bend, as a positive gradient is observed for all configurations. When the aggregates start to approach the second bend, the gradient starts to increase, as the turbulent energy dissipation rate increases slightly. This is true except for the configuration with the smallest bend radius, as turbulence is induced over a short length and a negative gradient is observed when approaching the next bend.

For the configurations with the smallest bend radius, $r_b = d_h$, the gradient approaches a constant value after a length of $L = 2d_h$ which means that the particles will aggregate at a constant rate within this length of the pipe. For the configurations with the largest bend radii, $r_b = 2d_h$ and $r_b = 2.5d_h$, the gradient continuously increases after the downstream of the bend. As these configurations experience a less negative gradient at the outlet of the bend and an increasing gradient along the length downstream of the pipe, this explains why these configurations will have the largest overall size when analysing the particle size over the entire domain.

C.4.6 Effect of the geometrical configurations

The Sauter mean diameter is volume-averaged over the entire domain, $\overline{d}_{32}$, to evaluate the geometrical configurations in a single point and thereby compare the different configurations. It is observed that the volume-averaged Sauter mean diameter, $\overline{d}_{32}$, can be categorised based on the bend radius, which is seen in Fig. C.7.

It becomes clear that the bend radius is the single most important parameter when

aggregating particles in a hydraulic pipe flocculator, as seen when analysing the results in Fig. C.7. The overall trend of the configurations is that volume-averaged particle diameter increases as the bend radius increases, which is directly observed when comparing the results from the different bend radii in Fig. C.7a to C.7d and this is in good agreement with our previous study (Bilde et al., 2022). The difference in size between the configurations with bend radius $r_b = 2d_h$ and $r_b = 2.5d_h$, in Fig. C.7c and C.7d, are small compared to the other bend radii. This indicates that the effect of the bend radius stagnates around $r_b = 2d_h$. Secondly, it is observed that the primary length, L_1, is the second-most important parameter when aggregating the particles. When the primary length of the configuration increases, so does the mean particle diameter. For all simulations it is observed that the simulations with $L_1 = 20d_h$ yield the largest particle diameter, $\tilde{d}_{32}$. Thirdly, it is observed that the secondary length, L_2, has the smallest impact when aggregating particles. For the cases with a short primary length, $L_1 \leq 5d_h$, the secondary length becomes the primary length, and therefore the particle diameter, $\tilde{d}_{32}$, increases as a function of L_2. For the cases with the longest secondary lengths, $L_2 \geq 10d_h$, it is observed that a short secondary length creates larger aggregates depending on the bend radius. For the largest bend radii, it is observed that $L_2 = 0$ results in the largest overall particle diameter.

An interesting observation is made for the configurations with no straight pipe sections, $L_1 = L_2 = 0$, for all bend radii, as these configurations yield a high particle diameter compared to the configurations with the same bend radius. The helically coiled configuration with bend radii of $r_b = 2d_h$ and $r_b = 2.5d_h$, yields larger volume-averaged particle diameters when compared to the other configurations. As there are no straight pipe sections in these configurations, there is no transition from the bend to the straight pipe where the fluid flow will detach and create a downstream circulation zone (Hellström et al., 2013). These findings are in good agreement with the single-phase numerical findings of Oliveira and Teixeira (2018) and Oliveira et al. (2020).

Besides the findings of the configurations with $L_1 = L_2 = 0$, it is observed for all bend radii, that choosing a system with the longest primary length, $L_1 = 20d_h$ and no secondary length, $L_2 = 0$, results in the largest particle mean diameter.

C.4.7 Configuration response time

As all simulations have been started from the same monodisperse particle distribution of $d_p = 1$ μm, the time to reach a steady-state solution of the given geometrical configuration is of interest. The dimensionless length, $\tilde{L} = t_s u / d_h$, to reach a steady-state solution is used to evaluate the response time of the configurations. The configurations with the lowest induced turbulence produce the largest overall particle size, as seen in Fig. C.7, but as a function of this, these systems need the longest time to reach that steady-state solution, which is seen in Fig. C.8. The systems with the largest magnitude of induced turbulence, e.g. the systems with the smallest bend radius, produces smaller particles, but the time needed to obtain a steady-state solution is shorter compared to the systems with a larger bend radius.

The response length of the system is generally classified by the bend radius, as a smaller bend radius generally results in a shorter system response length. The

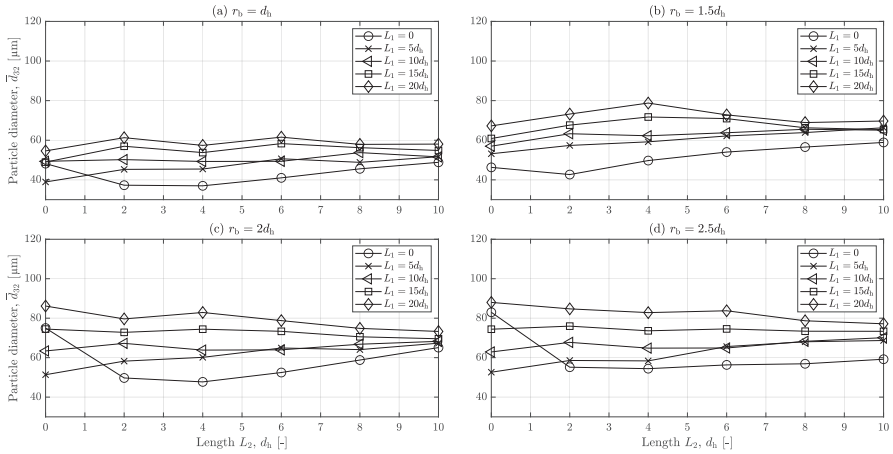

Fig. C.7: Global averaged Sauter mean diameter, $\overline{d}_{32}$, as a function of the secondary length for different primary lengths. C.7a: Bend radius of $r_b = d_h$. C.7b: Bend radius of $r_b = 1.5d_h$. C.7c: Bend radius of $r_b = 2d_h$. C.7d: Bend radius of $r_b = 2.5d_h$.

configurations with no primary- or secondary lengths, $L_1 = L_2 = 0$, have a longer response time compared to the other configurations with the same bend radius. This is explained by these configurations generally producing larger particles compared to the other configurations with the same bend radius and a longer response length is thereby needed. The difference in the dimensionless length needed to obtain a steady-state solution for the two largest bend radii, $r_b = 2d_h$ and $r_b = 2.5d_h$, there is only needed a slightly longer configuration to achieve a steady-state solution. As the particle size from the configurations is within similar range, this is also expected.

The response time for a configuration is highly dependent on the initial particle size, as the system will go towards a steady-state solution. In this study, where the simulation is initialised with monodisperse particles of $d_p = 1$ µm, the particles need to aggregate until a steady-state solution. The opposite initialisation could also be imagined, where the simulation is initialised with monodisperse particles of $d_p = 1000$ μm and the particles would then converge towards a steady-state solution by breakage instead of aggregation. This would result in a different response time for the configurations.

C.5 Conclusion

A numerical multiphase model is applied to simulate the aggregation and breakage of micron-sized particles subject to a turbulent fluid flow with a Reynolds number of $Re = 20,000$. The fluid-particle flow is modelled using the multi-fluid model where the particle number density function is modelled using the population balance equation that is solved using the class method implemented into the open-source CFD library OpenFOAM. The interfacial forces between the solid- and liquid phases are modelled using external force models. Monodisperse particles are inserted into a fully developed

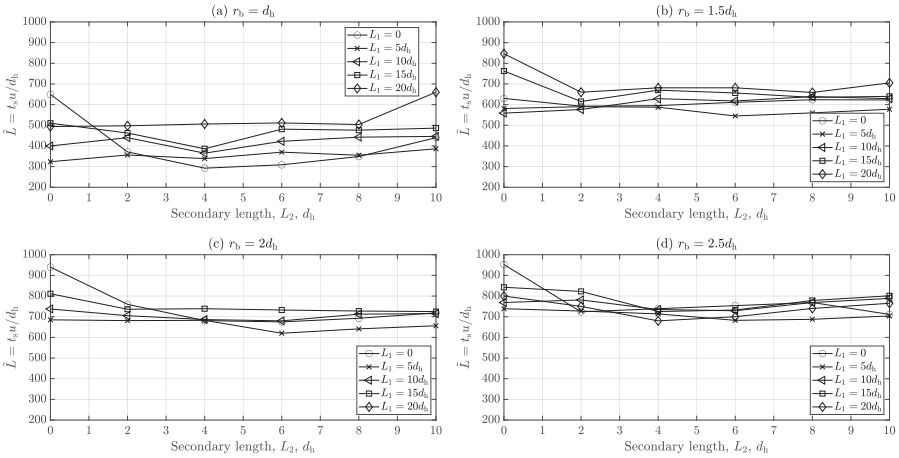

Fig. C.8: The dimensionless length needed to obtain a steady-state solution for the configurations. The dimensionless lengths for $r_b = d_h$ are shown in C.8a, the lengths for $r_b = 1.5d_h$ are shown in C.8b,the lengths for $r_b = 2d_h$ are shown in C.8c and the lengths for $r_b = 2.5d_h$ are shown in C.8d.

fluid velocity profile to initialise the simulation and track the time to reach a steady-state solution for the particle size distribution.

The geometrical parameters of a compact pipe flocculator are varied by changing the primary length, L_1, the secondary length, L_2, the bend radius r_b and the pitch of inclination, φ. The primary length is bounded by $0 \leq L_1 \leq 20d_h$, the secondary length is bounded by $0 \leq L_2 \leq 10d_h$ and the bend radius is bounded by $d_h \leq r_b \leq 2.5d_h$. A total of 123 simulations are completed to analyse the impact of the geometrical configurations under the turbulent flow conditions. It is found that the pitch of inclination has a negligible impact on the particle size distribution, which has the practical meaning that pipe flocculators can be made compact in the vertical direction without loss of performance.

Analysing the impact of the other geometrical parameters shows that the bend radius has the most significant impact on the particle size, as a smaller bend radius induces more turbulence due to the increased curvature in the bend. As the break-up of the aggregates is driven by turbulence, this causes the aggregates to break up at an increased rate compared to configurations with a larger bend radius.

Helically coiled configurations with no straight pipes, $L_1 = L_2 = 0$, and bend radius of $r_b \geq 2d_h$, resulted systems yielding large aggregates compared to other configurations with the same bend radius. This is explained by the lack of a re-circulation zone downstream from the pipe bend, which significantly increases the turbulence induced downstream of the pipe. These configurations comes at the cost of the longest dimensionless length needed to obtain a steady-state solution when initialising with monodisperse particles of $d_p = 1$ μm.

This study highlights the challenges of designing a compact hydraulic pipe flocculator as the available space often dictates the best configuration. The configurations simulated have a small- to medium footprint and therefore rely on the available height. It is shown that the configuration with a primary length of $L_1 = 20d_h$, a secondary

length of $L_2 = 0$ and a bend radius of $r_b = 2.5d_h$ results in the largest volume-averaged particle diameter for $Re = 20,000$ and particle properties resembling soot particles.

In practical terms, this means that the design of compact hydraulic flocculator becomes long and narrow with fewer connections to weld, which makes manufacturing and installation easier for industries where the available footprint is small but the available height is large.

References

Y. Adachi, M. A. Cohen Stuart, and R. Fokkink. Kinetics of Turbulent Coagulation Studied by Means of End-over-End Rotation. *Journal of Colloid and Interface Science*, 165(2):310–317, 7 1994. ISSN 0021-9797. doi: 10.1006/JCIS.1994.1234.

Kasper Gram Bilde, Jakob Hærvig, Ronald Lehnigk, Fabian Schlegel, and Kim Sørensen. On the agglomeration and breakage of particles in turbulent flows through pipe bends using CFD-PBE. *Chemical Engineering Science*, 260:117915, 10 2022. ISSN 00092509. doi: 10.1016/J.CES.2022.117915.

J. Bridgeman, B. Jefferson, and S.A. A. Parsons. The development and application of CFD models for water treatment flocculators. *Advances in Engineering Software*, 41(1): 99–109, 1 2010. ISSN 09659978. doi: 10.1016/J.ADVENGSOFT.2008.12.007.

John Bridgeman, Bruce Jefferson, and Simon Parsons. Assessing floc strength using CFD to improve organics removal. *Chemical Engineering Research and Design*, 86(8): 941–950, 8 2008. ISSN 0263-8762. doi: 10.1016/J.CHERD.2008.02.007.

Jonathan M Bridgeman. *Investigating the relationship between shear and floc fate using CFD*. PhD thesis, Cranfield University, 2006.

A. D. Burns, Thomas Frank, Ian Hamill, and J. M. Shi. The Favre averaged drag model for turbulent dispersion in Eulerian multi-phase flows. *5th International Conference on Multiphase Flow*, 4(392):1–17, 2004.

Thomas R. Camp and Philip C. Stein. Velocity Gradients and Internal Work in Fluid Motion. *Journal of Boston Society of Civil Engineering*, 30:219–237, 1943.

Andrew Escue and Jie Cui. Comparison of turbulence models in simulating swirling pipe flows. *Applied Mathematical Modelling*, 34(10):2840–2849, 10 2010. ISSN 0307-904X. doi: 10.1016/J.APM.2009.12.018.

Meng Fan, Liangfu Chen, Shenshen Li, Mingmin Zou, Lin Su, and Jinhua Tao. The Effects of Morphology and Water Coating on the Optical Properties of Soot Aggregates. *Aerosol and Air Quality Research*, 16:1315–1326, 2016. ISSN 2071-1409. doi: 10.4209/aaqr.2015.04.0250.

Mohamed Gar Alalm, Mahmoud Nasr, and Shinichi Ookawara. Assessment of a novel spiral hydraulic flocculation/sedimentation system by CFD simulation, fuzzy inference system, and response surface methodology. *Separation and Purification Technology*, 169:137–150, 9 2016. ISSN 1383-5866. doi: 10.1016/J.SEPPUR.2016.06.019.

Leo H.O. Hellström, Metodi B. Zlatinov, Guangjun Cao, and Alexander J. Smits. Turbulent pipe flow downstream of a 90° bend. *Journal of Fluid Mechanics*, 735:R7, 2013. ISSN 14697645. doi: 10.1017/jfm.2013.534.

Ricardo I Jeldres, Phillip D Fawell, and Brendan J Florio. Population balance modelling to describe the particle aggregation process: A review. *Powder Technology*, 326:190–207, 2017. doi: 10.1016/j.powtec.2017.12.033.

Zhaohua Jiang, Kenta Rai, Takuya Tsuji, Kimiaki Washino, Toshitsugu Tanaka, and Jun Oshitani. Upscaled DEM-CFD model for vibrated fluidized bed based on particle-scale similarities. *Advanced Powder Technology*, 31(12):4598–4618, 12 2020. ISSN 15685527. doi: 10.1016/j.apt.2020.10.009.

Sanjeev Kumar and D. Ramkrishna. On the solution of population balance equations by discretization—I. A fixed pivot technique. *Chemical Engineering Science*, 51(8): 1311–1332, 4 1996. ISSN 0009-2509. doi: 10.1016/0009-2509(96)88489-2.

K. A. Kusters. *The influence of turbulence on aggregation of small particles in agitated vessels*. PhD thesis, Technische Universiteit Eindhoven, 1991.

Marko Laakkonen, Pasi Moilanen, Ville Alopaeus, and Juhani Aittamaa. Modelling local bubble size distributions in agitated vessels. *Chemical Engineering Science*, 62(3): 721–740, 2 2007. ISSN 0009-2509. doi: 10.1016/J.CES.2006.10.006.

S Laine, L Phan, P Pellarin, and P Robert. Operating Diagnostics On A Flocculator-settling Tank Using Fluent CFD Software. *WIT Transactions on Ecology and the Environment*, 33, 1999. doi: https://doi.org/10.2495/WP990251.

Philipp Lau and Matthias Kind. CFD-PBE simulation to predict particle growth in a fluidized bed melt granulation batch process. *Powder Technology*, 300:28–36, 10 2016. ISSN 1873328X. doi: 10.1016/J.POWTEC.2016.02.040.

R. Lehnigk, W. Bainbridge, Y. Liao, D. Lucas, T. Niemi, J. Peltola, and F. Schlegel. An open-source population balance modeling framework for the simulation of polydisperse multiphase flows. *AIChE Journal*, page e17539, 12 2021. ISSN 1547-5905. doi: 10.1002/AIC.17539.

Dongyue Li, Zhengming Gao, Antonio Buffo, Wioletta Podgorska, and Daniele L. Marchisio. Droplet breakage and coalescence in liquid–liquid dispersions: Comparison of different kernels with EQMOM and QMOM. *AIChE Journal*, 63(6):2293–2311, 6 2017. ISSN 1547-5905. doi: 10.1002/AIC.15557.

Y. Liao, R. Oertel, S. Kriebitzsch, F. Schlegel, and D. Lucas. A discrete population balance equation for binary breakage. *International Journal for Numerical Methods in Fluids*, 87(4):202–215, 6 2018. ISSN 1097-0363. doi: 10.1002/FLD.4491.

Benoit B Mandelbrot. Self-Affine Fractals and Fractal Dimension. *Physica Scripta*, 32(4): 257, 10 1985. ISSN 1402-4896. doi: 10.1088/0031-8949/32/4/001.

Daniele L. Marchisio, R. Dennis Vigil, and Rodney O. Fox. Implementation of the quadrature method of moments in CFD codes for aggregation - breakage problems. *Chemical Engineering Science*, 58(15):3337–3351, 8 2003. ISSN 00092509. doi: 10.1016/S0009-2509(03)00211-2.

R. Mei. An approximate expression for the shear lift force on a spherical particle at finite reynolds number. *International Journal of Multiphase Flow*, 18(1):145–147, 1 1992. ISSN 0301-9322. doi: 10.1016/0301-9322(92)90012-6.

E. F. Mikhailov, S. S. Vlasenko, Igor A. Podgorny, V. Ramanathan, and C. E. Corrigan. Optical properties of soot–water drop agglomerates: An experimental study. *Journal of Geophysical Research: Atmospheres*, 111(D7):7209, 4 2006. ISSN 2156-2202. doi: 10.1029/2005JD006389.

D. S. Oliveira and E. C. Teixeira. Swirl number in helically coiled tube flocculators: theoretical, experimental, and CFD modeling analysis. *International Journal of Environmental Science and Technology*, 16(3):3735–3744, 2018. doi: 10.1007/s13762-018-2027-x.

D. S. Oliveira, E. C. Teixeira, and C. B. Donadel. Novel approaches for predicting efficiency in helically coiled tube flocculators using regression models and artificial neural networks. *Water and Environment Journal*, 34(4):550–562, 11 2020. ISSN 1747-6593. doi: 10.1111/WEJ.12484.

Danieli Soares de Oliveira and Clainer Bravin Donadel. Global velocity gradient evaluation: An innovative approach using CFD modeling applied to water and wastewater treatment plants. *Journal of Water Process Engineering*, 28:21–27, 4 2019. ISSN 2214-7144. doi: 10.1016/J.JWPE.2018.12.009.

A. Passalacqua, F. Laurent, E. Madadi-Kandjani, J. C. Heylmun, and R. O. Fox. An open-source quadrature-based population balance solver for OpenFOAM. *Chemical Engineering Science*, 176:306–318, 2 2018. ISSN 0009-2509. doi: 10.1016/J.CES.2017.10.043.

Liu-Chao Qiu, Jia-Jie Liu, Yi Liu, Peng-Zhi Lin, and Yu Han. CFD-DEM Simulation of Flocculation and Sedimentation of Cohesive Fine Particles. In *Proceedings of the 7th International Conference on Discrete Element Methods*, pages 537–542, 2016. ISBN 10.1007/9789811. doi: 10.1007/978-981-10-1926-5{_}55.

P. Saffman. The lift on a small sphere in a slow shear flow. *Journal of Fluid Mechanics1*, 22(2):385–400, 1965. doi: 10.1017/S0022112065000824.

F. Salehi, M. J. Cleary, and A. R. Masri. Population balance equation for turbulent polydispersed inertial droplets and particles. *Journal of Fluid Mechanics*, 831:719–742, 11 2017.

M. Sartori, D. S. Oliveira, E. C. Teixeira, W. B. Rauen, and N. C. Reis. CFD modelling of helically coiled tube flocculators for velocity gradient assessment. *Journal of the Brazilian Society of Mechanical Sciences and Engineering*, 37(1):187–198, 1 2015. ISSN 18063691. doi: 10.1007/s40430-014-0141-3.

M. v. Smoluchowski. Versuch einer mathematischen Theorie der Koagulationskinetik kolloider Lösungen. *Zeitschrift für Physikalische Chemie*, 92(1):129–168, 11 1917. ISSN 2196-7156. doi: 10.1515/ZPCH-1918-9209.

Josef Tausendschön, Jari Kolehmainen, Sankaran Sundaresan, and Stefan Radl. Coarse graining Euler-Lagrange simulations of cohesive particle fluidization. *Powder Technology*, 364:167–182, 3 2020. ISSN 1873328X. doi: 10.1016/j.powtec.2020.01.056.

Olle Törnblom. Turbulent Shear and Breakup of Flocculated Biomaterial in Centrifuge Inlets. *Chemical Engineering & Technology*, 41(12):2366–2374, 12 2018. ISSN 09307516. doi: 10.1002/ceat.201800297.

Yamuna S. Vadasarukkai, Graham A Gagnon, D. Reid Campbell, and Sarah C. Clark. Assessment of hydraulic flocculation processes using CFD. *American Water Works Association*, 103(11):66–80, 2011. doi: 10.1002/j.1551-8833.2011.tb11567.x.

Pei Wang, Shuai Shen, Ling Zhou, and Deyou Liu. Turbulent Aggregation and Deposition Mechanism of Respirable Dust Pollutants under Wet Dedusting using a Two-Fluid Model with the Population Balance Method. *International Journal of Environmental Research and Public Health*, 16, 2019. doi: 10.3390/ijerph16183359.

Xuetao Wang, Baoyu Cui, Dezhou Wei, Zhenguo Song, Yi He, and Andrew E. Bayly. CFD-PBM modelling of tailings flocculation in a lab-scale gravity thickener. *Powder Technology*, 396:139–151, 1 2022. ISSN 1873328X. doi: 10.1016/J.POWTEC.2021.10.054.

C.Y. Wen and Y.H. Yu. Mechanics of Fluidization. *The Chemical Engineering Progress Symposium Series*, 162:100–111, 1966.

Ping Xiang, Yihui Wan, Xun Wang, and Huilan Lian. Numerical simulation and experimental study of electrocoagulation grid flocculation tank. *Water Science and Technology*, 78(4):786–794, 2018. ISSN 02731223. doi: 10.2166/wst.2018.348.

V. Yakhot, S. A. Orszag, S. Thangam, T. B. Gatski, and C. G. Speziale. Development of turbulence models for shear flows by a double expansion technique. *Physics of Fluids A*, 4(7):1510–1520, 1992. ISSN 08998213. doi: 10.1063/1.858424.

Ya Yao, Yi Jun He, Zheng Hong Luo, and Lan Shi. 3D CFD-PBM modeling of the gas-solid flow field in a polydisperse polymerization FBR: The effect of drag model. *Advanced Powder Technology*, 25(5):1474–1482, 9 2014a. ISSN 15685527. doi: 10.1016/J.APT.2014.04.001.

Ya Yao, Jun-Wei Su, and Zheng-Hong Luo. CFD-PBM modeling polydisperse polymerization FBRs with simultaneous particle growth and aggregation: The effect of the method of moments. *Powder Technology*, 272:142–152, 2014b. doi: 10.1016/j.powtec.2014.11.037.

C. Yuan, F. Laurent, and R. O. Fox. An extended quadrature method of moments for population balance equations. *Journal of Aerosol Science*, 51:1–23, 9 2012. ISSN 0021-8502. doi: 10.1016/J.JAEROSCI.2012.04.003.

Minshu Zhan, Minghao You, Lingling Liu, Yilin Zhang, Fang Yuan, Baoyu Guo, Guojian Cheng, and Wei Xu. Numerical simulation of mechanical flocculation in water treatment. *Journal of Environmental Chemical Engineering*, 9(4):105536, 8 2021. ISSN 22133437. doi: 10.1016/j.jece.2021.105536.

Paper D

Aggregation and breakage of solid particles in a turbulent flow through a 90° pipe bend using CFD-PBE

Kasper Gram Bilde, Jakob Hærvig, Kim Sørensen

The paper was presented at the
17th OpenFOAM Workshop, University of Cambridge, United Kingdom, 11-14 July, 2022.

The layout has been revised.

Aggregation and breakage of solid particles in a turbulent flow through a 90° pipe bend using CFD-PBE

Kasper Gram Bilde*[,1], Jakob Hærvig[1], Kim Sørensen[1]

* *Corresponding author*
[1] *Aalborg University, Department of Energy, Pontoppidanstræde 111, 9220 Aalborg, Denmark*

Keywords: *Multiphase flow; Aggregation; Breakage; Population balance equation; MultiphaseEulerFoam*

The aggregation and breakage of particles in turbulent flows are of interest for many industries and applications. Several modelling procedures have been applied to dilute particle-laden flow to predict the aggregation and breakage of adhesive particles. The multiphase Euler-Euler method, where both the particle and fluid phases are modelled as continuous fields has proven beneficial for industrial-scale applications with micron-sized particles, as the number of particles otherwise becomes too large for typical Lagrangian methods. The population balance equation (PBE) is applied to account for the number density function of the particles in the computational domain. Several methods have been proposed to solve the PBE, where several are based on the method of moments (MOM). Some of the most common types of MOM are Quadrature MOM (QMOM), Direct QMOM (DQMOM) and Extended QMOM (EQMOM). An alternative approach to solve the PBE is the class method, which is implemented in the OpenFOAM multiphase Eulerian framework in the solver `multiphaseEulerFoam` Lehnigk et al. (2021). The polydisperse number density function is discretised into several size classes, thereby making the method straightforward and intuitive at the expense of a higher computational cost compared to the MOM methods.

The aggregation and breakage models for solid particles are described and implemented into the `multiphaseEulerFoam` framework in this study. Furthermore, interfacial momentum transfer is taken into account and the Saffman-Mei lift force is implemented into the `multiphaseEulerFoam` framework. The models are developed for OpenFOAM v9 and are accessible at the HZDR OpenFOAM Addon Schlegel et al. (2022). The modelling framework is then used to study the particle size distribution of micron-sized particles downstream of a 90° pipe bend for a turbulent fluid flow with a Reynolds number of $Re_\mathrm{f} = 20,000$.

Numerical framework: The continuity- and momentum equations for the multiphase Eulerian framework is seen in (D.1) and (D.2).

$$\frac{\partial}{\partial t}\left(\alpha_\varphi \rho_\varphi\right) + \nabla \cdot \left(\alpha_\varphi \rho_\varphi \vec{u}_\varphi\right) = 0 \tag{D.1}$$

$$\frac{\partial}{\partial t}\left(\alpha_\varphi \rho_\varphi \vec{u}_\varphi\right) + \nabla \cdot \left(\alpha_\varphi \rho_\varphi \vec{u}_\varphi \vec{u}_\varphi\right) - \nabla \cdot \tau_\varphi = -\alpha_\varphi \nabla p + \alpha_\varphi \rho_\varphi \vec{g} + \vec{M}_\varphi + \vec{S}_\varphi \tag{D.2}$$

where φ denotes each phase, α is the void fraction, ρ is the density, $\vec{u}$ is the velocity, τ is the stress tensor, p is the pressure, $\vec{g}$ is the gravitational acceleration, M is the rate

of interfacial momentum transfer and S is the momentum source term. Since the flow is turbulent and the geometrical setup introduces swirling in the flow, the RNG k-ε is applied to account for the Reynolds stresses. The class method for the PBE implemented in the `multiphaseEulerFoam` framework is seen in (D.3). The PBE is solved for each discretised size class.

$$\frac{\partial N_i}{\partial t} + \nabla \cdot \left(\vec{u} N_i\right) = S_i \tag{D.3}$$

where subscript i denotes each size group, N is the number of particles and S is the source term account for discontinuous changes in the number density function such as aggregation and breakage.

In this study, the drag-, lift-, virtual mass and turbulent dispersion force are implemented as interfacial momentum transfers. The drag coefficient is based on Wen and Yu (1966) where the drag coefficient is a function of the particle Reynolds number, Re_p and the particle volume fraction, α_p. The Saffman-Mei lift force model for finite Reynolds number is implemented in the multiphase Eulerian framework Mei (1992). A constant virtual mass coefficient of $C_\mathrm{VM} = 0.5$ is applied and a Favre averaged turbulent dispersion force model is applied Burns et al. (2004).

The turbulent aggregation kernel, β, by Adachi et al. (1994) can be seen in (D.4) and the breakage kernel, ζ, by Kusters (1991) can be seen in (D.5). The breakage kernel requires a daughter distribution function and a discretised beta distribution function is applied. The aggregation and breakage kernels for solid particles and the Saffman-Mei lift model are implemented in the multiphase Eulerian framework and are freely available at the HZDR Multiphase Addon for OpenFOAM Schlegel et al. (2022).

$$\beta = \frac{4}{3}\left(\frac{3\pi}{10}\right)^{0.5}\left(\frac{\varepsilon}{\nu}\right)\left(v_i + v_j\right)^3 \tag{D.4}$$

$$\zeta = \left(\frac{4}{15\pi}\right)^{0.5}\left(\frac{\varepsilon}{\nu}\right)^{0.5}\exp\left(-\frac{\varepsilon_\mathrm{cr}}{\varepsilon}\right) \tag{D.5}$$

where ε is the turbulent dissipation rate of the fluid, ν is the kinematic viscosity of the fluid, $v_{i,j}$ is the volume of particle i and j and ε_cr is the critical turbulent energy dissipation rate at which the agglomerates break.

Results: The particle size distribution is analysed for a 90° pipe bend with a bending radius of $r_\mathrm{b} = 1.5D$ with a dilute particle volume fraction of $\alpha_\mathrm{p} = 10^{-3}$. A length of $10D$ before and after the pipe bend is introduced, as seen in Fig. D.1a. The initial particle size distribution is seen in Fig. D.1b and a density ratio of $\rho_\mathrm{p}/\rho_\mathrm{f} = 1.4$ between the continuous and discrete phase. The Sauter mean diameter, $D_{3,2}$ is seen in Fig. D.1a and the particle size distribution for the inlet and at different positions downstream of the pipe bend is seen in Fig. D.1b. From Fig. D.1a it is seen that the particle size increases over the length of the geometry, but that the mean particle diameter increases significantly downstream of the pipe bend. As the particles move further downstream, the Sauter mean diameter increases further, which is both seen in Fig. D.1a and D.1b.

Conclusions: In this study, the population balance equation was successfully used in the multiphase Eulerian framework to describe the aggregation and breakage of micron-sized particles. The breakage and aggregation kernels were successfully implemented into the `multiphaseEulerFoam` framework as well as the interfacial lift force model.

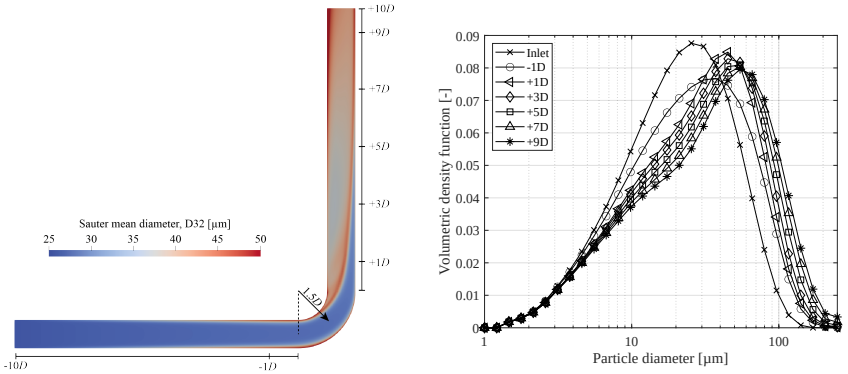

(a) Sauter mean diameter for the computational domain **(b)** Initial- and downstream particle size distributions.

The study shows how to model agglomeration and breakage of dilute particles in turbulent flows through a 90° pipe bend and how the particle size distribution increases downstream of the 90° pipe bend for the given particle properties.

References

Y. Adachi, M. A. Cohen Stuart, and R. Fokkink. Kinetics of Turbulent Coagulation Studied by Means of End-over-End Rotation. *Journal of Colloid and Interface Science*, 165(2):310–317, 7 1994. ISSN 0021-9797. doi: 10.1006/JCIS.1994.1234.

A. D. Burns, Thomas Frank, Ian Hamill, and J. M. Shi. The Favre averaged drag model for turbulent dispersion in Eulerian multi-phase flows. *5th International Conference on Multiphase Flow*, 4(392):1–17, 2004.

K. A. Kusters. *The influence of turbulence on aggregation of small particles in agitated vessels*. PhD thesis, Technische Universiteit Eindhoven, 1991.

R. Lehnigk, W. Bainbridge, Y. Liao, D. Lucas, T. Niemi, J. Peltola, and F. Schlegel. An open-source population balance modeling framework for the simulation of polydisperse multiphase flows. *AIChE Journal*, page e17539, 12 2021. ISSN 1547-5905. doi: 10.1002/AIC.17539.

R. Mei. An approximate expression for the shear lift force on a spherical particle at finite reynolds number. *International Journal of Multiphase Flow*, 18(1):145–147, 1 1992. ISSN 0301-9322. doi: 10.1016/0301-9322(92)90012-6.

Fabian Schlegel, Kasper Gram Bilde, Mazen Draw, Ilya Evdokimov, Susann Hänsch, Harris Khan, Ronald Lehnigk, Jiadong Li, Hongmei Lyu, Richard Meller, Gašper Petelin, and Matej Tekavčič. HZDR Multiphase Addon for OpenFOAM, 9 2022.

C.Y. Wen and Y.H. Yu. Mechanics of Fluidization. *The Chemical Engineering Progress Symposium Series*, 162:100–111, 1966.

ISSN (online): 2446-1636
ISBN (online): 978-87-7573-741-3

AALBORG UNIVERSITY PRESS